國立臺灣大學理學院化學研究所

博士口試論文

Department of Chemistry

College of Science

National Taiwan University

PhD Thesis

含金屬並具有微晶型孔壁 SBA-1 的合成、鑑定及催化

活性之探討

Synthesis, Characterization and Catalytic Properties of

Metal-incorporated SBA-1 with Zeolitic Wall

林宗翰

Tsung-Han Lin

指導教授：鄭淑芬 博士

Advisor: Soofin Cheng, Ph.D.

中華民國 103 年 7 月

July, 2014

摘要

本研究在鹼性的環境下 (pH~9) 合成結晶型孔壁之含鋁 SBA-1 介孔材料，模板使用 cetyltriethylammonium bromide (CTEABr)，而矽源是用含鋁的 ZSM-5 seeds，合成出來的介孔材料稱為 Al-ZSBA-1，其鋁含量可以高達 5.7%並擁有規則性排列之 3D cubic $Pm3n$ 的結構、高表面積 (600 m^2/g) 和孔洞體積，經由 NH_3-TPD 和離子交換法可測量出 Al-ZSBA-1 的酸性性質，從 ^{27}Al MAS NMR 知道大部分的 Al 都是四配位，我們也合成出非晶型孔壁之含鋁 SBA-1 (Al-SBA-1-alk)，並比較這兩種觸媒的催化活性，使用的催化反應為 2,4-di-*tert*-butylphenol (DTBP) 和 cinnamyl alcohol 經由 Friedel-Crafts reaction 產生中間產物 2,4-di-*tert*-butyl-6-cinnamylphenol (DTBCP)，再經由 Michael addition 可得到最終產物為 flavan，由催化結果得知擁有結晶型孔壁之介孔材料的酸性強度會比較高，flavan 選擇率會跟 ZSM-5 相似，其中以 7Al-ZSBA-1 的催化效果最好，flavan 的選擇率和產率分別為 75%和 39%。

另外，我們也在鹼性的環境下成功地合成具有三維孔洞結構的含鈦介孔材料 (Ti-SBA-1-alk)，接著使用沉積沉澱法將金離子放在含鈦介孔材料，命名為 yAu^{3+}/xTi，所得材料經由 XRD、N_2 adsorption-desorption isotherms、UV-Vis spectra、ICP-MS 和 TEM 等技術鑑定，可得知所合成出來的材料擁有很好的三維介孔結構、表面積可達到 800 m^2/g 以上以及很高的孔洞體積，而且當 Ti/Si 莫耳比小於 3%時，大多數的鈦離子是在骨架中的四面體中心，並且由 TEM 和 ICP-MS 得知金奈米粒子的大小與金含量是成正相關的，而金含量會隨著鈦含量提高而提高。

藉著改變金和鈦的含量，探討金和鈦之間的協同效應對催化丙烯環氧化反應的活性，發現當金含量小於 1wt%時，會得到很高的 PO 選擇率，其中以 10Au^{3+}/3Ti

觸媒的催化效果最好，丙烯的轉化率和環氧丙烷的選擇率分別可達到 7.4%和 91.7%，

其氫氣的選擇率高達 38.3%。我們也使用 TS-1 seed 當作矽源成功地合成出具有結

晶型孔壁含鈦的介孔材料，命名為 Ti-ZSBA-1，其物理與化學性質都跟 Ti-SBA-1-alk

很相似，然而，其催化活性會比 Ti-SBA-1-alk 高，最重要的是觸媒的失活現象有

所改善，其中以 10Au^{3+}/3TiZ 觸媒的催化表現最好，丙烯的轉化率和環氧丙烷的選

擇率分別可達到 8.64%和 92.6%，其氫氣的選擇率高達 43.5%。

Abstract

Cubic *Pm*3*n* mesoporous aluminosilicate isomorphous to SBA-1 with three-dimensional inter-connected pore structures was prepared in alkaline condition (pH around 9) using aluminum-incorporated ZSM-5 seeds as the Si and Al sources and cetyltriethylammonium bromide (CTEABr) as pore-directing agent with the aid of NaCl salt. The resultant materials (termed Al-ZSBA-1) with Al loading up to Al/Si molar ratio of 0.057 have cubic *Pm*3*n* structure and high surface areas (ca. 600 m^2/g). They showed stronger acidities than the counter materials prepared using sodium silicate as the silica source (referred as Al-SBA-1-alk). Moreover, all the Al in Al-ZSBA-1 retained in tetrahedral coordination after calcination at 823 K, while a portion of Al incorporated in Al-SBA-1-alk became octahedrally coordinated. When applying the materials as catalysts in the alkylation of 2,4-di-*tert*-butylphenol (DTBP) with cinnamylalcohol to form flavan, Al-ZSBA-1 gave higher flavan selectivity of 75% and yield of 39% than Al-SBA-1-alk, mordenite, ZSM-5, and beta zeolites. These results demonstrated that the Al-ZSBA-1 materials owned the advantages of strong acidity from zeolite nanostructures and good diffusivity from mesopores.

In addition, cubic *Pm*3*n* mesoporous Ti-incorporated silica with 1-5mol% Ti content have been prepared by co-condensation method and gold clusters were deposited on these supports by deposition-precipitation (DP) method. These resultant materials (termed yAu^{3+}/xTi, x and y represent the Ti/Si molar percentage and Au/support weight percentage in the synthesis solution, respectively.) were characterized by XRD patterns, N$_2$ adsorption-desorption isotherms, UV-Vis spectra and TEM. All samples have cubic *Pm*3*n* structure and high surface areas. The studies by

UV-Vis spectra indicated that the Ti(IV) in the catalysts with low Ti content was favorably in tetrahedral (T_d) coordination, whereas for the catalysts with Ti/Si molar ratio above 5%, a larger amount of Ti(IV) was in octahedral coordination. TEM images showed that the average particle size is larger than 3 nm as actual gold loadings is above 1wt%.

The catalytic results showed the catalyst with low actual gold loadings (< 1wt%) which is more selective to PO, while at high gold loadings (> 1wt%), the catalyst showed lower PO selectivity. In propylene epoxidation with H_2 and O_2, 7.4% propene conversion and > 90% PO selectivity were achieved over $10Au^{3+}/3Ti$ catalyst. We also successfully synthesized Ti-ZSBA-1 materials with zeolitic wall by using TS-1seeds as silica source and CTEABr as surfactant. The $10Au^{3+}/3TiZ$ catalyst gave higher propylene conversion of 8.6% and PO selectivity of 92.6% than $10Au^{3+}/3Ti$. Most of all, the deactivation problem was improved significantly and the decay rate of $10Au^{3+}/3TiZ$ is smaller than $10Au^{3+}/3Ti$.

Keywords: cubic *Pm*3*n,* mesoporous, Ti-SBA-1; propylene epoxidation, gold, zeolite seed; Al-incorporation

Content

Figure captions

Table index

XV

Scheme index

Chapter 1   Introduction

1.1 Micelle, packing parameter and mesoporous silica

The surfactant molecule consists of two parts, namely, a polar hydrophilic head group and an apolar hydrophobic tail (hydrocarbon chain). A schematic representation of a surfactant molecule and a micelle is shown in Fig. 1-1.[1] The surfactants with hydrophobic tails and hydrophilic charged headgroups are self-assembled to definite micelle structures. The main controlling forces of these micelle structures involve hydrophobic affinity on the hydrocarbon-water interface and hydrophilic repulsion, ionic repulsion, and steric repulsion of charged headgroups. The surfactant must pack to fill space and, thus, maximize favorable van der Waals interactions between the hydrophobic tails while avoiding high-energy repulsive interactions between the charged or polar headgroups. The packing of the surfactant molecules has been quantified through the use of the packing parameter, $g = V/a_o l$, where V is the total volume of the hydrophobic chains, a_o is the effective headgroup area per hydrophilic headgroup and l is the critical hydrophobic chain length. The a_o parameter is related to both the size and the charge on the surfactant headgroup and is affected by the electrostatic environment around the surfactant headgroup. The packing parameters of ionic surfactants are widely used in predicting and explaining the final mesophase of mesoporous structure.[2] Israelachvili *et al.*[3,4] have reported that depending on the value of packing parameter, the surfactant aggregates could acquire different shapes. They showed that in general micelles are spherical for $g < 1/3$ and ellipsoidal and cylindrical for $1/3 < g < 1/2$. The surfactant aggregates tend to be bilayers for $g > 1/2$ and in suitable cases this results in formation of vesicles (Fig. 1-2).[5] Additional factors such as

the degrees of ionization of surfactants, temperature, concentration, ionic strength, pH

and additives like alcohol, salts, etc. also influence the self-assembled structure.
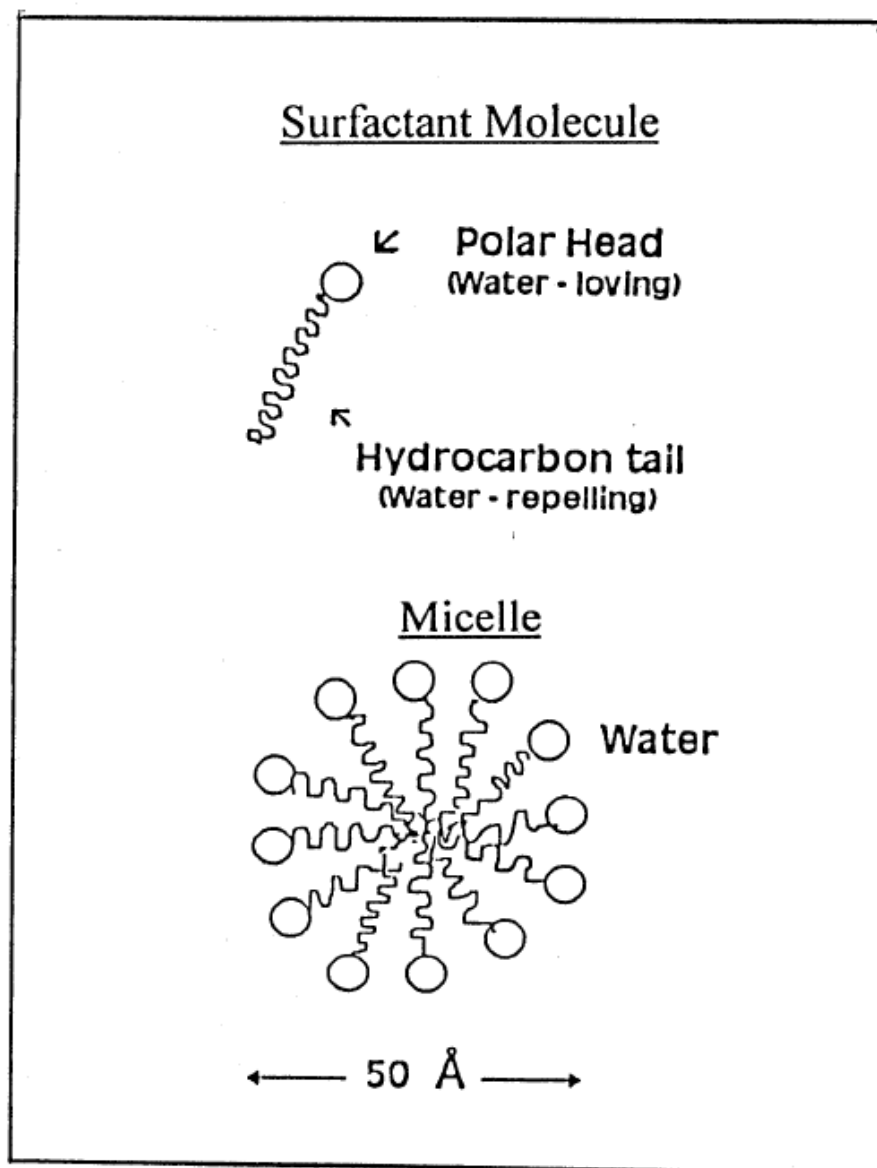
Fig. 1-1 A schematic structure of a micelle and a surfactant molecule.1
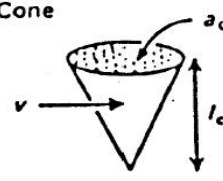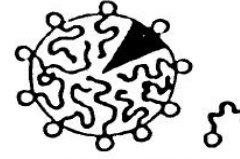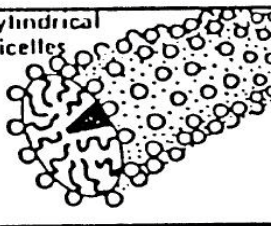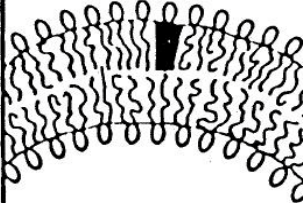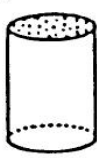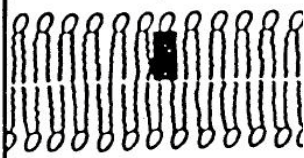
g	Critical packing shape	Structures formed
< 1/3	Cone	Spherical micelles
1/3-1/2	Truncated cone	Cylindrical micelles
1/2-1	Truncated cone	Flexible bilayers, vesicles
~1	Cylinder	Planar bilayers

Fig. 1-2 The packing parameter of a surfactant molecule and the various structures formed in aqueous solutions.[5]

In 1992, scientists at Mobil Oil research and Development reported the synthesis of mesostructued silicates.[6,7] In Mobil's report, quaternary ammonium cationic surfactants such as cetyltrimethylammonium bromide ($C_{16}H_{33}N(CH_3)_3Br$, CTABr) were first used as templates to prepare highly ordered M41S mesoporous silicate molecular sieves under hydrothermal, basic conditions. This kind of attractive material has high surface area,

high thermal stability, uniform pore sizes, tunable porosities and open frameworks. These characteristics are very important in field of catalysis, separation, sensors, adsorption, optical devices, etc.[8,9,10,11] According to IUPAC definition, inorganic solids that contain pores with diameters in the size range of 20–500 Å are considered as mesoporous materials. Examples of mesoporous materials include zeolites, M41S, aerogels, and pillared layered structures, as listed in Table 1-1.[12]

Table 1-1 Pore-size regimes and representative porous inorganic materials.[12]

Pore-size regimes	Definition	Examples	Actual size range
macroporous	> 500 Å	glasses	> 500 Å
mesoporous	20 – 500 Å	aerogels	> 100 Å
		pillared layered clays	10 Å, 100 Å[a]
		M41S	16 – 100 Å
microporous	< 20 Å	zeolites, zeotypes	< 14.2 Å
		activated carbon	6 Å

[a] Bimodal pore-size distribution.

Many studies have been reported on the synthesis and formation mechanisms for mesoporous silica. In 1992, a liquid crystal templating (LCT) mechanism was proposed by the Mobil researchers based on the similarity between liquid crystalline surfactant assemblies and M41S.[7] A key feature of the LCT mechanism is that the liquid crystalline mesophases or micelles act as templates rather than individual single molecules or ions. Accordingly, the final product is a silicate skeleton which contains voids that mimics these mesophases. The silicate condensation is not the dominant factor in the formation of the mesoporous structure. The whole process may be via two possible mechanistic pathways as schematically shown in Fig. 1-3: (1) the liquid crystal mesophases may form prior to the addition of silicate species; (2) the silicate species

added to the reaction mixture may influence the ordering of the isotropic rod-like micelles to the desired liquid crystal phase, i.e., hexagonal mesophase. Therefore, the mesophase formed is structurally and morphologically directed by the existing liquid crystal micelles. It is now known that pathway 1 did not take place because the surfactant concentrations used were far below the critical micelle concentration (CMC) required for hexagonal LC formation.[13] The second mechanistic pathway of LCT was postulated as a cooperative self-assembly of the ammonium surfactant and the silicate precursor species below the CMC.
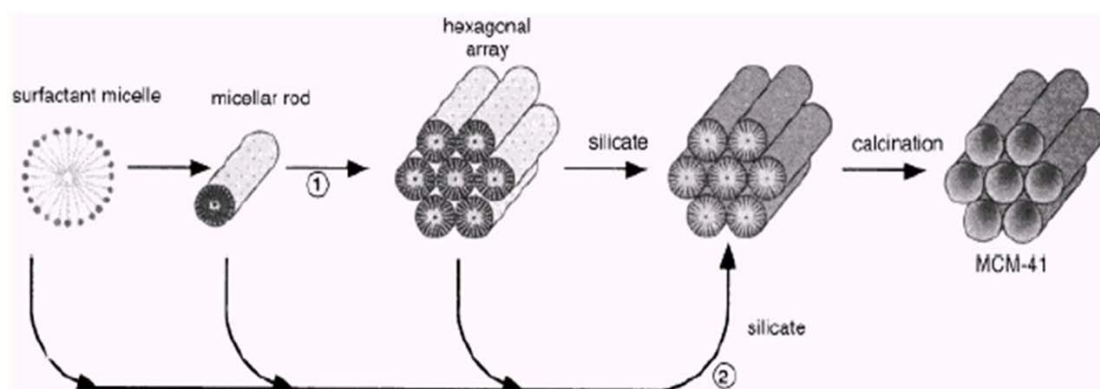
Fig. 1-3 Liquid crystal templating mechanism.7

Davis and co-workers proposed a "silicate rod assembly" mechanism shown in Fig. 1-4.[14] They have investigated the formation mechanism by employing XRD, ^{29}Si solid state NMR, in situ ^{14}N NMR and thermo gravimetric analysis (TGA) techniques. Two or three monolayers of silicate species first deposit on isolated surfactant micellar rods. The long surfactant-silicate rods spontaneously aggregate and eventually pack into a long-range ordered hexagonal arrangement. Heating and aging then completed the condensation of the silicates into the as-synthesized MCM-41 mesostructure. This mechanism is however unconvincing due to the difficulty of assembling long rods.
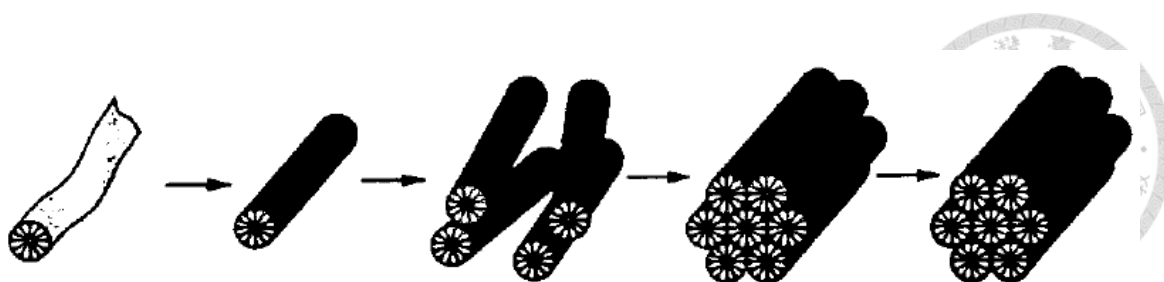
Fig. 1-4 Assembly of silicate-encapsulated rods.[14]

In 1993, a "charge density matching" mechanistic model was proposed by Monnier et al.[15] and suggested that MCM-41 could be derived from a lamellar phase. The authors proposed that in a surfactant/silicate aqueous mixture with relatively low pH, a low degree of polymerization of silica species, and low temperatures, small silica oligomers play an important role in the formation of mesoporous phase. In part, this is because they can interact with surfactant cations by Coulombic interactions at the interfaces, leading to a strong interaction by multidentate binding between them. As polymerization of the silicate species proceeds, the average head group area (a_o) of surfactant assembly increases due to the decrease of the charge density of larger silicate polyanions. This leads to the corrugation of the silicate layers and ultimately results in the hexagonal mesophase precipitation. Fig. 1-5 schematically shows the transformation mechanism from lamellar to hexagonal phase through charge matching.
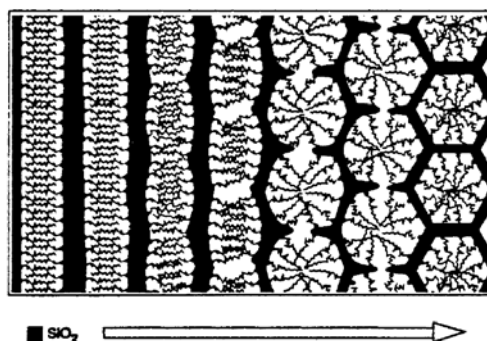
Fig. 1-5 Curvature induced by charge density matching. The arrow indicates the reaction coordinate.[15]

6

In 1994, Steel et al.[16] postulated that surfactant molecules assembled directly into the hexagonal LC phase upon addition of the silicate species, based on ^{14}N NMR spectroscopy. The silicates were organized into layers, with rows of the cylindrical rods intercalated between the layers (Fig. 1-6). Aging the mixture caused the layers to pucker and collapse around the rods, which then transformed into the surfactant-containing MCM-41 hexagonal-phase mesostructure.
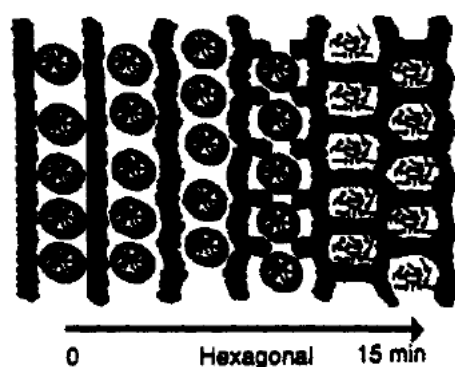
Fig. 1-6 Puckering of silicate layers in the direction.[16]

Firouzi et al.[17] suggested that ion exchange between surfactant anions (OH⁻, Br⁻, Cl⁻) and multiply charged anionic silica oligomer (D4R, double four ring, $[Si_8O_{20}]^{8-}$) may take place in a surfactant-silicate aqueous solution because the high anionic charge densities of the oligomer (Fig. 1-7). Silicate oligomers interact with positively charged groups in cationic surfactants driven by Coulomb forces. The silicate species at the interface polymerize and cross-link and further change the charge density of the inorganic layers. With the proceeding of the reaction, the arrangements of surfactants and the charge density between inorganic and organic species influence each other. Hence the compositions of inorganic-organic hybrids differ to some degree. It is the matching of charge density at the surfactant/inorganic species interfaces that governs

7

the assembly process. The transformation of the isotropic micellar solutions of CTAB into hexagonal or lamellar phases when mixed with anionic silicate oligomers in highly alkaline solutions was indeed detected through a combination of correlated solution state ^{2}H, ^{13}C and ^{29}Si NMR spectroscopy, small-angle X-ray scattering (SAXS) and polarized optical microscopy measurements.

precursor solutions

micelles and isolated cationic surfactant molecules

inorganic silicate anions (for example, D4R oligomers)

ion exchange

or

SLC assembly

phase transformation

lamellar SLC

hexagonal SLC
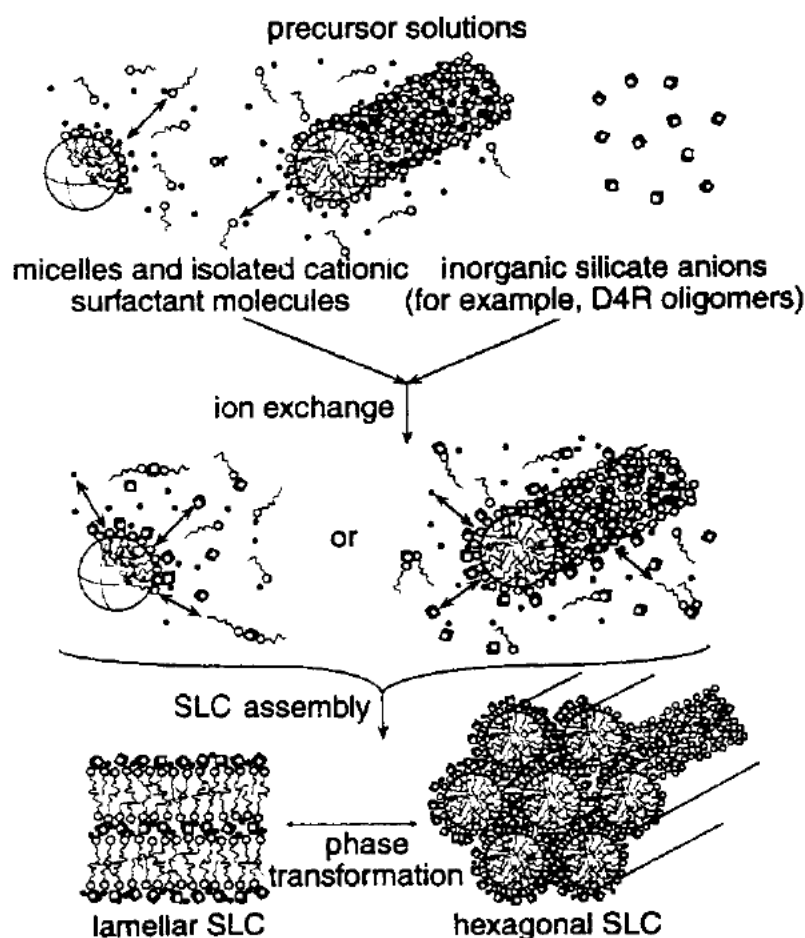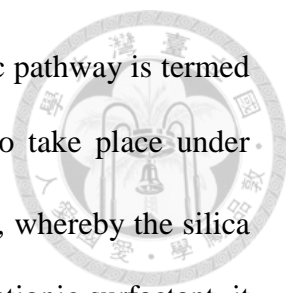
Fig. 1-7 Formation of a silicatropic liquid crystal phase.[17]

A generalized mechanism of formation based on the specific type of electrostatic interaction between a given inorganic precursor I and surfactant head group S was proposed by Huo and co-workers.[18,19] These interactions are classified as follows shown in Fig. 1-8.[20] If the reaction takes place under basic conditions and cationic

8

quaternary ammonium surfactants are used as the SDA, the synthetic pathway is termed S^+I^- (S: surfactant; I: inorganic species). The preparation can also take place under acidic conditions (below the isoelectric point of the Si-OH; pH = 2), whereby the silica species are positively charged. To produce an interaction with the cationic surfactant, it is necessary to add a mediator ion X^- (usually a halide) ($S^+X^-I^+$). Conversely, when negatively charged surfactants (e.g., long-chain alkyl phosphates) are used as the SDA, it is possible to work in basic media, whereby again a mediator ion M^+ must be added to ensure interaction between the equally negatively charged silica species ($S^-M^+I^-$); a mediator ion is not required in acidic media (S^-I^+). Thus, the dominating interactions in pathways are electrostatic. Moreover, it is still possible for the attractive interactions to be mediated through hydrogen bonds. This is the case when nonionic surfactants are used (e.g., S^o: a long-chained amine; N^o: polyethylene oxide), whereby uncharged silica species (S^oI^o) or ion pairs ($S^o(XI)^o$) can be present.
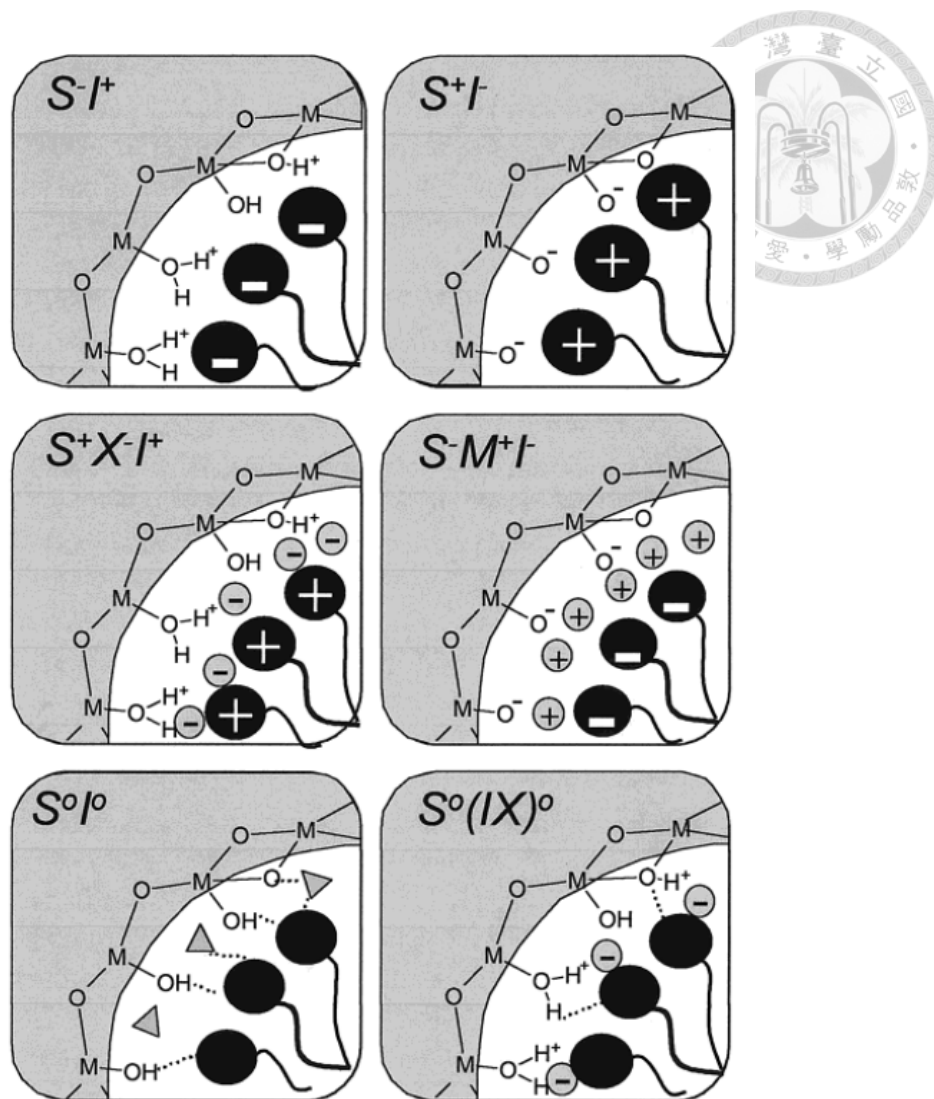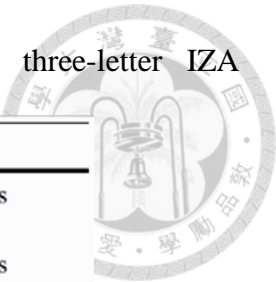
Fig. 1-8 Schematic representation of the different types of silica-surfactant interfaces. S represents the surfactant molecule and I, the inorganic framework. M^+ and X^- represent the corresponding counter ions. Solvent molecules are not shown, except for the I^oS^o case (triangles); dashed lines correspond to H-bonding interactions.[20]

1.2 Zeolites

The term zeolite was originally coined in 1756 by Swedish mineralogist Axel Fredrik Cronstedt, who observed that that on heating a natural zeolite mineral, the solid material appeared to bubble and the particles to dance, as water was lost as steam from the pores of the mineral. Based on this, Cronstedt combined the Greek words "zeo" (to boil) and "lithos" (stone) to form the word zeolite. The aluminosilicate zeolites of general formula $A_{x/n}$-$[Si_{1-x}Al_xO_2]$ · mH_2O, where A is typically a metal cation of valence n, were the first class of nanoporous materials to be recognized. They occur quite extensively in nature, and synthetic examples were made as early as the mid 19th century.

The nomenclature is often confusing, in spite of the fact that the International Zeolite Association has assigned a three-letter code to each structure type. A typical example would be FAU, which represents the family of materials with the faujasite-type structure. Nevertheless, many materials are more commonly known by acronyms chosen by the laboratories in which they were discovered. Pore sizes range from about 2.5 Å in the case of sodalites (SOD), in which the largest channel has rings containing 6 Si/Al sites (i.e. 6-rings), to about 10 Å in so-called UTD-1 which has a 14-ring channel. Some common examples are given in Table 1-2.[21] Zeolitic materials are well known to exhibit large pore volumes that are associated with very low tetrahedral (T) site densities (<20 T atoms/1000 $Å^3$, T = Si, Al). The majority of the systems with large channels contain rings with even numbers of T sites, for example 8-, 10-, 12- or 14-rings.

Table 1-2 Examples of nanoporous aluminosilicates, with the three-letter IZA designations and a brief description of the pore systems.

System	Pore system
sodalite family (SOD) (e.g. mineral and synthetic sodalites)	3-dimensional; 6-ring channels
zeolite A family (LTA) (e.g. zeolites A, ZK-4; no mineral analogue)	3-dimensional; 8-ring channels
chabazites (CHA) (e.g. mineral chabazites, SSZ-13)	3-dimensional; 8-ring channels
ZSM-5 (MFI) (e. g. mineral murataite, silicalite)	2-dimensional; 10-ring channels
ferrierites (FER) (e.g. mineral and synthetic ferrierites)	2-dimensional; 10 and 8-ring channels
faujasites (FAU) (e.g. mineral faujasite, zeolites LSX, X, Y, US-Y)	3-dimensional; 12-ring channels

Zeolites are crystalline, hydrated aluminosilicates having microporous, regular structures. The presence of charge compensation cations (alkaline, alkaline-earth, protons, etc.) within the porosity of the inorganic frameworks gives to these materials ionic exchange and catalytic properties, which are widely used in the industry. Moreover, the hydrophobic (zeosils, SiO_2) or hydrophilic (aluminosilicates) nature of the tailorable inorganic framework make these solids useful as specific adsorbents of organic molecules or water in the gas or liquid phase. The main applications of zeolitic materials are adsorption and drying, catalysis, and detergency. Table 1-3 summarizes some of the most important actual and prospective applications. Hydrated low-silica zeolites (Si/Al<2), such as synthetic sodium zeolite A (LTA), are used widely for ion-exchange applications where their high cation content leads to high exchange capacities. Dehydrated forms of the large-pore low-silica zeolites, such as zeolite X (FAU), are used in adsorption and separation applications, including non-cryogenic air separation. The low-silica materials are relatively unstable at high temperatures, so
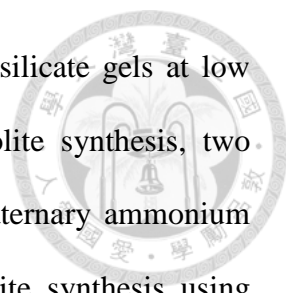
materials with high Si/Al ratios are preferred for catalytic applications. These include

high-silica ultrastabilized Y and ZSM-5.

Table 1-3 Some important applications of aluminosilicate zeolites[21].

Well-established:

ion-exchange with hydrated zeolites
    detergency (e.g. zeolites Na-A and Na-P)
    water softeners
    animal feeds
    radwaste remediation (e.g. Cs, Sr with clinoptilolite)
molecular sieving with dehydrated zeolites
    air separation (N_2 from O_2 with Li-LSX)
    drying agents (e.g. double glazing, air conditioning)
    sulfur removal from natural gas
    separation of HFCs (CFC substitutes)
catalysis with dehydrated zeolites
    catalytic cracking (gasoline production)—zeolite-Y derivatives
    xylene isomerization (for polyesters)—H-ZSM-5
    butene isomerization—H-FER
    methanol to gasoline—H-ZSM-5
    phenol to hydroquinone—titanosilicates
    denox reactions—Cu-ZSM-5, Co-FER

Future possibilities include:

nano-composites for electro-optics
    sensors with zeolite thin films
    stereoselective polymerization
    contrast enhancement in MRI (e.g. Gd-Y)

The first natural zeolite was discovered in 1756 and efforts to synthesize zeolites

can be traced back to 1862.[22] Early attempts of zeolite synthesis centered around

mimicking geologic conditions that involve high temperatures (T>473 K) and pressures

(P > 100 bar). Since the 1940s, systematic synthetic studies have been disclosed. In

1948, the first synthesis of a zeolite that did not have a natural counterpart was

accomplished by Barrer.[23] However, zeolite technology was initiated in the late 1940s

by the large-scale, synthetic methodologies of Milton and co-workers, who developed

hydrothermal zeolite syntheses using reactive alkali-metal aluminosilicate gels at low temperatures (~373 K) and pressures.[24] In next advance for zeolite synthesis, two groups of workers disclosed in 1961 the effect of introducing quaternary ammonium cations into zeolite synthesis. Barrer and Denny reported a zeolite synthesis using alkylammonium cations, namely, an intermediate, silica analogue of zeolite A using tetramethylammonium (TMA$^+$) cation.[25] They predicted that the addition of alkylammonium ions to sodium aluminosilicate gels increased the framework Si/A1 ratio. Kerr and Kokotailo published data on a silica-rich version of zeolite A named ZK-4 (Si/Al up to 1.7) although no mention of its method of preparation was made in the open literature until a later publication.[26,27] In fact, the word "template" has been applied to the "organizing ability" of TMA$^+$ toward sodalite cage formation. The use of organic materials in zeolite syntheses was quickly expanded after the initial work of Barrer and Denny. Many new high-silica zeolites were crystallized using organic molecules with aluminosilicate gels at 373-473 K. For example, zeolites β (BEA), ZSM-5, and ZSM-11 (MEL) are synthesized using tetraethylammonium, tetrapropylammonium, and tetrabutylammonium ions, respectively.

ZSM-5 (Zeolite Socony Mobil–5, structure type MFI – mordenite framework inverted) is an aluminosilicate zeolite mineral belonging to the pentasil family of zeolites. ZSM-5 catalyst was first synthesized by Argauer and Landolt in 1972.[28] ZSM-5 typically crystallizes in the *Pnma* orthorhombic space group with lattice constants a = 20.1, b = 19.9, and c = 13.4 Å. Fig. 1-9 and Fig. 1-10 show the skeletal diagram of (100) and (010) face of ZSM-5 respectively, where the 10-membered ring apertures are the entrances to the sinusoidal channels. Fig. 1-11 shows the channel structure of ZSM-5.[29] There are two channel systems in ZSM-5: a straight channel

running parallel to (010) with 10-ring openings of 5.4 × 5.6 Å, and a sinusoidal channel parallel to the (100) axis with 10-ring openings of dimension 5.1 × 5.5 Å (Fig. 1-12).[30] ZSM-5 can be obtained in the presence of a great variety of organic species.

However, the pure phase can be obtained only by performing the synthesis in the presence of tetrapropylammonium cations (TPA$^+$) cations. The examples were all based on a mixture of TPA$^+$ and sodium cations using a synthesis temperature of 125-175 °C for a reaction time of 5-9 days. In the as-synthesized solids, four TPA$^+$ per unit cell are occluded within the inorganic framework, at the intersection of both systems of channels. Solid-state NMR studies of the reaction gels along the synthesis performed by Burkett and co-workers confirmed the van der Waals interactions between the TPA$^+$ and the inorganic silica species.

ZSM-5 with pore diameter in the range of 0.51 - 0.56 nm has shape selectivity in cracking of n-paraffins and n olefins. This effect is attributed that in ZSM-5 channel the diffusion coefficients for branched and linear hydrocarbons are much different. For example, ZSM-5 as a Fluid Catalytic Cracking (FCC) catalyst can boost gasoline octane number yield of propylene in the gas products.[31]
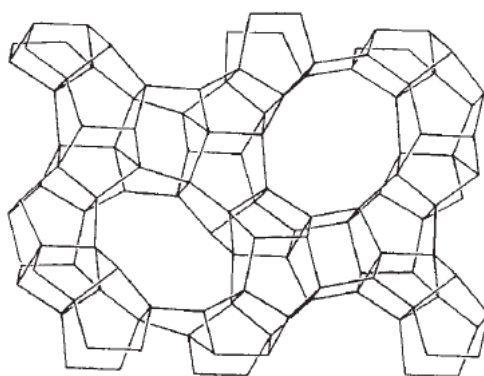
Fig. 1-9 skeletal diagram of (010) face of ZSM-5.[29]
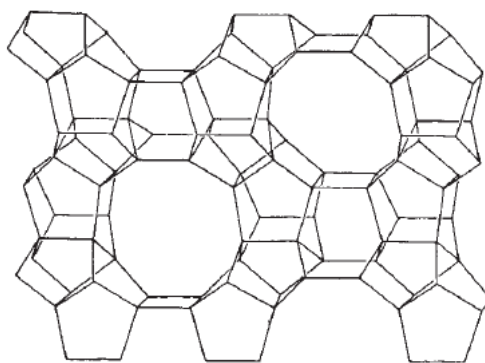
Fig. 1-10 skeletal diagram of (100) face of ZSM-5.[29]
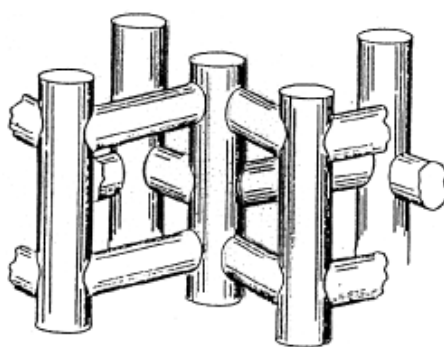
Fig. 1-11 Two type of channel of ZSM-5.[29]

10-ring viewed along [010]
(straight channel)

10-ring viewed along [100]
(sinusoidal channel)
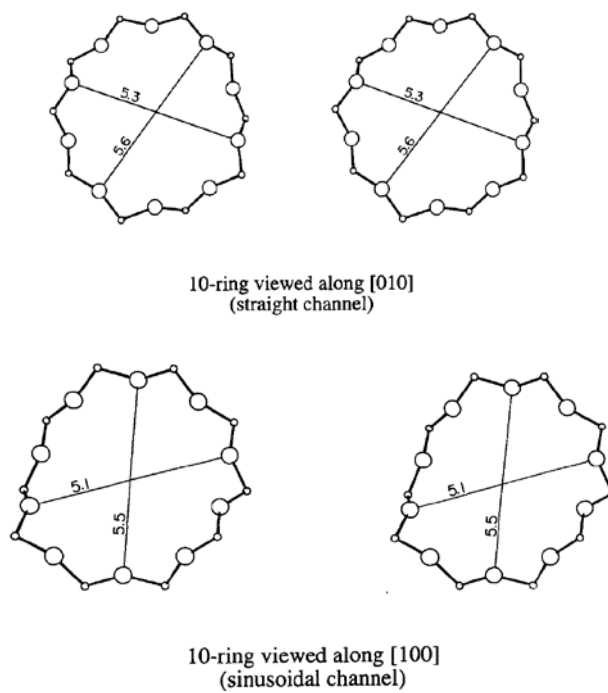
Fig. 1-12 Pore size of ZSM-5.[30]

1.3 SBA-1

In 1994, a cubic *Pm*3*n* phase SBA-1 was first synthesizes by using cetyltriethylammonium bromide (CTEABr) as a surfactant and tetraethyl orthosilicate (TEOS) as a silica source in acidic media[18], which was suggested to have an ordered cage-type pore structure with open windows, forming a continuous porous network. The SBA-1 materials have high surface area (> 1000 m^2/g) and pore volume with the pore diameter of about 2 nm.[32] The three-dimensional channel connectivity shown in Fig. 1-13 is considered to be suitable for its applications as a catalyst support and adsorbent. Among the ordered mesoporous materials, three-dimensional inter-connected pore structures are usually favorable to the one-dimensional array of pores due to better pore accessibility.[33,34,35]

Cubic
*Pm*3*n*
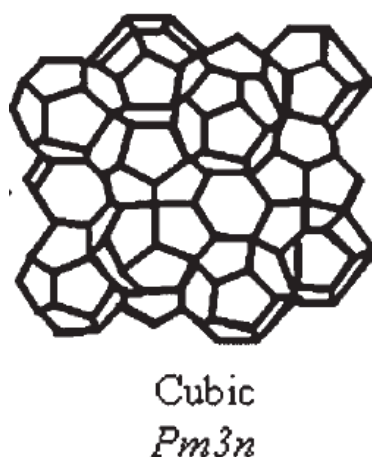
Fig. 1-13 Structure of SBA-1[36]

1.3.1 Phase transformation of SBA-1
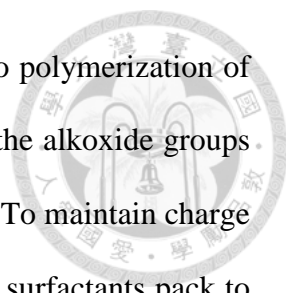
In 1999, Kim et al[37] changed various factor like synthesis procedure, acids, acid concentrations, surfactant with different chain length, amount of H_2O and TEOS in order to find the optimal synthesis condition for SBA-1. They found that the optimal

molar composition of reaction mixture is 1 CTEABr: 5 TEOS: 240-400 HCl: 3000-5000 H_2O and ^{29}Si MAS NMR confirmed that the cross-linking of SBA-1can be enhanced by heating reaction mixture at 373 K in the synthesis procedure. High-quality SBA-1 samples exhibiting well-resolved XRD peaks can be obtained following the procedure in this paper. In addition, this study presented a data that the acid anions may affect the mesostructure formation, ex. H_2SO_4 and HCl lead to the formation of the cubic phase, whereas HBr and HNO_3 lead to the hexagonal phase on the basis of Hofmeister series.

In early 2000, many research have been reported about the controlling the morphology[38] and mesostructure[39,40,41] of SBA-1 via reaction temperature, reaction time, various acids, CTEABr and acid concentration. At lower acidity or lower temperature, the crystallization is slowed and particular morphology having 54 or more crystal faces. The crystal faces became unclear with increasing synthesis temperature from -5 °C to 5 °C.[38]

Using different kind of acids in synthesis solution would influence strongly the mesostructure formation.[39,40] The effect of anions on the formation of mesostructures could be explained in terms of the adsorption strength on the headgroups of the surfactant micelle. Less strongly hydrated ions have in general smaller ionic radii and bind more strongly on the surface of the surfactant micelles and It also has been considered that the existence of the anion opposite to the surfactant headgroups would decrease the repulsion that efficiently decreases the a_o value. Therefore, Less hydrated anions led to the formation of the larger *g* parameter mesostructure.

Phase transformation could be observable during the synthesis with the time and this phase transition can be explained by the surfactant packing parameter *g*. In the cubic *Pm3n* phase synthesis system, the driving force from a hexagonal (higher *g*

parameter) to a cubic structure (lower *g* parameter) was attributed to polymerization of silica species, attributing that when silicate condensation proceeds, the alkoxide groups produce siloxane bonds and as a result the charge density decreased. To maintain charge matching in the interface between surfactants and silica species, the surfactants pack to form a high surface curvature to increase the effective headgroup area and lower the packing parameter so that the cubic mosophases with higher *g* parameters are favored. This phase transformation and silica condensation was confirmed by XRD and ^{29}Si MAS NMR, respectively[40]. Besides, lower CTEABr concentration, higher TEOS/CTEABr molar ratio, higher temperature and lower acidity are more favorable to form higher g parameter mesostructure and vise versa.[41]

In 2002, Liu et al[42] used *in-situ* time-resolved small angle X-ray scattering to study the intermediate phases formed during the formation of mesostructured silica film from aqueous–alcohol solution of CTMAB/TEOS. they found that the cubic structure of SBA-1 precipitate is stable upon heating, and the reaction temperature is not an important factor for phase transformation. The phase transformation from cubic to hexagonal occurred only when the wet precipitate was dried in open air and as a result drying the precipitate could be an important factor in obtaining mesostructure materials of different phases. Soon, Ogura et al[43] also used *in-situ* time-resolved small-angle X-ray scattering to research the relationship between the drying and phase transformation in detail. They found that the critical criteria for phase transformation are silicate flexibility and the number of H_2O molecules involved at the hydrophilic headgroup area of surfactant for the confinement of surfactant micelles. Prolonging the periods of synthesis time would make the silicate framework more rigid so that the phase transformation did not occur and this illustration is proposed in Fig. 1-14.

19
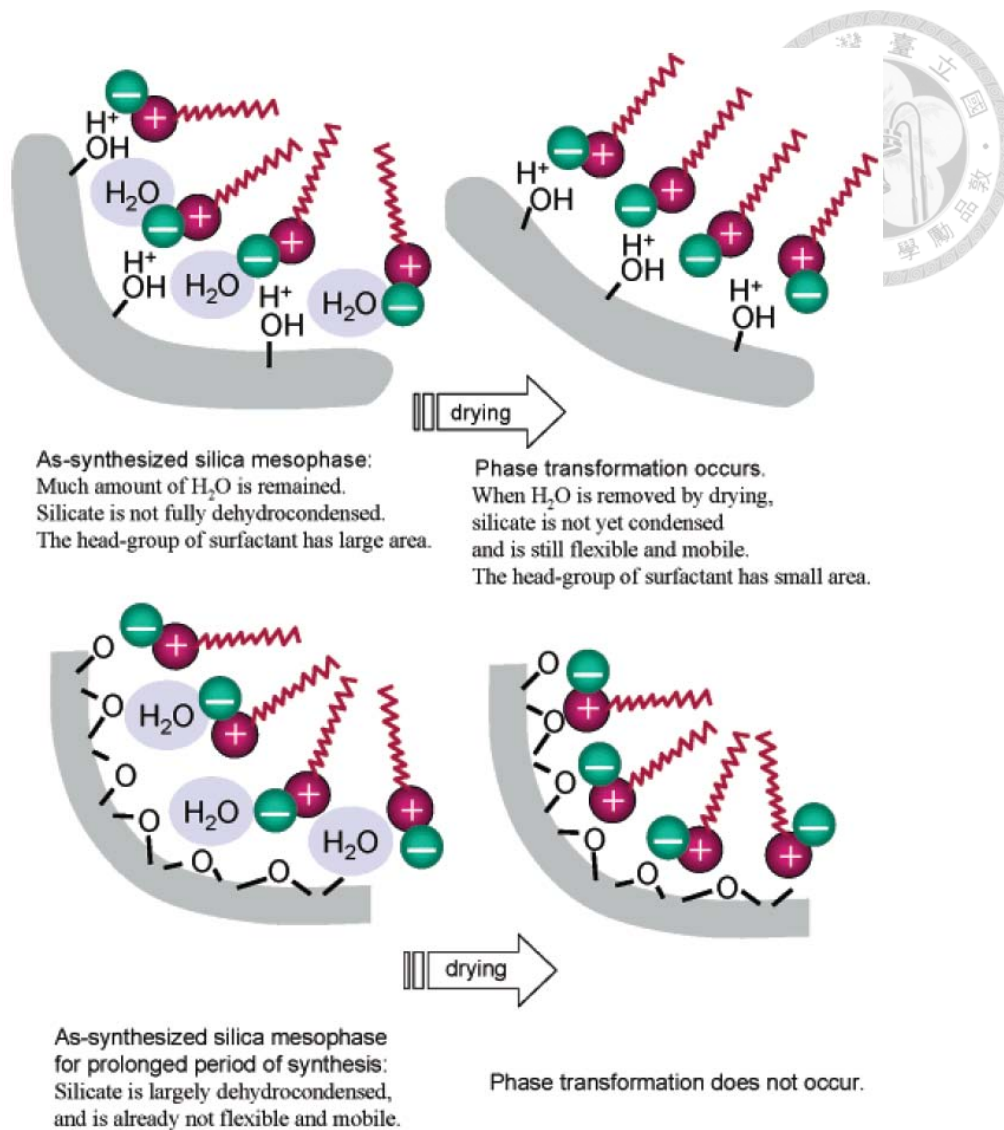
Fig. 1-14 Illustration for the surfactant molecules and silicate in the determined mesophase.[43]

In 2009, Liu et al[44] used the in situ fluorescence quenching experiment of pyrene to study that the anion present in the interface between the CTEA micelle and the silica wall are ready to be exchanged, accompanied by phase transformation and morphology change (Fig. 1-15). The mesostructure of the silica tends to transform from pore structure of low *g* value to that of high *g* value, or from a higher pore curvature toward lower one, which follows the Hofmeister series.
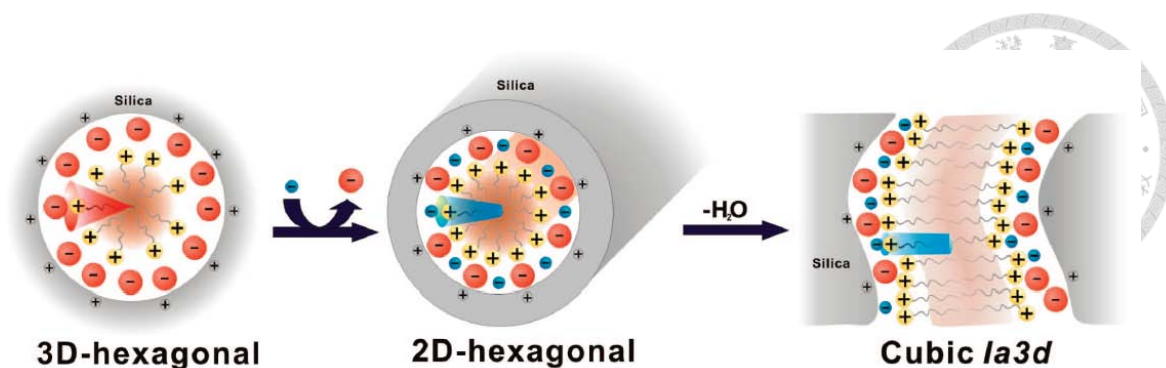
Fig. 1-15 Schematic representation of the mesophase transformation of silica precipitated in H_2SO_4 then ion-exchanged with NaSCN.[44]

1.3.2 Morphology changing of SBA-1

In 2003, Chao et al[45] first used the sodium silicate as a silica source and C_{18}TMACl as a surfactant to synthesize SBA-1 materials. They controlled the pH value of the reaction mixture in range of 1.0 - 2.0, contributing that the silica condensation rate is very slow in this pH value on the basis of silica chemistry. Due to the pH-dependence of the silica condensation rate, the shapes of as-synthesized SBA-1 mesoporous silica crystals show an evolution from sphere → decaoctahedron → truncated cube → cube as the pH value decreases from 1.0 to 2.0 (Fig. 1-16). Besides, this materials were also synthesized by using the surfactant with various chain length and different anions (C_nTMAX, n = 14 - 18; X = Cl or Br).[46]

21
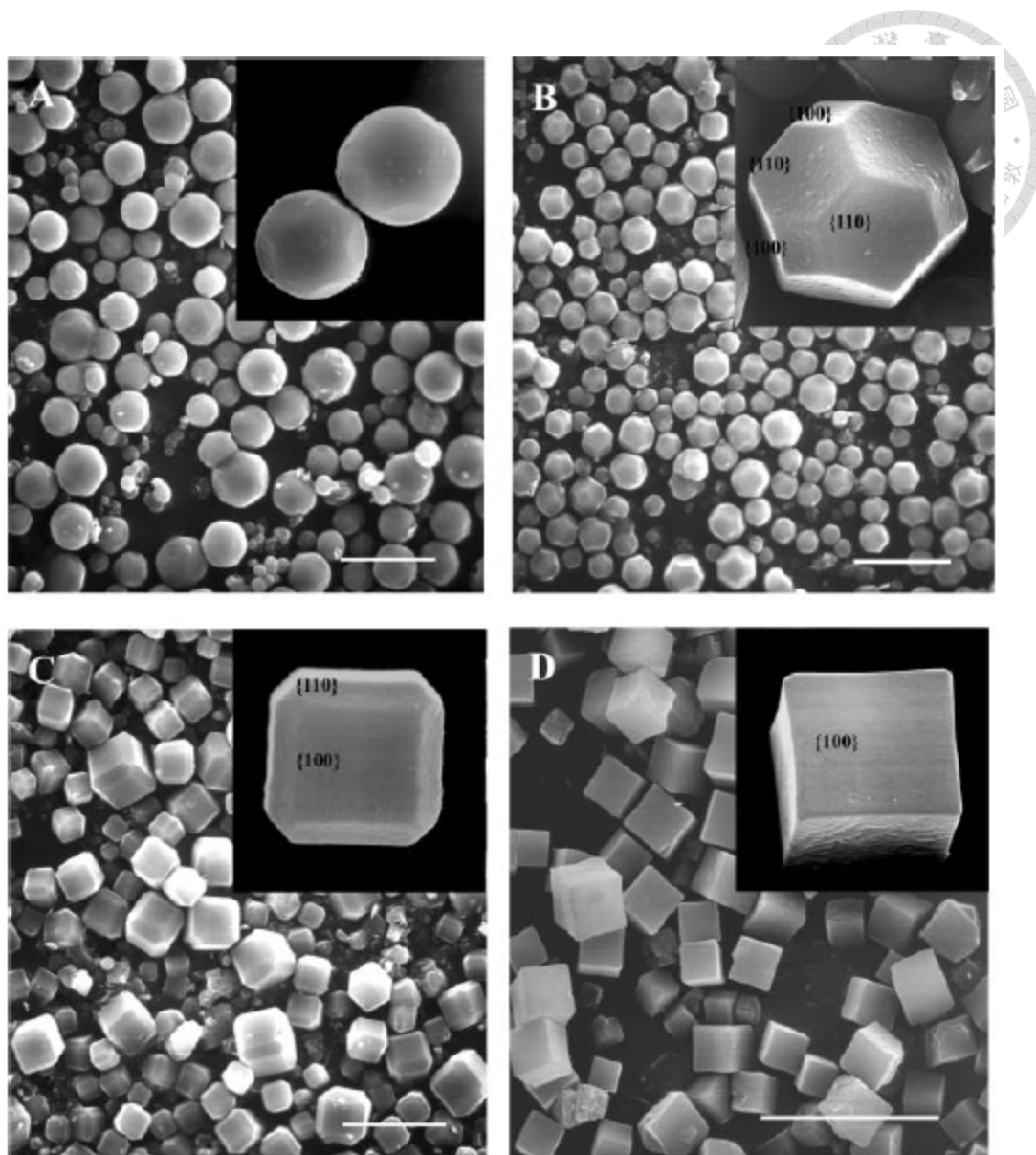
Fig. 1-16 Representative low-magnification SEM micrographs of the calcined
mesoporous silica of the samples：(A) pH = 1.0 (B) pH = 1.5 (C) pH = 1.8 (D) pH = 2.0.
The insets are the high-magnification SEM images of the representative SBA-1
mesoporous silica crystals. The scale bar = 15 μm.[45]

1.3.3 Synthesis of SBA-1 in alkaline solution

The drawback of the material from practical applications has been the low stability of the as-made samples toward washing with water.[32,37] Efforts have been made to overcome this disadvantage by increasing the amount and concentration of acid used[47] or concomitantly adding auxiliary agents[48,49]. On the other hand, under the strongly acidic synthesis condition, metal incorporation into SBA-1 has been very inefficient [50,51,52,53], though the incorporation of metal ions into the framework of mesoporous silica is important in order to introduce functionalities and broaden its applications.

Our laboratory has recently disclosed an alkaline route to prepare well ordered cubic *Pm3n* silica using sodium silicate as the silica source and cetyltriethylammonium bromide (CTEABr) as the pore-directing agent with the optimal pH value of the synthesis solution around 9.[54] The addition of a proper amount of salts such as NaCl was found essential in order to obtain materials of well-ordered cubic *Pm3n* mesoporous structure. In contrast to the conventional synthesis condition of SBA-1, where large amount of mineral acid is needed and tetraethylorthosilicate (TEOS) was the silica source, the alkaline route is more economical and environmentally friendly. Most of all, hetero-elements could be efficiently incorporated into the silica framework through isomorphous substitution and the cubic mesostructure of the resultant materials was stable toward washing with water and hydrothermal treatment.

1.4 Mesoporous zeolite

Various approaches for the preparation of mesoporous zeolites have been reported.[55,56,57,58,59] They can be classified into five categories: (i) partial crystallization of amorphous pore walls of mesoporous silica, (ii) using zeolite seeds as the building units of mesoporous framework, (iii) controlled dealumination and desilication of zeolitic materials, (iv) using carbon templating materials to incorporate mesopores during the synthesis of zeolites, and (v) assembly of mesoporous structures with zeolitic sheets.

1.4.1 Partial crystallization of amorphous pore walls of mesoporous silica

In this method, there two pathways to synthesize mesoporous zeolites. One involves two synthesis steps, preparation of an amorphous mesoporous materials followed by transformation of amorphous walls to crystalline walls by subsequent hydrothermal treatment in the presence of structure-directing agent (SDA) of zeolites. This way to position the appropriate amount of template molecules inside a mesoporous wall can lead to partial reacrystallization of amorphous wall and this materials exhibited high catalytic activity.[60,61]

The other is a one-step synthesis, based on the idea that the SDA could direct zeolite crystallization in the mesopore walls while the mesoporous structure was simultaneously formed according to the supramolecular templating mechanism of the surfactant micelles. In a typical synthesis, the surfactant was added into a gel composition for zeolite synthesis containing SDA and silica sources. Then the mixture is undergo the hydrothermal treatment at high reaction temperature and the mesoporous zeolite could be obtained.[62,63,64] These two way are often called "dual templating" method.

1.4.2 Using zeolite seeds as the building units of mesoporous framework

Zeolite seeds are nanoparticles containing the primary or secondary building units of zeolites and usually synthesized by shorten the hydrothermal time which results in the particle size of smaller than 10 nm. Using zeolite seeds as a silica source and surfactant as a template can synthesize the mesoporous materials with the zeolitic wall. The resultant materials exhibited well-ordered mesostructure, good hydrothermal stability and catalytic activity.[65,66,67,68,69]

1.4.3 Controlled dealumination and desilication of zeolitic materials

The strategy for this approach is the extraction of silica or Al from the zeolite through the chemical treatment in acids or bases. The alkaline treatment was explored as a post-synthesis tool to increase the mesoporosity inside zeolites. The selective extraction of framework silicon by treatment in alkaline solutions, referred to as desilication or base leaching, is now a widely used top-down method to prepare mesoporous zeolites. Desilication was firstly applied to study chemical changes of MFI crystals upon contact with NaOH aqueous solutions.[70,71] The first paper highlighting the presence of mesopores in ZSM-5 zeolites by framework silicon extraction in alkaline medium appeared in the year 2000 by the Matsukata group.[72] Recently, various studies have been reported according to this method.[73,74,75]

The dealumination process is typically applied to the high-Al zeolites. The steam-thermal dealumination of zeolite Y is the most well-known example.[76,77,78] Schematically the standard preparation procedure consists of two distinct steps. In a first step the original NH_4Y zeolite is submitted to hydrothermal treatment at high temperature (973-1073 K). The main effect of this treatment is to strongly dealuminize the zeolite framework. The vacancies created by the removal of tetracoordinated Al

25

atoms are likely to be filled by Si atoms. The second step of the preparation procedure is an acid leaching in a mineral acid. The main aim of this treatment is the solubilization of the extra-framework aluminium species created in the course of the calcination step.

1.4.4 Using carbon templating materials to incorporate mesopores during the synthesis of zeolites

The idea for this method is that the crystallization of a zeolite inside the pores of an inert matrix would prevent the zeolite crystals from growing any larger than the size of the pores in the matrix material. In a ideal case, open mesopores can be generated within microporous zeolite crystal by the subsequent removal of nanotemplates through calcination. Many carbon materials as a hard template have been used to synthesized mesoporous zeolites such as carbon nanoparticles, carbon nanotubes and carbon nanofiber.[79,80,81] In addition, carbon mesoporous molecular sieves (CMKs) are also used as a hard template. In 2004, Sakthivel et al.[82] and Yang et al.[83] reported that the mesoporous zeolites can be synthesized by using ordered CMK-1 (cubic structure) and CMK-3 (2D-hexagonal structure).

1.4.5 Assembly of mesoporous structures with zeolitic sheets.

Recently, Ryoo and co-workers[84] have explored bifunctional structure-directing agents, diquaternary ammonium surfactants, which is composed of the long alkyl chain and two alkyl-bridged ammonium head groups (Fig. 1-17). They combined the long alkyl chains usually present in amphiphilic templates for mesoporous solids with the cationic ammonium entities necessary for the formation of zeolitic micropores into a single template. The MFI nanosheets with thickness of one or two unit cell of zeolites are synthesized by using this bifunctional template. The ammonium head groups caused the silica precursor to form the microporous crystalline zeolitic framework while the

26

self-assembled surfactant tails directed the zeolite crystal morphology into a lamellar mesostructure and the schematically structure is shown in Fig. 1-18. Based on this concept, a series of bifunctional templates are prepared and tested them for order mesostructure and mesoporous zeolites. The gemini-type surfactants such as $C_{18}H_{37}$-$N^+(CH_3)_2$-C_6H_{12}-$N^+(CH_3)_2$-C_6H_{12}-$N^+(CH_3)_2$-$C_{18}H_{37}$ can generate ordered hexagonal mesoporous zeolites with mesopores of about 3 to 4 nm and the wall has the microporous crystallite framework.[85]
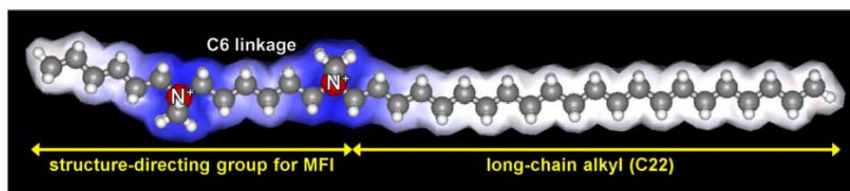
Fig. 1-17 Bifunctional cationic surfactant ($C_{22\text{-}6\text{-}6}$) directing porous structures in meso- and micro-length scales simultaneously.[84]
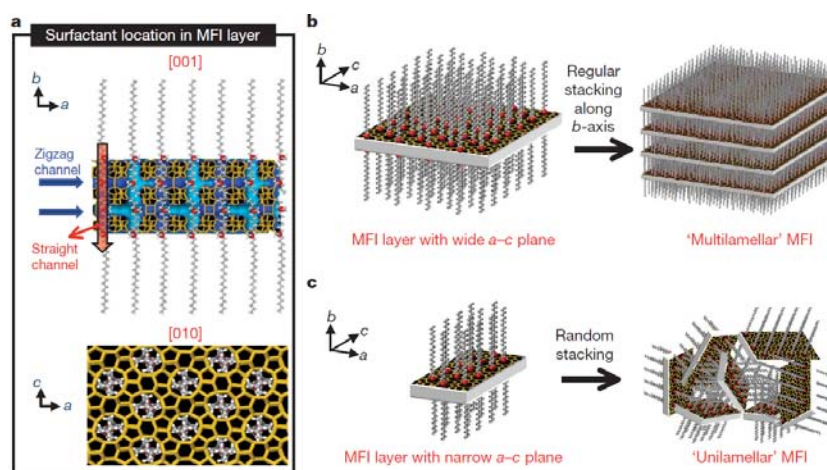
Fig. 1-18 Crystallization of MFI nanosheets.[84]

1.4.6 Al-incorporated SBA-1 with zeolitic wall

Among these methods mentioned above, the method using zeolite seeds as the building units of mesoporous framework has shown the advantage of facile control of

the mesostructure through changing different kinds of surfactants and hydrothermal conditions. It has been demonstrated that mesoporous zeolite catalysts prepared by this method exhibit high catalytic activities in acid-catalyzed reactions.[65,67,69]

In the present study, the effort was extended to synthesize cubic *Pm*3*n* silica assembled from aluminum substituted ZSM-5 seeds. The resultant materials were found to have higher hydrothermal stability and stronger acidic strength in comparison with the counter materials prepared from sodium silicate. The catalytic properties were examined by carrying out the alkylation of 2,4-di-*tert*-butylphenol (DTBP) with cinnamyl alcohol to form flavan as a model reaction[54, 86]. Flavans are a type of flavanoids, and flavanoids are a ubiquitous group of polyphenolic substances which are present in most plants preserving the health of plants against infections and parasites. Flavans have found numerous pharmacological applications as antioxidants [87], antimicrobial[88], anti-inflammatory and anti-cancer drugs[89].

1.5 Using Ti-incorporated SBA-1 as a support on direct phase propylene epoxidation reaction

1.5.1 Propylene oxide (PO) production

Propylene oxide is an important industrial feedstock for the production of polyethers and propylene glycol. The propylene oxide (PO) production processes that have been industrialized so far can be divided into two method: the traditional hydrochorination process and co-oxidation of propylene process with either isobutane or ethylbenzene.[90]

The hydrochlorination process involves reaction of propylene and chlorine in the presence of water to produce the two isomers of propylene chlorohydrin, 1-chloro-2-propanol or 2-chloro-1-propanol. This is followed by dehydrochlorination with base, usually aqueous sodium hydroxide or calcium hydroxide or lime to propylene oxide and salt. This process is schematically illustrated in Scheme 1-1. The major disadvantage of this process is environmental pollution, the production of chlorinated side products and a large amount of salts. Therefore, taking the environmental impacts into account, the most built plants are all using co-oxidation of propylene process technologies.
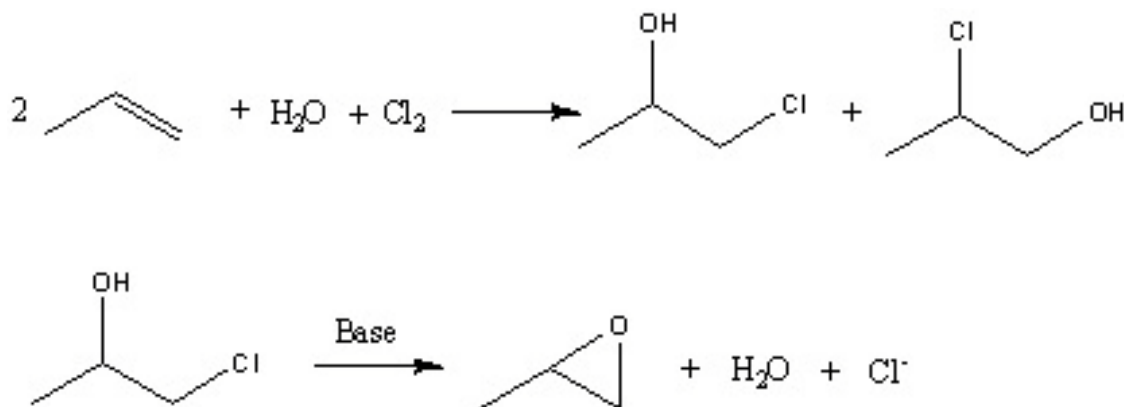
Scheme 1-1 hydrochlorination process

Scheme 1-2 show the co-oxidation process with the ethylbenzene. The ethylbenzene is reacted with oxygen to produce ethylbenzene hydroperoxide. The ethylbenzene hydroperoxide is subsequently used to epoxidize propylene to yield propylene oxide and methyl benzyl alcohol. In an alternative process, isobutane is substituted for ethylbenzene and, through the similar reaction pathway, tertiary butyl alcohol is the co-product. Methyl benzyl alcohol and tertiary butyl alcohol can then be dehydrated to styrene monomer and isobutylene for sale, respectively. This process is first developed by Halcon Corp. in 1960s.[91] A major disadvantage of these processes is that a co-product is produced in a fixed ratio, usually 2-4 times the amount of propylene oxide produced.
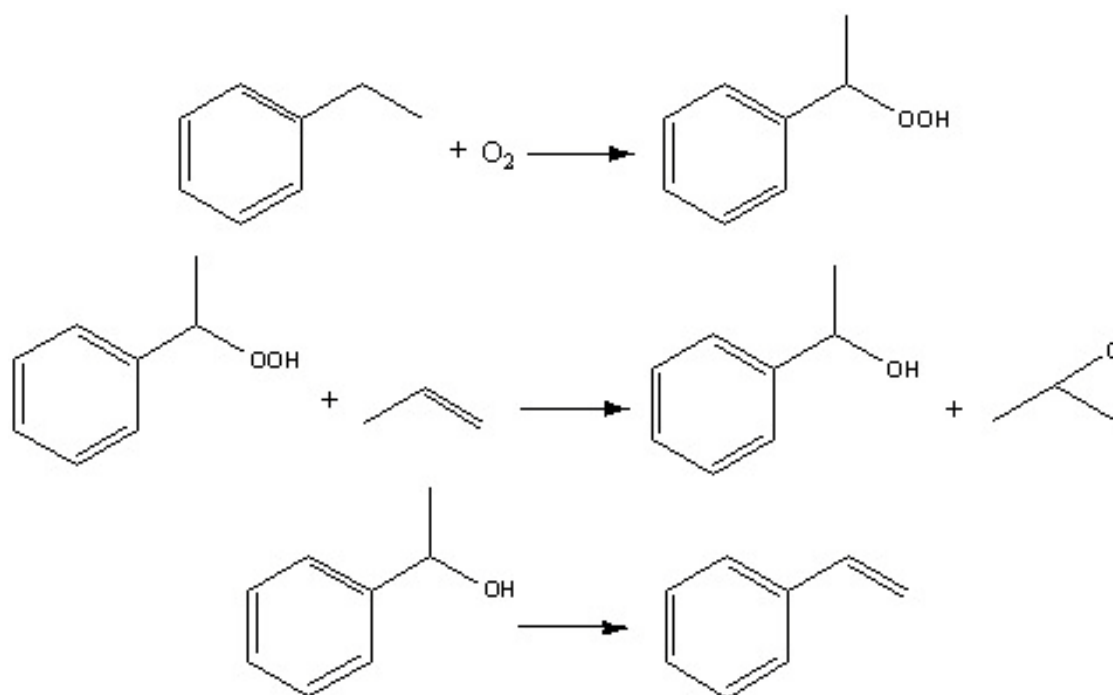
Scheme 1-2 Co-oxidation process

A process similar to the co-oxidation process is using cumene hydroperoxide as a oxidant and Sumitomo Chemical Company built up the plant for this process in 2003.[92]

In this process, cumene is oxidized by oxygen to obtain cumene hydroperoxide, which reacts with propylene to produce propylene oxide. The co-product, α,α-dimethyl benzyl alcohol can be recycled through hydrogenation back to cumene (Scheme 1-3).
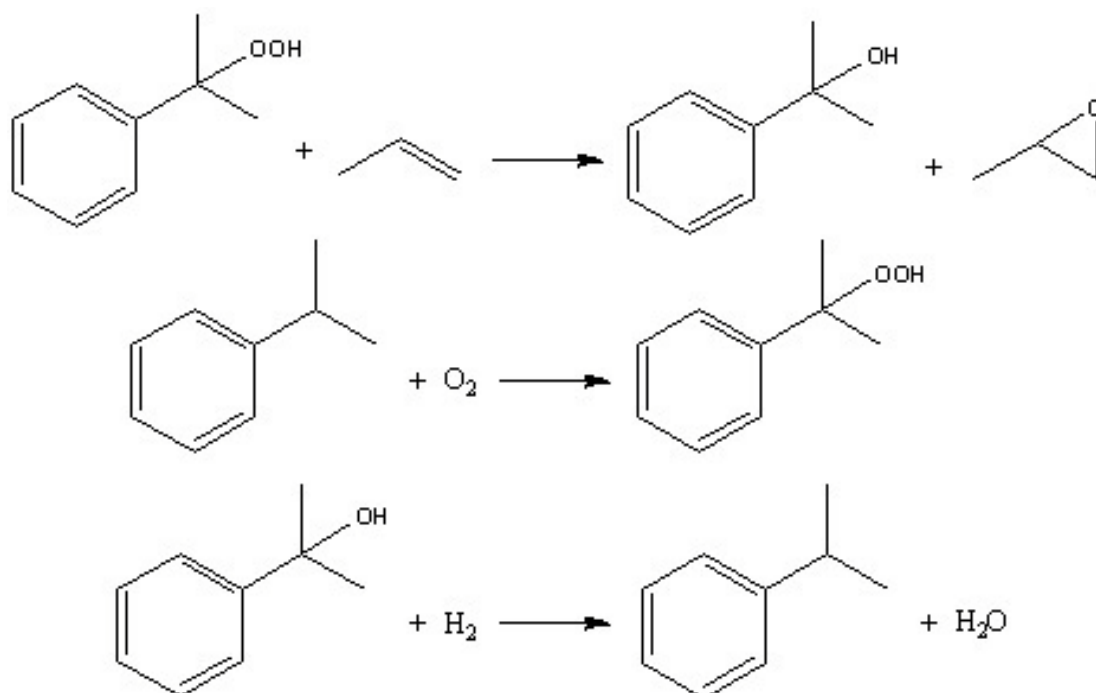
Scheme 1-3 Oxidation Process with cumene hydroperoxide

High propylene conversion and high propylene oxide yield can be obtained by using titanium silicalite-1 (TS-1) as a catalyst and alcohol as a solvent.[93,94] TS-1 is a molecular sieve with MFI structure and an average pore diameter of 0.55 nm.[95] This reaction is environment-friendly and the only co-product is water. However, the major problem for the commercialization of this process is high cost of hydrogen peroxide. In 2008, Dow Chemical and BASF built up a plant for hydrogen peroxide to propylene oxide (HPPO) process in Antwerp, Belgium[96] and this process can solve the problem of high cost of hydrogen peroxide.

1.5.2 Direct gas phase epoxidation of propylene with H_2 and O_2 over Au/Ti-support system

Since Haruta group[97,98] discovered that the gold nanoparticles supported on the Ti-incorporated materials give high selectivity to propylene oxide in direct gas phase epoxidation of propylene with mixture of H_2 and O_2 in 1998, various Ti containing supports have been reported such as Ti-MCM-41[99], Ti-MCM-48[100], Ti-SBA-15[101], Ti-HMS [102], Ti-SiO$_2$ [103], 3D mesoporous titanosilicates [104], Core-shell-structured TS-1@mesoporous silica[105] and TiO$_2$/SBA-15[106].
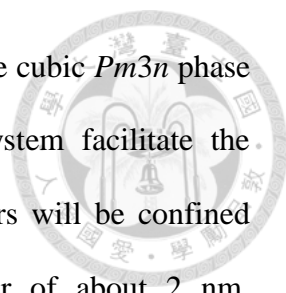
Besides, the gold particle size and its location play an important role for this reaction. So far there are two hypotheses about how large the particle size the more active is for direct gas phase epoxidation. In 2011, Huang et al[107] found that the gold clusters with the diameter of 1.0–2.0 nm on the external surfaces are more active for PO synthesis than tiny gold clusters inside the microporous channels of TS-1 by using HAADF-STEM combined with ^{129}Xe NMR and elemental analyses. However, the Delgass group[108,109] claimed that the gold clusters smaller than 1 nm inside the TS-1 channels can be active site for this reaction.

The mechanism for direct gas phase epoxidation was proposed by Oyama and Haruta group[110,111] by using in situ UV-Vis, EPR and XANES spectrum. The reaction pathways is schematically shown in Scheme 1-4: (1) synthesis of hydrogen peroxide from hydrogen and oxygen on gold nanoparticles; (2) formation of Ti-hydroperoxo or peroxo species from hydrogen peroxide on tetrahedral Ti centers; (3) reaction of propylene with the Ti-hydroperoxide species to form PO; and (4) decomposition of hydrogen peroxide to water.
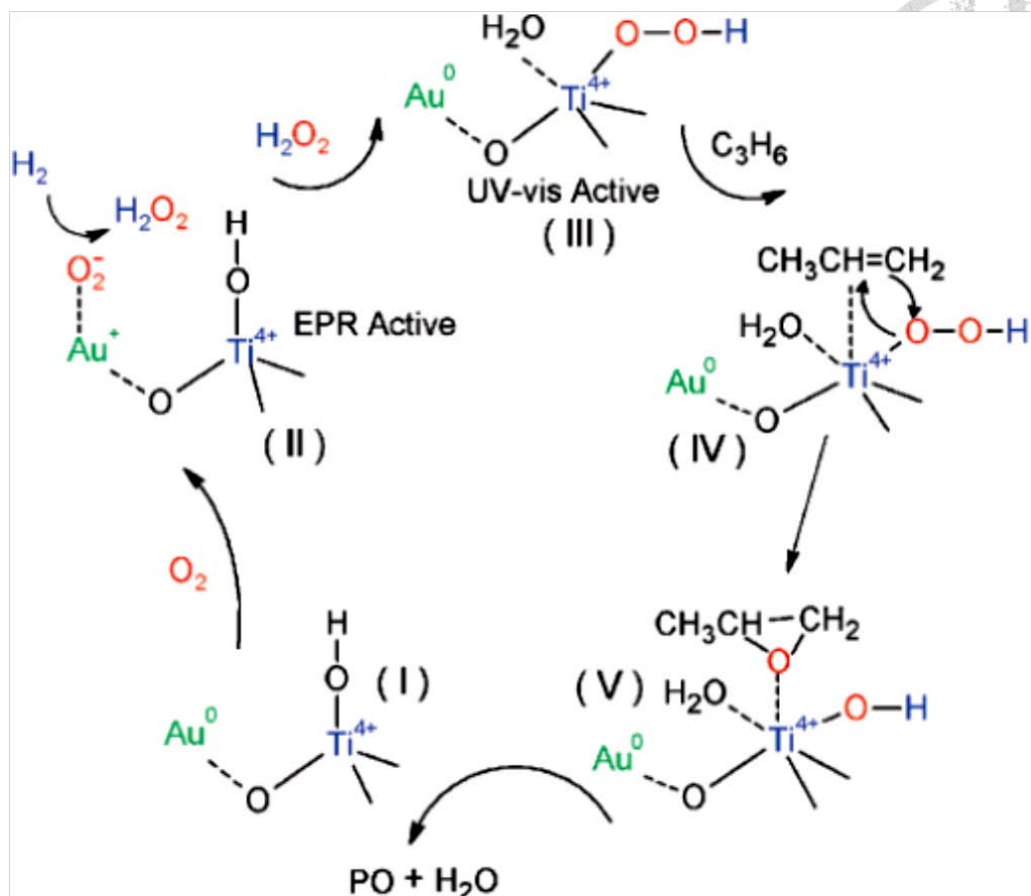
Scheme 1-4 Possible mechanism for propylene epoxidation with H_2 and O_2.[110]

One way to the promotion of reactivity is modification of the catalyst. The treatment of the support with NH_4NO_3[112], $In(NO_3)_3$[113], alkaline[114], alkaline earth metals[115], silylation[116], precipitation agent[117], and alkali salts[118] could effectively promote catalytic activity over catalysts. Huang et al[114]. reported that high PO rate, 137 g_{PO} h^{-1} kg_{cat}^{-1} at 200 ^{o}C, can be achieved by using a solid grinding (SG) method to deposit small gold clusters (<2 nm) on alkaline treatment TS-1. Another kind of promoter is trimethylamine (TMA), a strong Lewis base with a pKa value of 9.9. The catalytic performance, hydrogen efficient and deactivation can be improved by using TMA as a promoter in the reaction mixture.[119,120] Recently, some studies reported that using as-synthesized TS-1 as a support can improve the catalyst deactivation.[121,122]

33
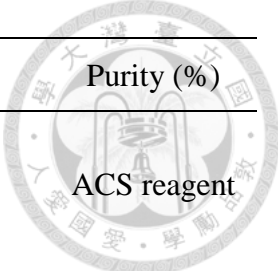
In this present study, our laboratory recently has synthesized the cubic $Pm3n$ phase SBA-1 in alkaline condition[54] and its three-dimensional pore system facilitate the diffusion of products, PO or acrolein. We expect that gold clusters will be confined insides the pores of SBA-1 materials having the pore diameter of about 2 nm, preventing the aggregation of gold clusters during reaction. The size of gold clusters insides the pores will be about 2 nm, which is more active for direct gas phase epoxidation reaction.[107] Besides, in order to enhance the catalytic performance and improve the deactivation, Ti-incorporated SBA-1 materials with zeolitic wall are prepared by using TS-1 seeds as silica source and CTEABr as surfactants.

Chapter 2   Experimental

2.1 Reagents

Name	Brand	Purity (%)
Triethylamine	Tedia	99.9
1-bromohexadecane	Acros	97
Sodium chloride	Acros	99.5
Hydrochloric acid	Aencore	37
Sodium silicate solution	Sigma-Aldrich	27
Tetrapropylammonium bromide	Alfa Aesar	98+
2,4-di-*tert*-butylphenol	Acros	97
Cinnamylalcohol	Sigma-Aldrich	98
4-*tert*-butylphenol	Alfa Aesar	99
Ammonium chloride	Acros	99.5
2,2,4-trimethylpentane	Acros	99.5
Acetonitrile	Echo	99.99
Dimethyacetamide	Acros	99
Octane	Acros	99+
Sodium Aluminate	Hanawa Chemical pure	
Titanium tetraisopropoxide	Acros	98+
Tetrapropylammonium hydroxide solution	Acros	25
Sodium hydroxide	Acros	98.5
Tetramethylammonium chloride	Acros	98+
Tetrabutylammonium bromide	Acros	99+

Name	Brand	Purity (%)
Tetrachloroauric acid trihydrate ($HAuCl_4 \cdot 3H_2O$)	Acros	ACS reagent
Propene oxide	Acros	99.5
Ethanal	Riedel-de haen	99.5
Acetone	Merck	99.5
Acrolein	Fluka	99.5
N_2	豐明	99.995
H_2	豐明	99.999
He	豐明	99.995
O_2	豐明	99.99
Propene	豐明	99.99

2.2 Cubic *Pm3n* mesoporous aluminosilicate assembled from zeolite seeds as strong acidic catalysts

2.2.1 Preparation of Al(III)-incorporated cubic *Pm3n* mesoporous silica under alkaline condition

Al-incorporated *Pm3n* mesoporous silica materials designated "xAl-SBA-1-alk", where x is the Al/Si molar percentage in the synthesis solution, were prepared referred to the procedures in reference 54. CTEABr was first dissolved in an aqueous solution containing sodium chloride and a small amount of hydrochloric acid. To this mixture at 273 K, the aqueous solution containing sodium aluminate and sodium silicate with Al/Si atomic ratios varied in 1-7% was added so that the pH value of the final solution was kept around 9. The molar composition of the reaction mixture was $Na_2SiO_3/NaAlO_2/CTEABr/NaCl/ H_2O= 1.0/0.01–0.07/0.26/6/500$. After stirring for 10 min, the mixture was aged at 273 K for 24 h. The solid product was recovered by filtration, washing thoroughly with deionized water, and drying at 373 K overnight. To remove the template, the as-synthesized samples were calcined in air under static condition at 823 K for 10 h with the heating rate of 10 K/min.

2.2.2 Preparation of Al(III)-incorporated ZSM-5 seeds

The ZSM-5 seeds were prepared referred to the procedures in reference 123, except all the reagents were diluted to 3.5 times to avoid the precipitation of zeolite. The solutions containing 1.5 g sodium silicate, 0.58 g tetrapropylammonium bromide (TPABr), 9.6 g deionized water and required amounts of $NaAlO_2$ were neutralized with 1.2 M H_2SO_4 until a final pH of 11.2. After stirring at ambient temperature for 1 h, the mixture was transferred to autoclave and heated at 423 K under static condition for different hours with various amount of Al content (1 h for 1%, 12 h for 3%, 24 h for 5%,

24 h for 7%).

2.2.3 Preparation of cubic *Pm3n* mesoporous silica assembled from Al(III)-incorporated ZSM-5 seeds

The procedures were similar to those for preparation of Al-SBA-1-alk, except Al(III)-incorporated ZSM-5 seeds were used as the silica and aluminum sources. The resultant materials are designated "xAl-ZSBA-1" , where x is the Al/Si molar percentage in the synthesis solution.

The flow charts of preparation of Al-SBA-1-alk and Al-ZSBA-1 samples are shown as followed:

Synthesis of Al-SBA-1-alk

$2.36g\ NaCl + 40g\ H_2O + HCl$

↓ stirred for 10 min

$0.712\ g\ CTEABr \longrightarrow$ ↓ stirred for 2 h at RT

↓ stirred for 1 h at 273 K

Certain amount of NaAlO$_2$ + sodium silicate + 20 g H$_2$O $\longrightarrow$ ↓ stirred for 10 min

↓ stayed at 273 k for 24h

↓ filtered, washed, dried and calcined at 823 K for 10 h

Na^+-Al-SBA-1-alk

↓ ion-exchanged by 1 M NH$_4$Cl for 4 h (100mL/1g SiO$_2$) twice

↓ filtered, washed, dried and then calcined

xAl-SBA-1-alk

x: Al/Si molar percentage

$(1Si：0.01\text{-}0.07Al：6NaCl：0.26CTEABr：500H_2O)$

Synthesis of Al-ZSBA-1

certain amount of $NaAlO_2$ + 6.8 g H_2O

↓ stirred for 30 min

1.5 g sodium silicate ⟶ ↓ stirred for 30 min

0.58 g TPABr + 2.8 g H_2O ⟶ ↓ stirred for 30 min

↓ added 1.2 M H_2SO_4 until pH=11.2

↓ stirred for 1 h

↓ transferred to autoclave at 423 k
for hydrothermal reaction

Na^+-ZSM-5 seeds

2.36 g NaCl + 40 g H_2O + HCl

↓ stirred for 10 min

0.712 g CTEABr ⟶ ↓ stirred for 2 h at RT

↓ stirred for 1 h at 273 K

ZSM-5 seeds ⟶ ↓ stirred for 10 min

↓ stayed at 273 k for 24 h

↓ filtered, washed, dried and
calcined at 823 K for 10 h

Na^+-Al-ZSBA-1

↓ ion-exchanged by 1 M NH_4Cl for
4 h (100mL/1g SiO_2) twice

↓ filtered, washed, dried and then calcined

xAl-ZSBA-1
x: Al/Si molar percentage
(1Si：0.01-0.07Al：6NaCl：0.26CTEABr：500H_2O)

2.2.4 Acid capacities measurement

The accessibility of Brønsted acid sites in the materials was determined by ion-exchange with cations of various sizes followed by acid-base titration. Aqueous solutions of sodium chloride (NaCl, 2 M), tetramethylammonium chloride (TMACl, 0.05 M), and tetrabutylammonium bromide (TBABr, 0.05 M) were used as the exchange agents. In a typical experiment, 0.20 g of the solid dried at 200 °C for 1 day was added to 40 mL of aqueous solution containing the corresponding salt. The suspension was mixed to reach equilibrium for 6 h, then the solid was filtered and washed with a small amount of water. Finally, the filtrate was titrated by an aqueous solution of 0.01 M $NaOH_{(aq)}$.

2.2.5 Catalytic reaction procedure

To generate Brønsted acid sites on Al-SBA-1-alk and Al-ZSBA-1, the calcined samples were ion-exchanged with 1 M NH_4Cl aqueous solution twice, followed by filtration, washing with deionized water, drying at 373 K and calcination at 823 K. Before catalytic test, the catalyst was baked at 473 K at least for 5 h to remove adsorbed moisture. The alkylation of 2,4-di-*tert*-butylphenol (DTBP) with cinnamyl alcohol was performed in a 50 mL flask immersed in a thermostat bath with a magnetic stirrer. 100 mg of the catalyst suspended in 12.5 mL solvent was mixed with 0.25 mmol of DTBP (Aldrich) and 0.25 mmol of cinnamyl alcohol (Aldrich), and the reaction was proceeded at 368 K for different reaction periods. After quenching to room temperature, the liquid products were separated from the solid catalyst by filtration and analyzed by a Shimadzu GC-2014 gas chromatograph (GC) equipped with a flame ionization detector (FID) and a RTX-5 capillary column (30 m*0.53 mm) using octane as an internal standard. The side products such as oligomer and 2,4,6-tri-*tert*-butylphenol can't be

detected by FID due to their high boiling points. The turnover over frequency is calculated and defined as follows:

$$TOF\ (h^{-1}) = \frac{\text{mole of DTBP converted}}{\text{mole of active sites (mole of Al content)} \times \text{reaction time (hours)}}$$

Fig. 2-1 and Fig. 2-2 show the NMR spectra of 2,4-di-*tert*-butyl-6-cinnamylphenol (DTBCP) and flavan, respectively. Flavan and DTBCP are not commercialized. The product and intermediate standard are synthesized as followed: 5 g DTBP and 4 g cinnamyl alcohol are mixing with stirring and then one drop of conc. H_2SO_4 is added. After the mixture is reacted for 24 h, flavan and DTBCP can be purified by chromatography. The chromatography is packed by silica gel and the elution is hexane.

The DTBP conversion and flavan yield are defined as followed:

$$DTBP\ conv. = \frac{(\text{initial mole of DTBP} - \text{final mole of DTBP})}{\text{initial mole of DTBP}}$$

$$\text{flavav yield} = \frac{\text{mole of flavan}}{\text{theoretical mole of flavan}}$$

the final mole of DTBP and mole of flavan are both calculated by calibration curve.
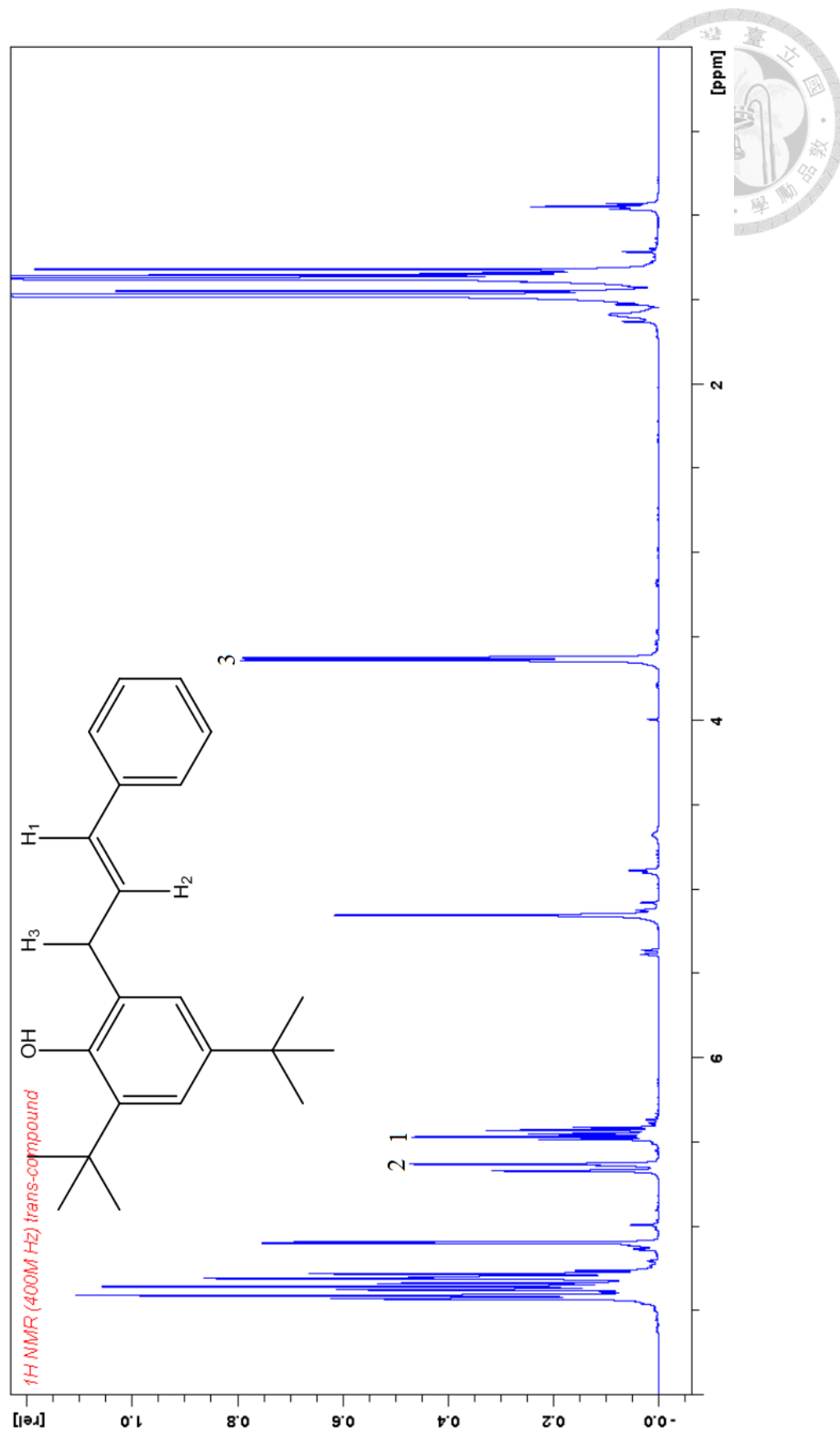
Fig. 2-1 ^{1}H NMR spectra of DTBCP.
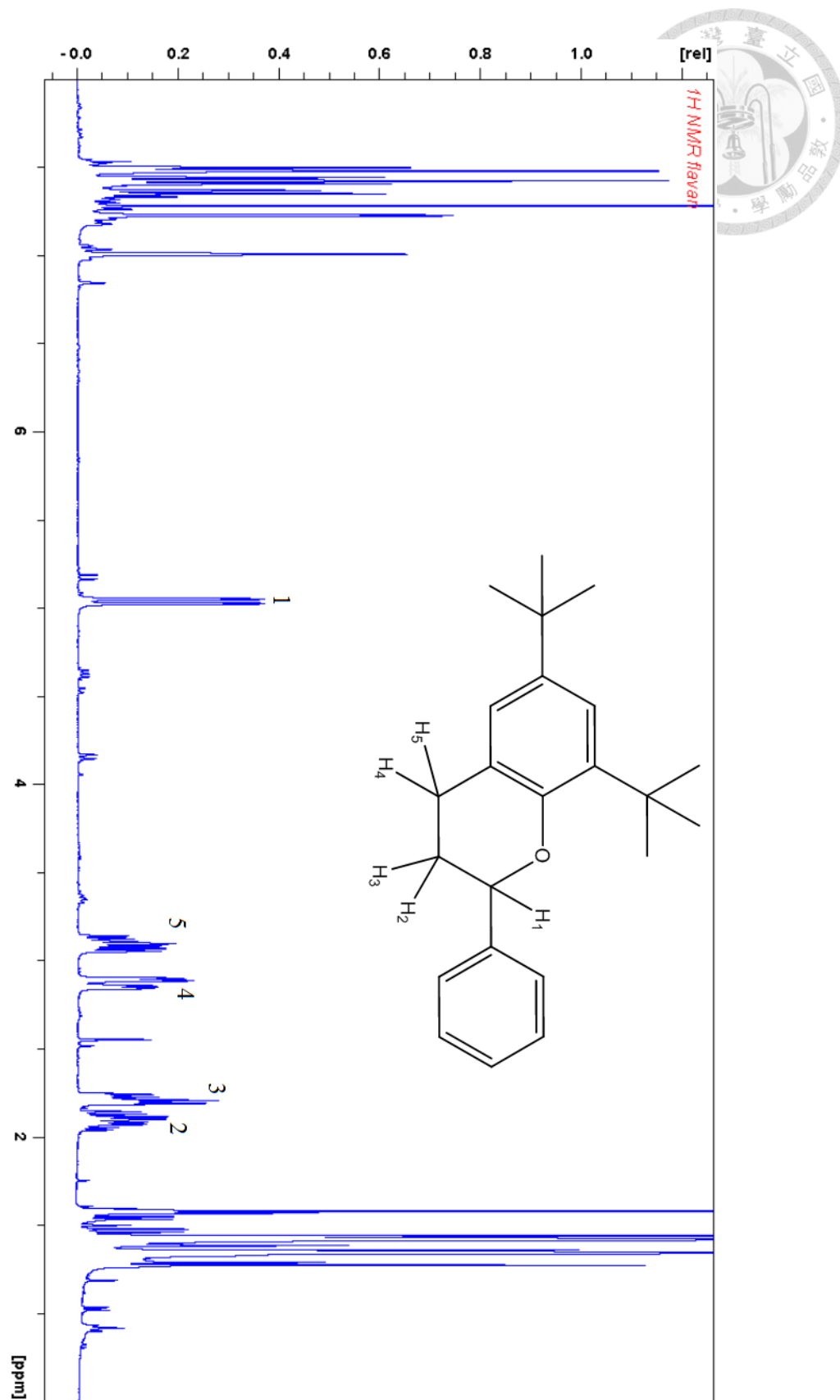
Fig. 2-2 ^{1}H NMR spectra of flavan.

2.3 Direct gas phase epoxidation of propylene over Au/Ti-SBA-1

2.3.1 Preparation of Ti-incorporated cubic *Pm3n* mesoporous silica under alkaline condition

Ti-incorporated *Pm3n* mesoporous silica materials designated "xTi-SBA-1-alk", where x is the Ti/Si molar percentage in the synthesis solution, were prepared referred to the procedures in reference 54. CTEABr was first dissolved in an aqueous solution containing sodium chloride and a appropriate amount of hydrochloric acid so that the pH value of the final solution was kept around 9. After stirring for 90 min at room temperature, the titanium tetraisopropoxide (TTIP) was added and then this mixture was stirred for 30 min followed by cooled down to 0 $^{\circ}$C. After stirring for 60 min, sodium silicate was added. The molar composition of the reaction mixture was Na_2SiO_3/ TTIP/ CTEABr/ NaCl/ HCl/ H_2O = 1.0/ 0.01–0.05/ 0.13/ 3/ 0.60/ 200. After stirring for 10 min, the mixture was aged under static condition at 0 $^{\circ}$C for 24 h. The solid product was recovered by filtration, washing thoroughly with deionized water, and drying at 100 $^{\circ}$C overnight. To remove the template, the as-synthesized samples were calcined in air under static condition at 550 $^{\circ}$C for 10 h.

2.3.2 Preparation of Ti-incorporated SBA-1 materials with zeolitic wall

Ti-incorporated SBA-1 materials with zeolitic wall were prepared by using TS-1 seeds as silica source and CTEABr as surfactant. First, the TS-1 seeds were prepared referred to the procedures in reference 124 . In a typical procedure, tetraethylorthosilicate (TEOS) and TTIP were properly mixed with stirring at room temperature for 30 min. Then, 4.8 g tetrapropylammonium hydroxide (TPAOH) aqueous solution was added drop-wise into the previous mixture under vigorous stirring. Subsequently, 3.3 g H_2O was added to this mixture. The molar composition of the TS-1

seed solution was TEOS/ TTIP/ TPAOH/ H_2O = 1.0/ 0.01–0.05/ 0.44/ 28.5.The resulting clear solution was transferred to autoclave and heated at 90 $^{\circ}$C under static condition for 20 hours.

0.712 g CTEABr was dissolved in the aqueous solution containing 2.32 g sodium chloride, a appropriate amount of hydrochloric acid and 41.5 g H_2O. After stirring for 120 min at room temperature, this mixture was cooled down to 0 $^{\circ}$C in ice bath and stirred for 60 min. Then, TS-1 seed solution was added to this mixture under stirring. The molar composition of the final mixture was TEOS/ TTIP/ TPAOH/ CTEABr/ NaCl/ H_2O = 1.0/ 0.01–0.05/ 0.44/ 0.13/ 3/ 200. After stirring for 10 min, the mixture was aged under static condition at 0 $^{\circ}$C for 24 h. The solid product was recovered by filtration, washing thoroughly with deionized water, and drying at 100 $^{\circ}$C overnight. To remove the template, the as-synthesized samples were calcined in air under static condition at 550 $^{\circ}$C for 10 h. The resulting samples were denoted as xTi-ZSBA-1 and x represent the Ti/Si molar percentage.

2.3.3 Gold deposition

The method of gold deposition is using deposition-precipitation (DP) method. In a typical synthesis, a required amount of hydrogen tetrachloroaurate(III) trihydrate ($HAuCl_4 \cdot 3H_2O$) was first dissolved in 25 mL deionized water and then the aqueous solution of 1 M NaOH was added dropwise to this solution until the pH value reached 6.0. Subsequently, 0.5 g support was added and the pH value of this suspense solution was adjusted to 7.0. Finally, the solid was filtered, washed with deionized water and dried in vacuum conditions at room temperature. The gold samples were denoted as yAu^{3+}/xTi. or yAu^{3+}/xTiZ. (x and y represent the Ti/Si molar percentage and Au/support weight percentage in the synthesis solution, respectively.) The yAu^{3+}/xTiZ sample was

using Ti-incorporated SBA-1 materials with zeolitic wall as a support.

The flow charts of synthesis of various samples are shown as followed:

Synthesis of Ti-SBA-1

1.18 g NaCl + 15 g H_2O + 0.46 g HCl

|stirred for 10 min

0.356 g CTEABr ——→

stirred for 1 h at RT

TTIP ——→

stirred for 0.5 h at RT

stirred for 1.5 h at 273 K

1.5 g sodium silicate + 8 g H_2O ——→

stirred for 10 min

stayed at 273 K for 24 h

filtered, washed, dried and
calcined at 823 K for 10 h

aTi-SBA-1-alk

a: Ti/Si molar percentage

Si/Ti/CTEABr/NaCl/HCl/H_2O = 1/0.01 – 0.05/0.13/3/0.70/200

The pH value of final solution is 8.5 ~ 9.

Synthesis of Ti-ZSBA-1

2.8 g TEOS + required amount of TTIP

stirred for 10 min

4.8 g 20 wt% TPAOH aqueous solution →

stirred for 10 min

3.3 g H$_2$O →

stirred for 10 min

transferred to autoclave at 90 °C for 20 h

TS-1 seed (clear solution)
Si/Ti/TPAOH/H$_2$O = 1/0.01-0.05/0.44/28.5

2.32 g NaCl + 38.5 g H$_2$O + HCl

stirred for 10 min

0.712 g CTEABr →

stirred for 2 h at R.T.

stirred for 1 h at 273K

TS-1 seed →

stirred for 10 min at 273 K

stay at 273 K for 24 h

Filtered, washed, dried and calcined at 823 K for 10 h
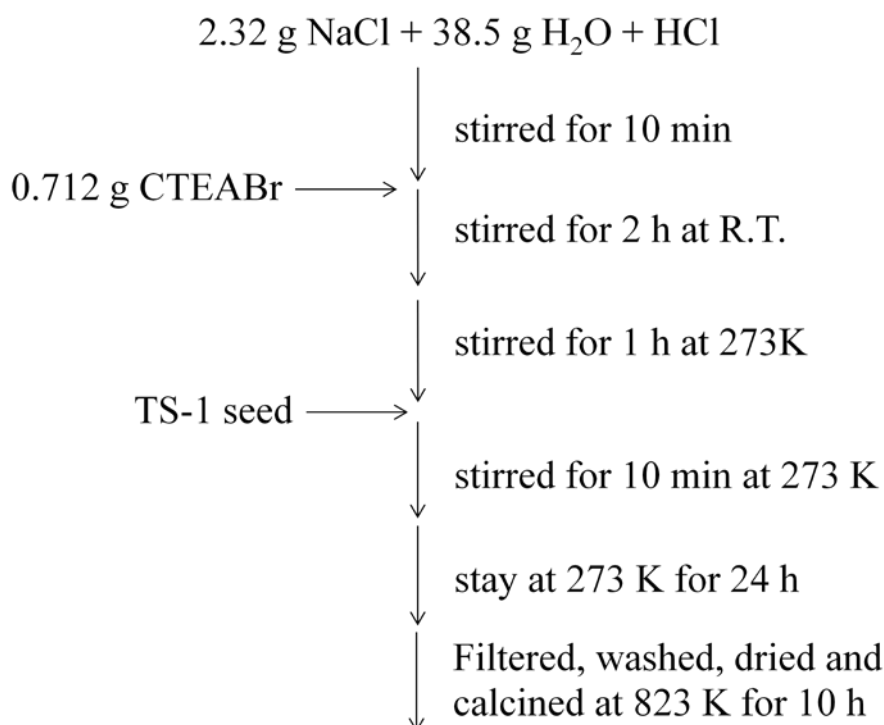
aTi-ZSBA-1
a: Ti/Si molar percentage
Si/Ti/CTEABr/NaCl/H$_2$O = 1/0.01 − 0.05/0.13/3/200
The pH value of final solution is 8.5 ~ 9.

Gold deposition

required amount of $HAuCl_4 \cdot 3H_2O$ + 50 g deionized water

| pH was adjusted to 6 by adding 1 M $NaOH_{(aq)}$

1 g support $\longrightarrow$

| pH was adjusted to 7 by adding 1 M $NaOH_{(aq)}$

| Filtrated, washed and dried under vacuum at RT
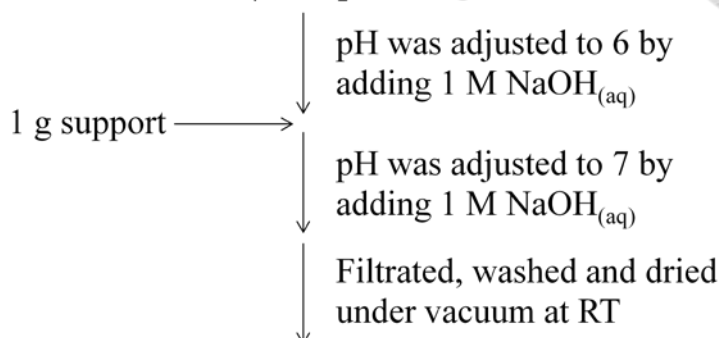
$10Au^{3+}/aTiZ$

a: Ti/Si molar percentage

2.3.4 Catalytic reaction procedure

Before catalytic tests, the catalyst was first dried under vacuum at room temperature overnight and then 0.3 g of catalyst was weighed and loaded in a packed bed within a quartz-tubular reactor. The catalyst was pretreated by heating to 160-200 $^{\circ}C$ under He flow with the heating rate 1 $^{\circ}C$/min and holding for 30 min. The catalytic measurements were carried out under atmospheric pressure in the reaction gas mixture (C_3H_6/ O_2/ /H_2/ He= 10/ 10/ 10/ 70vol%) with a flow rate of 25 mL/min. The products were analyzed by using a Shimadzu GC-14B gas chromatography equipped with a flame ionization detector (propylene, PO, ethanal, acetone and acrolein) and a thermal conductivity detector (H_2, O_2 and CO_2), attached to a CP-Wax 52 CB capillary column and a 60/80 Carboxen-1000 packed column, respectively. The catalyst was denoted as yAu/xTi. The designs for ten-port valve and catalytic reactor are schematically shown in Scheme 2-1 and Scheme 2-2. The propylene conversion, PO selectivity, H_2 conversion and H_2 selectivity were calculated and defined as follows:

48

$$\text{propylene conversion} = \frac{\text{mole of } (C_{3-\text{oxygenates}} + \frac{1}{3} CO_2)}{\text{mole of propylene in feed}}$$

$$\text{PO selectivity} = \frac{\text{mole of PO}}{\text{mole of } (C_{3-\text{oxygenates}} + \frac{1}{3} CO_2)}$$

$$H_2 \text{ conversion } (\%) = \frac{\text{mole of } (H_2 \text{ in feed} - H_2 \text{ in products})}{\text{mole of } H_2 \text{ in feed}}$$

$$H_2 \text{ selectivity} = \frac{\text{mole of PO}}{\text{mol of } H_2 \text{ converted}}$$
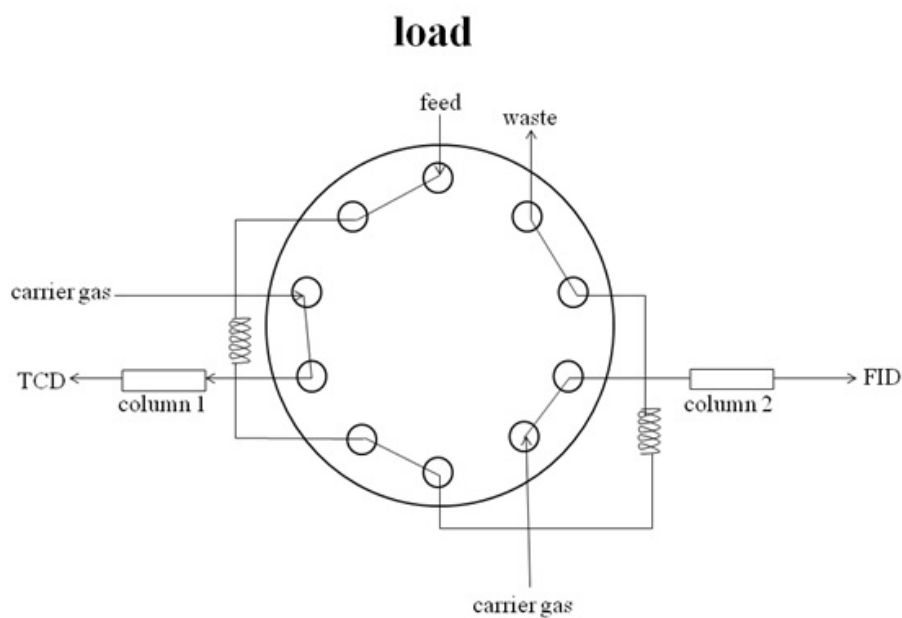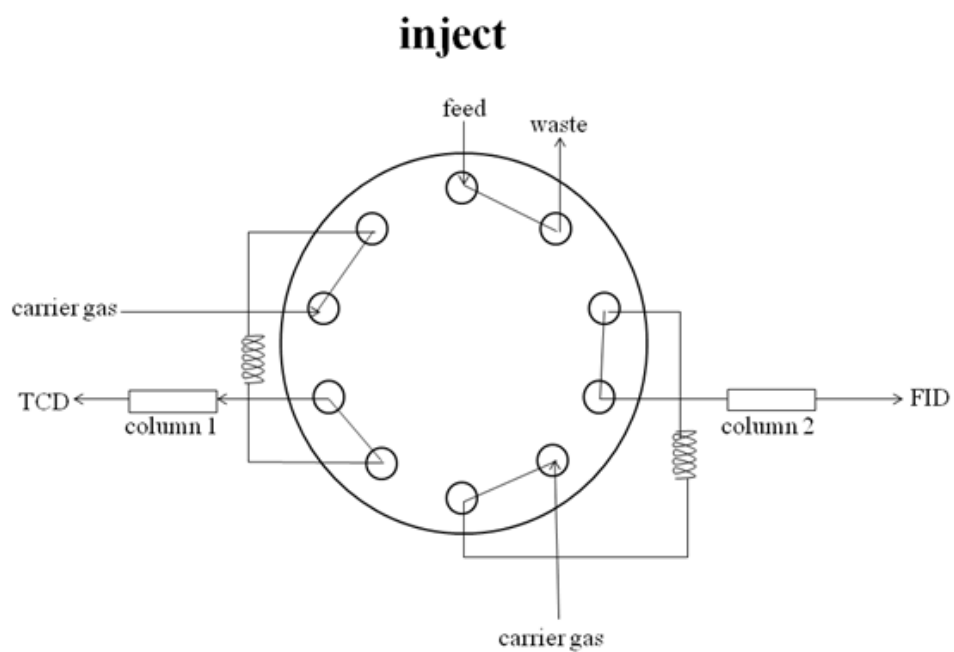
Scheme 2-1 Ten-port valve design for load and inject

1. Gas cylinders
2. Flow controllers
3. Three way valve
4. Additives
5. Quartz tube
6. Catalyst
7. 10 port valve
8. GC
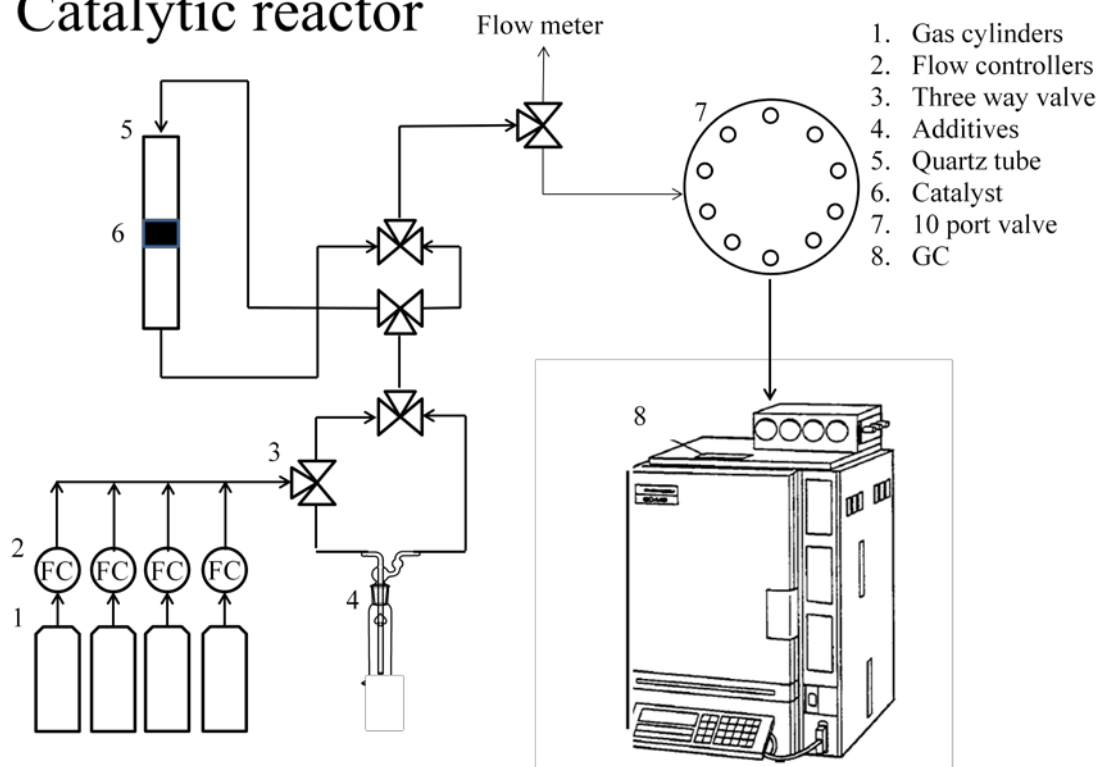
Scheme 2-2 Design for catalytic reactor

2.4 Characterization

2.4.1 Powder X-ray diffraction

Powder X-ray diffraction (XRD) patterns were recorded using a PANalytical X'pert Pro diffractometer with Cu $K\alpha$ radiation operated at 40 mA and 45 kV. A powder X-ray diffractometer consists of an X-ray source (usually an X-ray tube), a sample stage, a detector and a way to vary angle θ. The X-ray is focused on the sample at some angle θ, while the detector opposite the source reads the intensity of the X-ray it receives at 2θ away from the source path. The incident angle is than increased over time while the detector angle always remains 2θ above the source path (Fig. 2-3). The interaction of the incident rays with the sample produces constructive interference (and a diffracted ray) when conditions satisfy Bragg's Law ($n\lambda=2d\sin\theta$, λ: wavelength of X-ray radiation, d: the distance between two layers). This law relates the wavelength of electromagnetic radiation to the diffraction angle and the lattice spacing in a crystalline sample.
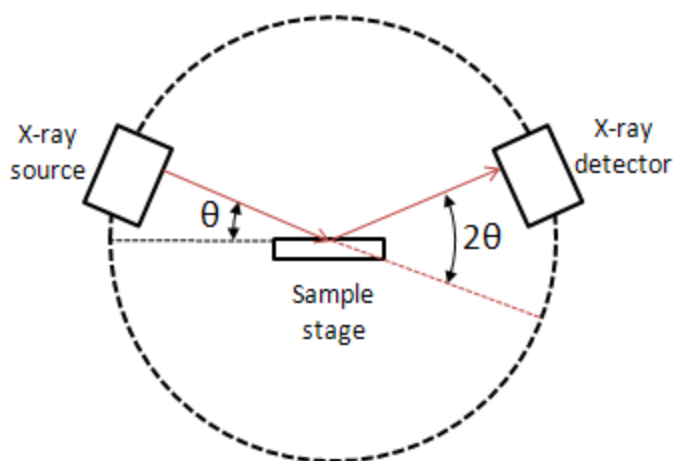
Fig. 2-3 Instrumentation of XRD

2.4.2 N_2 adsorption-desorption isotherm

N_2 sorption isotherms were measured using a Micromeritics Tristar 3000 system at liquid nitrogen temperature (77 K). Before the measurements, the samples were degassed at 323 K for 10 h under vacuum (10^{-3} Torr). The surface area was calculated by using Brunauer-Emmett-Teller (BET) method[125]. The BET equation is

$$\frac{1}{v[(p_o/p) - 1]} = \frac{c - 1}{v_m}\left(\frac{p}{p_o}\right) + \frac{1}{v_m c}$$

where p and p_o are the equilibrium and the saturation pressure of adsorbates at the temperature of adsorption, v is the adsorbed gas quantity (for example, in volume units), and v_m is the monolayer adsorbed gas quantity. c is the constant,

$$c = \frac{E_1 - E_L}{RT}$$

where E_1 is the heat of adsorption for the first layer and is E_L that for the second and higher layers and is equal to the heat of liquefaction. BET equation is an adsorption isotherm and can be plotted as a straight line with $1/v[(p_o/p) - 1]$ on the y-axis and (p/p_o) on the x-axis according to experimental results. This plot is called a BET plot. The linear relationship of this equation is maintained only in the range of $0.05 < p/p_o < 0.35$. The value of the slope, S and the y-intercept, I of the line are used to calculate the monolayer adsorbed gas quantity, v_m and the BET constant, c. The following equations can be used:

$$v_m = \frac{1}{S + I} \text{ and } c = 1 + \frac{S}{I}$$

Finally the BET surface area is given by

$$S_{BET} = \frac{a \times N \times v_m}{m \times V}$$

where N is Avogadro's number, a is the adsorption cross section of the adsorbing

species, V is the molar volume of the adsorbate gas and m is the mass of the adsorbent.

Pore size was determined by Barrett-Joyner-Halenda (BJH) method using the desorption branch of the isotherms. The BJH method is based on a model of the adsorbent as a collection of cylindrical pores[126]. The theory accounts for capillary condensation in the pores using the classical Kelvin equation, which in turn assumes a hemispherical liquid-vapor meniscus and a well-defined surface tension. Condensation occurs in pores that already have some multilayer on the walls (Fig. 2-4). Kelvin equation is shown as followed:

$$\ln\frac{p}{p_o} = \frac{2 \times \gamma \times V_m}{R \times T \times r_m}$$

where γ is the surface tension, V_m is the molar volume of the liquid, R is the universal gas constant, r_m is the radius of the droplet and T is temperature. The two common equation used for calculating the statistical thickness (t) are shown as below:

$$t = \left[\frac{13.99}{0.034 - \log(^p/_{p_o})}\right]^{1/2} \text{Harkins} - \text{Jura equation}$$

$$t = 3.54\left[\frac{5.00}{\ln(^p/_{p_o})}\right]^{1/3} \text{Halsey equation}$$

Therefore, the pore radius, r_p is calculated from the Kelvin equation and the selected statistical thickness equation ($r_p = r_k + t$ and $r_k = r_m\cos\theta$).
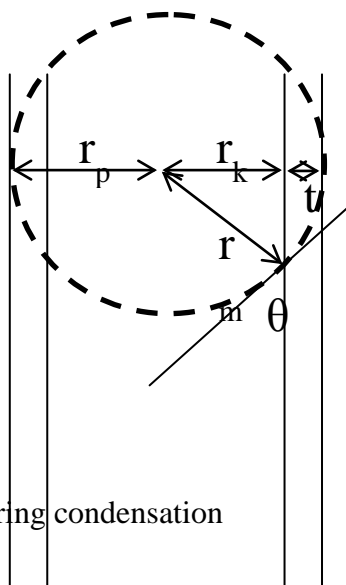
Fig. 2-4 Multilayer appear during condensation

2.4.3 Electron microscopy (EM)

Transmission electron microscopy (TEM) was performed on a JEOL JEM-1200EX II Transmission Electron Microscope, operating at 80 kV, and the scanning electron microscopy (SEM) images were taken using a Cold-field emission Scanning Electron Microscope (Hitachi S-4800).

2.4.4 Solid state NMR

The ^{27}Al MAS NMR experiments were carried out at frequencies 78.21 MHz on a Brucker MSL-300 NMR spectrometer equipped with a commercial 4 mm MAS-NMR probe. The magic-angle spinning frequencies were set to 12 kHz for all experiments. Chemical shifts were externally referenced to $Al(NO_3)_3$.

2.4.5 Inductively-coupled plasma-mass spectrometry

The inductively-coupled plasma-mass spectrometry (ICP-MS) of the samples dissolved in HF aqueous solutions were taken by using an Agilent 7700e ICP/MS instrument. In detail, 20 mg sample was placed into the Teflon cup. Then, 1 mL conc.

$HF_{(aq)}$, 1 mL conc. $HNO_{3(aq)}$ and 1 mL conc. $HCl_{(aq)}$ were added. The clear solution was obtained and diluted to ppm level by deionized water.

2.4.6 Temperature-programmed desorption

Temperature-programmed desorption of ammonia (NH_3-TPD) was performed by a Micrometrics Autochem 2910 system equipped with a thermal conductivity detector (TCD). Prior to the measurements, the samples (ca. 300 mg) were pre-treated at 823 K for 1 h under a He flow to eliminate physically adsorbed water. The samples cooled to 373 K then adsorbed NH_3 for 30 min, followed by purging with He gas again for another 30 min to eliminate physically adsorbed ammonia. The NH_3-TPD profiles were measured over the temperature range of 373-823 K by using He as a carrier gas of 30 mL/min.

2.4.7 X-ray absorption spectroscopy

The Ti K-edge and Au L_3-edge X-ray absorption spectroscopy was obtained at the beam lines 17C of National Synchrotron Radiation Research Center (NSRRC) at Hsinchu, Taiwan. Standard operating condition was 1.5 GeV and 300 mA. The photon energy was calibrated using pure Ti foil (K-edge, 4966 eV) and Au foil (L3-edge, 11919 eV). X-ray absorption spectroscopy end-station in BL17C1 hutch is shown in Fig. 2-5. The end station has setups for performing X-ray absorption experiments on various types of samples including liquids and solids. Of particular research interest is the study of catalytic reaction using EXAFS technique. The end station contains gas-ionization chambers with associated electronics for transmission mode, a Lytle detector coupled with various filters for fluorescence mode and a total electron yield detector (operating with helium flushing).
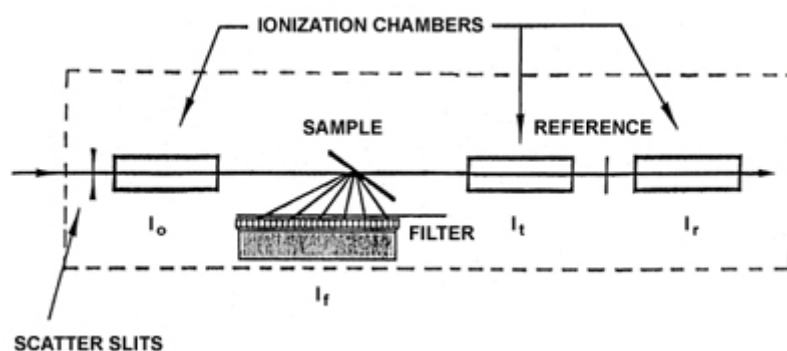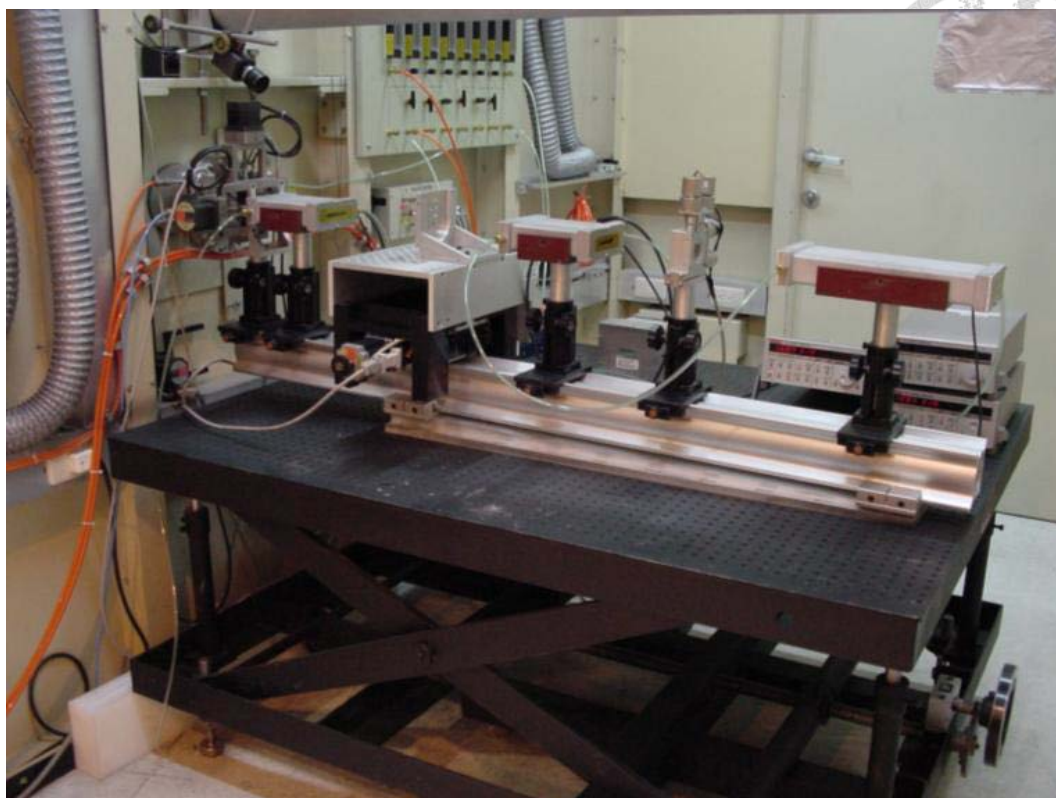
Fig. 2-5 End-station in BL17C1 hutch

2.4.8 Diffuse-reflectance UV-Vis spectroscopy

Diffuse-reflectance UV-Vis spectra were taken by a Hitachi U-3310 spectrometer equipped with an integrating sphere detector using $Ba(SO)_4$ as a reference material. The y-axis is calculated by using the Kubelka-Munk theory. The theory which makes possible to use diffuse-reflectance spectra was proposed by Kubelka and Munk[127].

Originally they proposed a model to describe the behavior of light traveling inside a light-scattering specimen (Fig. 2-6), which is based on the following differential equations:

$$-di_T = -(S + K)i_T dx + Si_R dx$$

$$di_R = -(S + K)i_R dx + Si_T dx$$

where i_T and i_R are the intensities of light traveling inside the sample towards its un-illuminated and illuminated surfaces, respectively; dx is the differential segment along the light path; S and K are the so called K-M scattering and absorption coefficients, respectively. A limiting assumption is that the particles making up the layer must be much smaller than the total thickness. Both absorbing and scattering media must be uniformly distributed through the sheet. Ideally, illumination should be with diffuse monochromatic light and observation should be of the diffuse reflectance of the paper. The theory works best for optically thick materials where > 50% of light is reflected and < 20% is transmitted. In the limiting case of an infinitely thick sample, thickness and sample holder have no influence on the value of reflectance (*R*). In this case, the Kubelka-Munk equation at any wavelength becomes as followed:

$$\frac{K}{S} = \frac{(1 - R_\infty)^2}{2R_\infty} \equiv F(R_\infty)$$

$F(R_\infty)$ is the so-called remission or Kubelka-Munk function, where $R_\infty = R_{sample}/R_{standard}$.
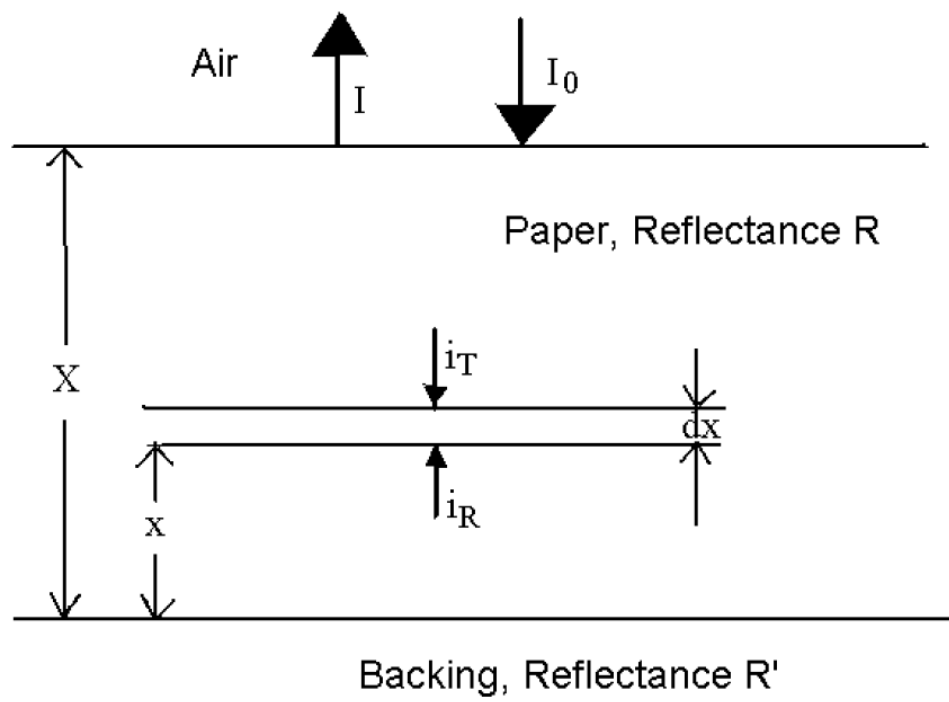
Fig. 2-6 skin spectral model

Chapter 3 Cubic *Pm*3*n* mesoporous aluminosilicate assembled from zeolite seeds as strong acidic catalysts
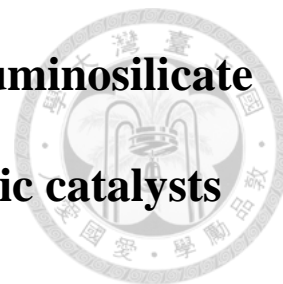
3.1 Characterization

Fig. 3-1~Fig. 3-4 show the XRD patterns of as-synthesized Al-ZSM-5 with various Al loadings for different hydrothermal time. The characteristic peaks of MFI structure are present at different time for different Al loading. For 1Al-ZSM-5 material, no peaks are observable at the hydrothermal time of 1 h and after the hydrothermal time of 3 h, ZSM-5 crystal is formed shown in Fig. 3-1. The crystallization time will delay for the ZSM-5 with higher Al loadings. For examples, the induction periods of 3Al, 5Al and 7Al-ZSM-5 samples are 36 h, 96 h, and 96 h, respectively (Fig. 3-2~Fig. 3-4). It is indicated that the higher Al loadings, the longer the induction period and the lower the crystallization rate. These results are similar to the reference 128. The large ZSM-5 crystals are not suitable to be a seed for preparation of mesoporous materials with zeolitic wall. Therefore, the hydrothermal time of 1 h for 1Al-ZSM-5, 12 h for 3 Al-ZSM-5, 24 h for 5Al-ZSM-5 and 24 h for 7Al-ZSM-5 are the better choice.
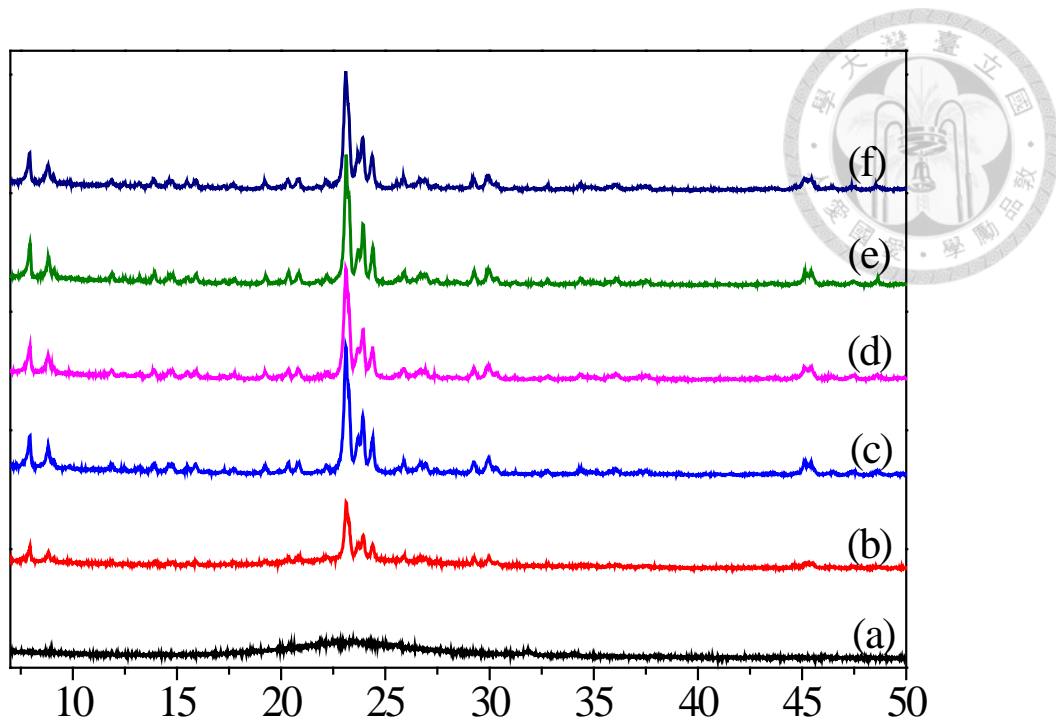
Fig. 3-1 XRD patterns of as-synthesized 1Al-ZSM-5 for different hydrothermal time: (a)

1 h (b) 3 h (c) 6 h (d) 12 h (e) 18 h (f) 24 h
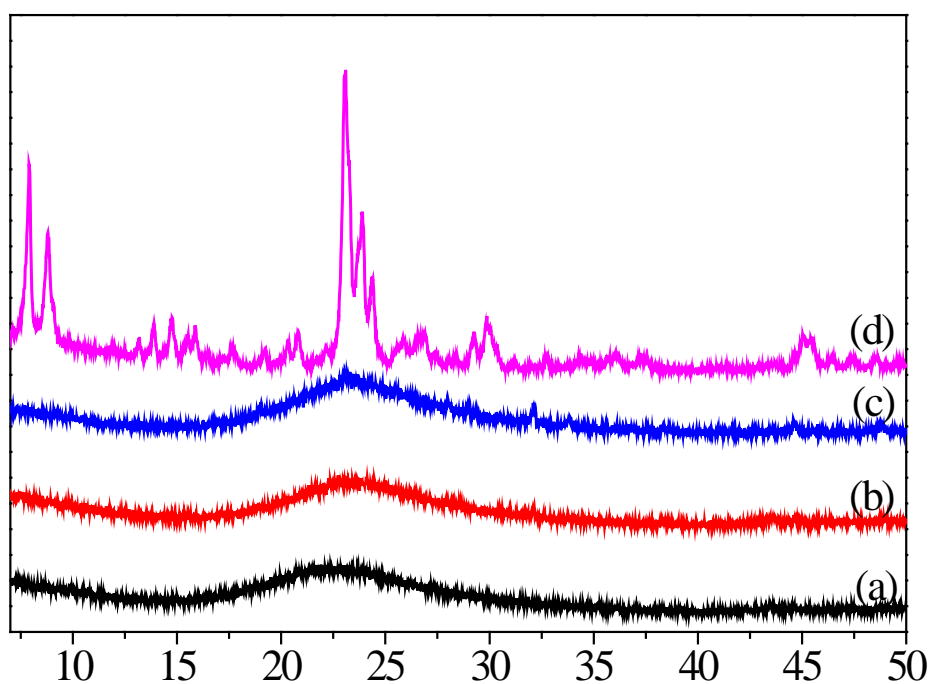
Fig. 3-2 XRD patterns of as-synthesized 3Al-ZSM-5 for different hydrothermal time: (a)
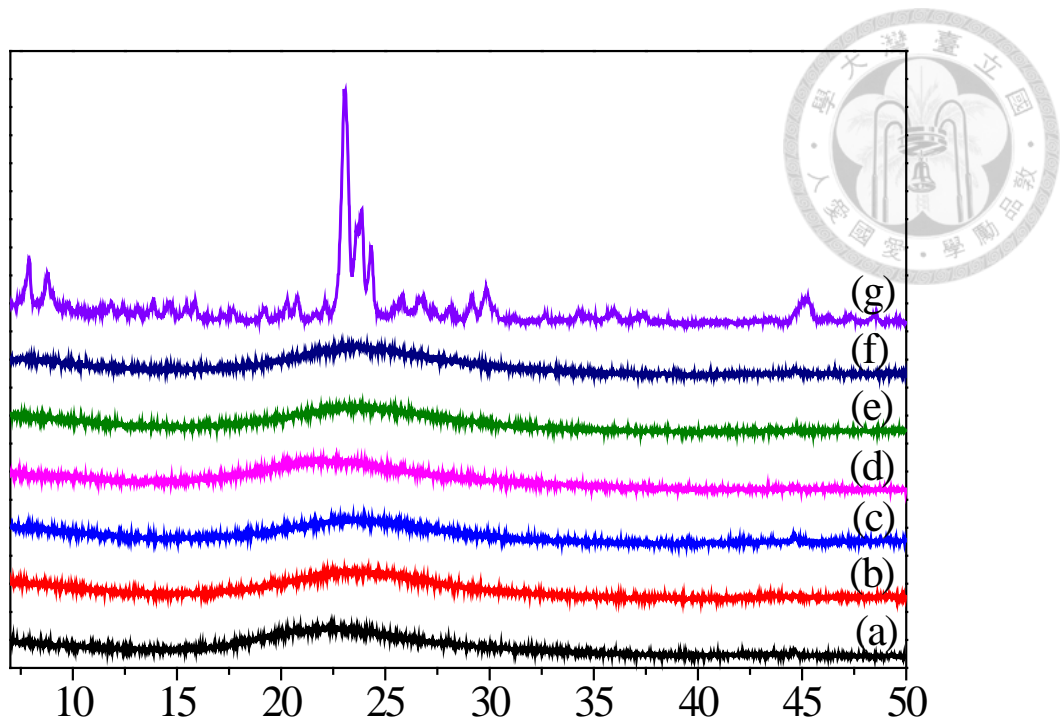
12 h (b) 18 h (c) 24 h (d) 36 h.

Fig. 3-3 XRD patterns of as-synthesized 5Al-ZSM-5 for different hydrothermal time: (a) 12 h (b) 18 h (c) 24 h (d) 36 h (e) 48 (f) 72 h (g) 96 h.
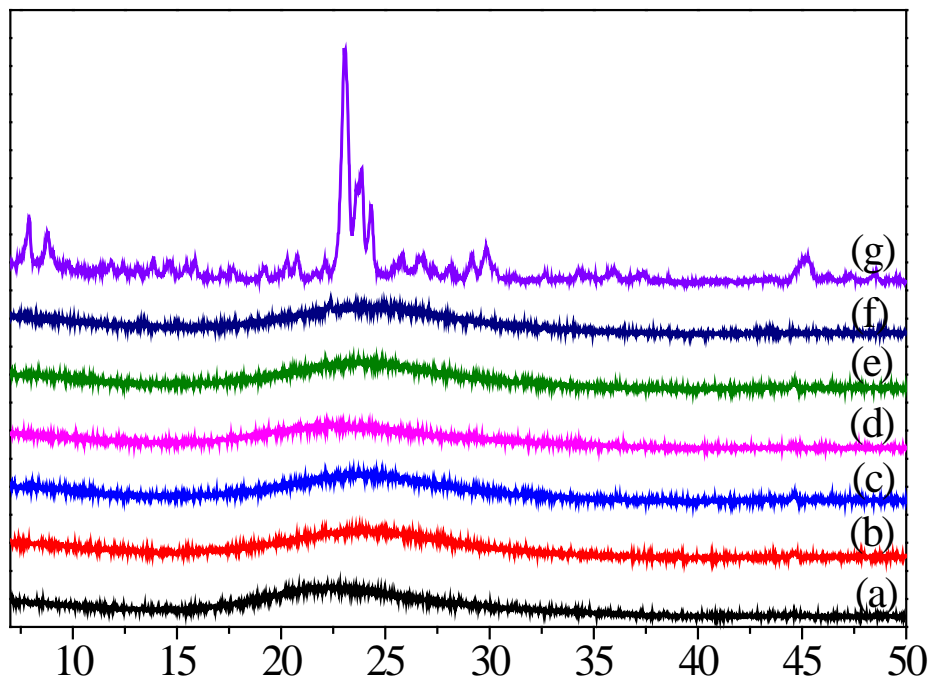
Fig. 3-4 XRD patterns of as-synthesized 7Al-ZSM-5 for different hydrothermal time: (a) 12 h (b) 18 h (c) 24 h (d) 36 h (e) 48 (f) 72 h (g) 96 h.
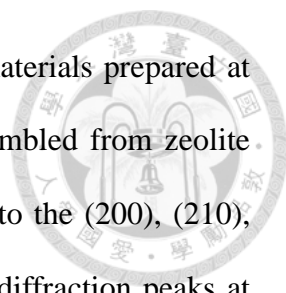
Fig. 3-5 shows the XRD patterns of the calcined Al-SBA-1 materials prepared at pH 9. The XRD patterns of the calcined Al-ZSBA-1 samples assembled from zeolite seeds show three distinct diffraction peaks at 2θ~1.5-2.5° indexed to the (200), (210), and (211) planes of cubic *Pm3n* symmetry, and also some weaker diffraction peaks at 2θ~3-4° assigning to the (222), (320), (321), and (400) planes.[19] The calcined Al-ZSBA-1 samples with Al/Si molar percentages lower than 5% still retain three resolvable diffraction peaks at 2θ~1.5-2.5°, while the one synthesized with Al/Si = 7% has only a broad peak in this region. These results imply that the well-ordered mesopores in cubic *Pm3n* arrangement can be retained with the Al/Si molar ratio up to 5% in the synthesis solution. It is also noticed that no separated zeolite phase was formed since no diffraction peaks corresponding to ZMS-5 structure were detected in the high angle regions (as shown in the inserted figures). On the other hand, the counter samples synthesized using sodium silicate instead of zeolite seeds as the silica source lose the resolvable diffraction peaks at 2θ~1.5–2.5° when the Al/Si molar percentages are only higher than 3%.

Fig. 3-5 XRD patterns of calcined (A) Al-SBA-1-alk, (B) Al-ZSBA-1 with various Al/Si molar ratios: (a) 1% (b) 3% (c) 5% (d) 7%.

The textural properties of the calcined Al-SBA-1-alk and Al-ZSBA-1 samples were examined by N_2 physisorption experiments, and the results are shown in Fig. 2 and Table 1. All the calcined samples have type IV isotherms according to the IUPAC classification, and that was the characteristics of ordered mesoporous materials. They are basically in the shape similar to that of conventional SBA-1 prepared in acidic condition. The surface areas and pore volumes of Al-SBA-1-alk are 900−1100 m^2/g and 0.75−0.82 cm^3/g, respectively. In comparison, the surface areas of Al-ZSBA-1 samples assembled from zeolite seeds are lower (600−800 m^2/g). It is also noticeable that Al-ZSBA-1 samples contain small amounts of micropore volumes while Al-SBA-1-alk samples do not.
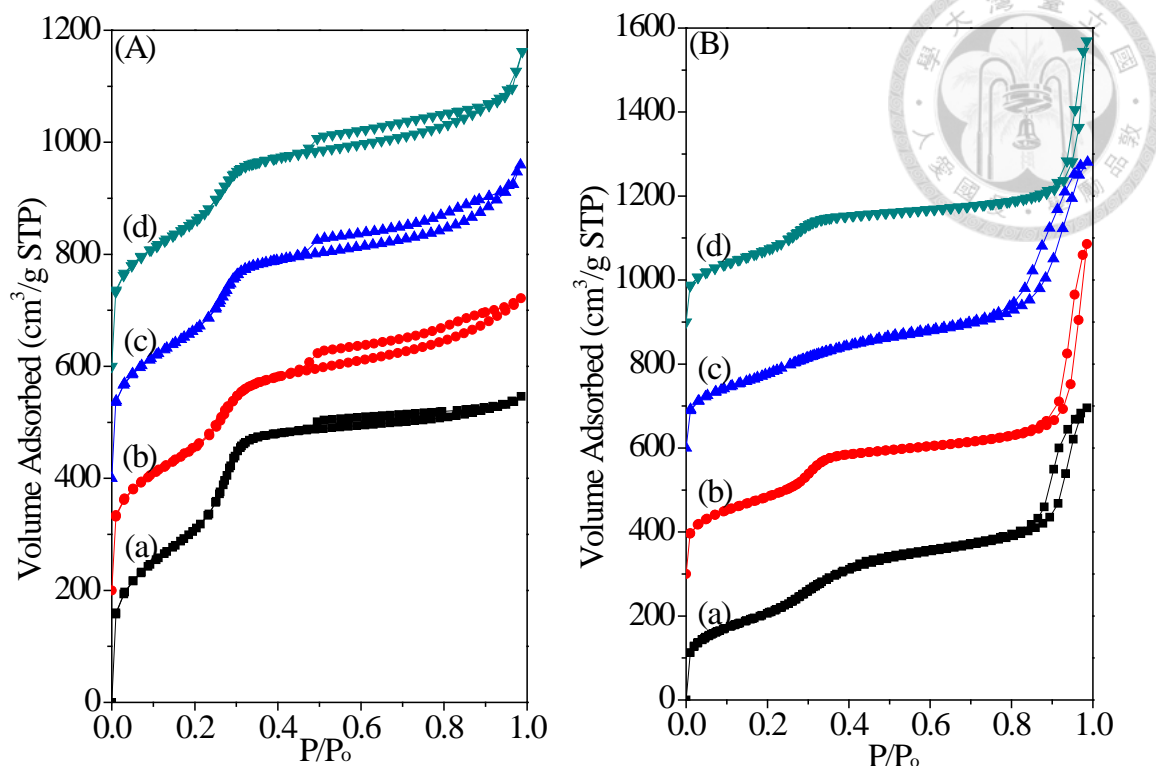
Fig. 3-6 N$_2$ adsorption-desorption isotherms of Al-SBA-1-alk and Al-ZSBA-1 samples with various Al/Si molar ratios: (a) 1% (b) 3% (c) 5% (d) 7%. (shifted in vertical axis by 200 cm^3/g STP between profiles of Al-SBA-1-alk samples and 250 cm^3/g STP of Al-ZSBA-1 samples)

Table 3-1 Physicochemical properties of calcined cubic *Pm*3*n* mesoporous silica samples prepared with various amounts of Al at alkaline condition.

Sample	d$_{210}$ (nm)	S$_{BET}$ (m^2/g)	D$_p$[a] (nm)	V$_{total}$ (cm^3/g)	V$_{micro}$[b] (cm^3/g)	FWHM[c] (ppm)
1Al-SBA-1-alk	3.6	1148	2.2	0.82	0	17.5
3Al-SBA-1-alk	3.8	945	2.2	0.77	0	18.1
5Al-SBA-1-alk	4.0	982	2.2	0.79	0	17.6
7Al-SBA-1-alk	4.1	961	2.2	0.75	0	16.6
1Al-ZSBA-1	4.1	759	2.4	0.86	0.03	15.7
3Al-ZSBA-1	3.8	677	2.4	0.70	0.02	15.4
5Al-ZSBA-1	3.8	652	2.4	0.66	0.05	15.8
7Al-ZSBA-1	3.9	645	2.4	0.60	0.07	15.2

[a]Calculated from desorption branch; [b]Calculated from t-plot method; [c]Solid-state ^{27}Al MAS NMR peak at 50 ppm

SEM images show that both Al-ZSBA-1 and Al-SBA-1-alk materials were generally spherical without any facets (Fig. 3-7). The particle sizes of the materials synthesized in alkaline condition varies in a large range from 100 nm to 1 μm in diameter. They are different from the particles of SBA-1 synthesized by acidic route, which have well-defined external morphology with crystal facets, and the particle size was usually in 3–15 μm.[36,39] The smaller particle sizes of the materials synthesized in alkaline condition are due to the faster precipitation rate of the silica.[54] It is also noticeable that the particle sizes decrease with the increase in Al content. Moreover, the particle sizes of Al-ZSBA-1 assembled from zeolite seeds are less homogeneous than Al-SBA-1-alk. The TEM photographs shown in Fig. 3-8 confirm that the Al-SBA-1-alk and Al-ZSBA-1materials possessed long-range ordering of the 3D cubic arrays. The average pore diameter determined from TEM photographs is around 2 nm, which is in consistence with that from N_2 sorption experiments.
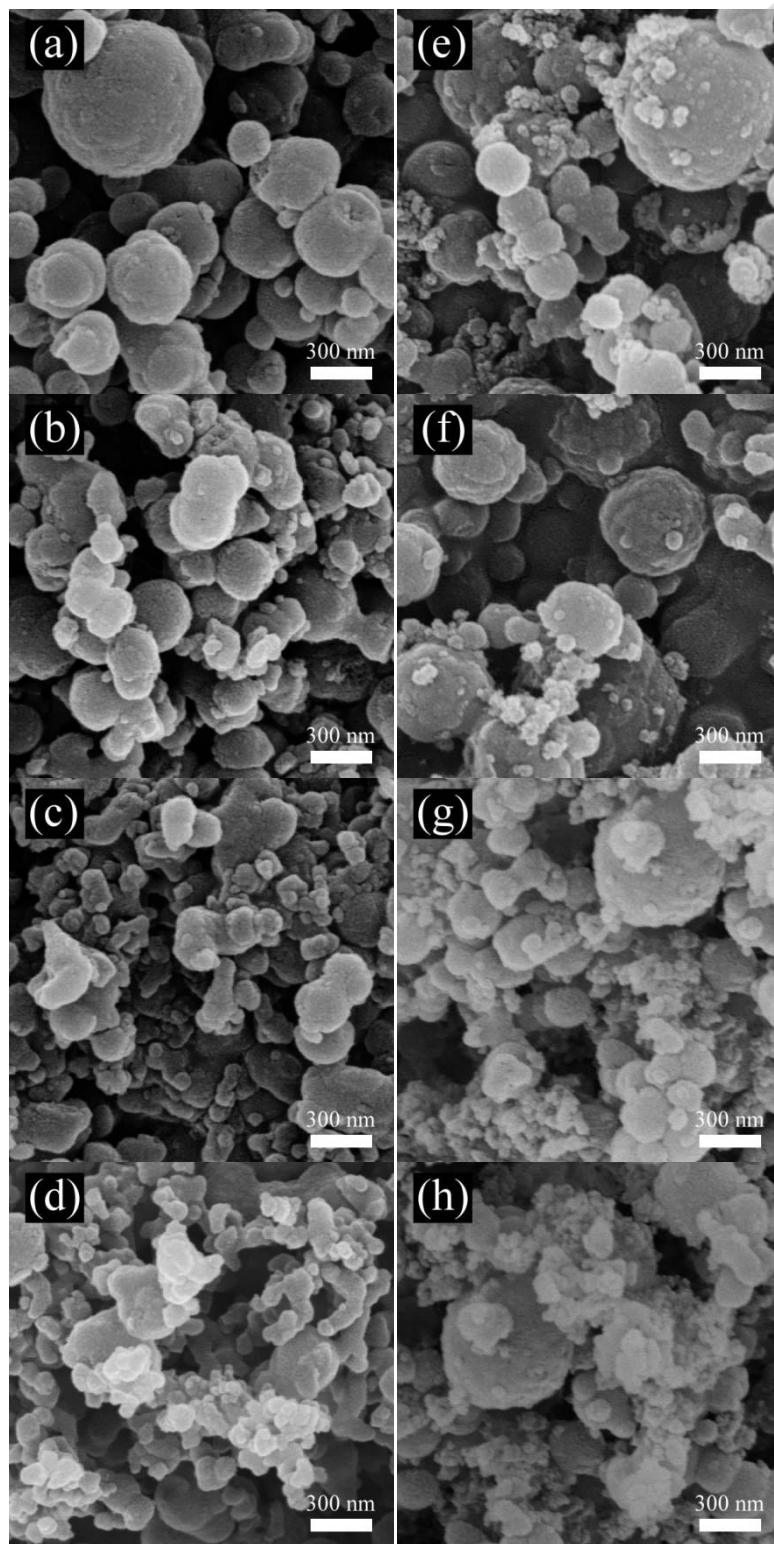
Fig. 3-7 SEM photographs of Al-SBA-1-alk (a-d) and Al-ZSBA-1 (e-h) samples with various Al/Si molar ratios: (a) 1% (b) 3% (c) 5% (d) 7% (e) 1% (f) 3% (g) 5% (h) 7%.
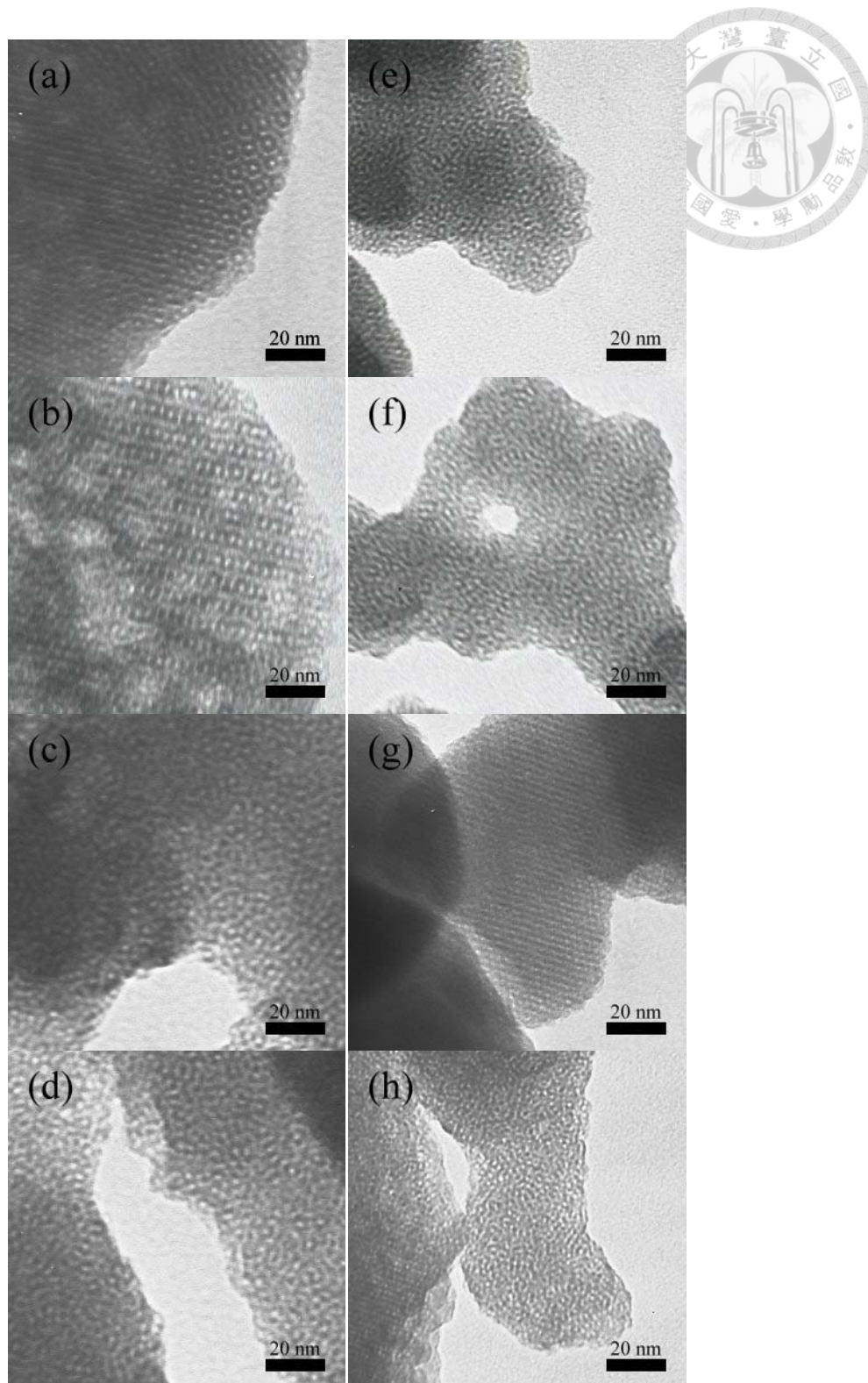
Fig. 3-8 TEM photographs of Al-SBA-1-alk (a-d) and Al-ZSBA-1 (e-h) samples with various Al/Si molar ratios: (a) 1% (b) 3% (c) 5% (d) 7% (e) 1% (f) 3% (g) 5% (h) 7%.
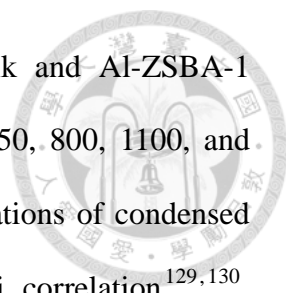
Fig. 3-9 shows the FT-IR spectra of calcined Al-SBA-1-alk and Al-ZSBA-1 samples in comparison to that of ZSM-5. The absorptions near 450, 800, 1100, and 1220 cm^{-1} are assigned to the Si-O-Si bending and stretching vibrations of condensed silica framework. According to the Flanigen-Khatami-Szymanski correlation[129,130], these peaks are corresponding to internal vibration of Si(A1)O$_4$ tetrahedra and are common to silica and quartz. For the cubic *Pm*3*n* silica materials, these peaks are relatively broader in comparison to those of ZSM-5 due to the amorphous nature of the silica framework. In addition, a bending vibration of non-condensed silanol group appears at ca. 960 cm^{-1} and the bending and stretching vibrations of hydroxyl groups and physically adsorbed water appear at 1650 and 3450 cm^{-1}, respectively. It is noticeable that the walls of both Al-SBA-1-alk and Al-ZSBA-1 materials contain large amounts of silanol groups, akin to amorphous silica. The absorption at 550-650 cm^{-1}, on the other hand, was assigned to the presence of a double-ring of tetrahedra in the zeolitic framework[131,132]. For a ZSM-5 structure, the latter absorption appears near 550 cm^{-1}. The intensity ratio of the peaks at 550 to 450 cm^{-1} is often used as a quantitative measurement of zeolite crystallinity. The ratio for the ZSM-5 sample is 0.77, and the Al-ZSBA-1 materials assembled from zeolite seeds have the ratios of 0.61–0.63, which are only slightly higher than 0.58 for 2Al-SBA-1-alk. These results imply that the zeolite seeds incorporated in the walls of Al-ZSBA-1 materials have low crystallinity.
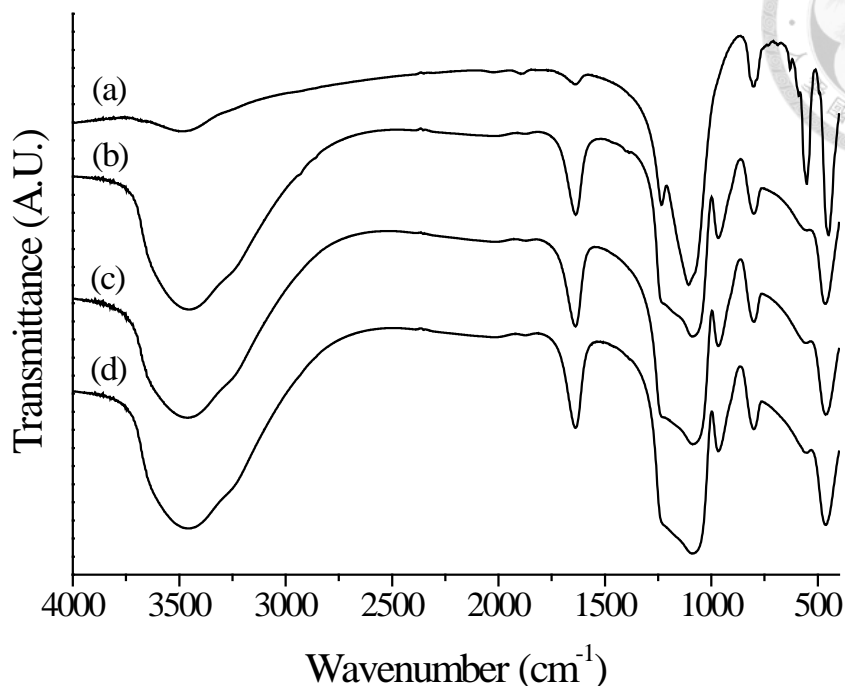
Fig. 3-9 FT-IR spectra of (a) ZSM-5, (b) 2Al-SBA-1-alk, (c) 2Al-ZSBA-1 and (d) 5Al-ZSBA-1.

Fig. 3-10 shows the solid state ^{27}Al MAS NMR spectra of the calcined samples containing various amounts of Al(III). All the Al-ZSBA-1 samples show only a single peak at 50 ppm assigned to the tetrahedrally coordinated aluminum. Moreover, the peak intensity increases with the aluminum content. The absence of signals around 0 ppm, corresponding to the octahedrally coordinated aluminum, indicates that no extra-framework alumina species were formed. However, the Al-SBA-1-alk sample with higher Al loading has an additional small peak appeared at 0 ppm on the ^{27}Al MAS NMR spectra and the peaks should correspond to Al(III) ions in octahedral coordination, which could be due to the formation of extra-framework alumina species in the 7Al-SBA-1-alk sample. These results imply that the Al(III) ions are better retained in the tetrahedral sites of the mesoporous silica framework if they are incorporated into the

69

zeolite seeds first. In addition, the value of full width at half maximum (FWHM) for Al tetrahedral peaks provides a measurement of the uniformity of Al microenvironment in both zeolites and amorphous silicas.[69,133] For the Al-ZSBA-1 samples, the FWHM values are all about 15 ppm smaller than that of Al-SBA-alk samples (Table 3-1). This result clearly evidences that using zeolite seeds as silica source slightly increases the uniformity of Al environment in the Al-ZSBA-1 samples.
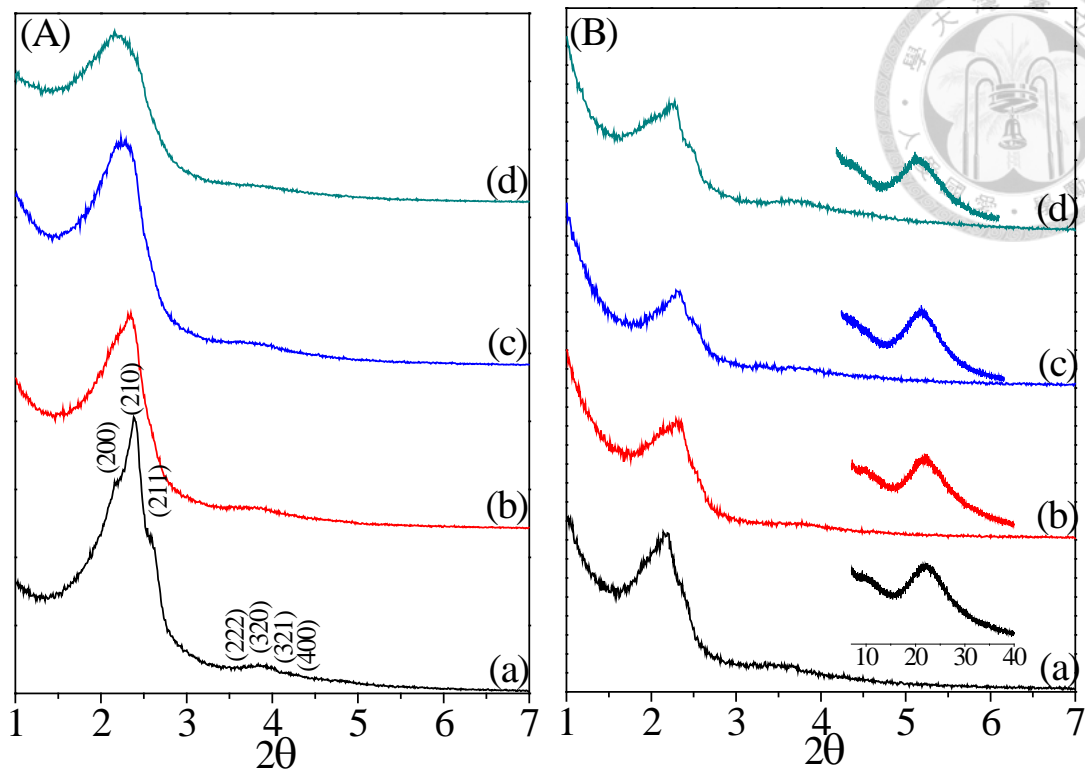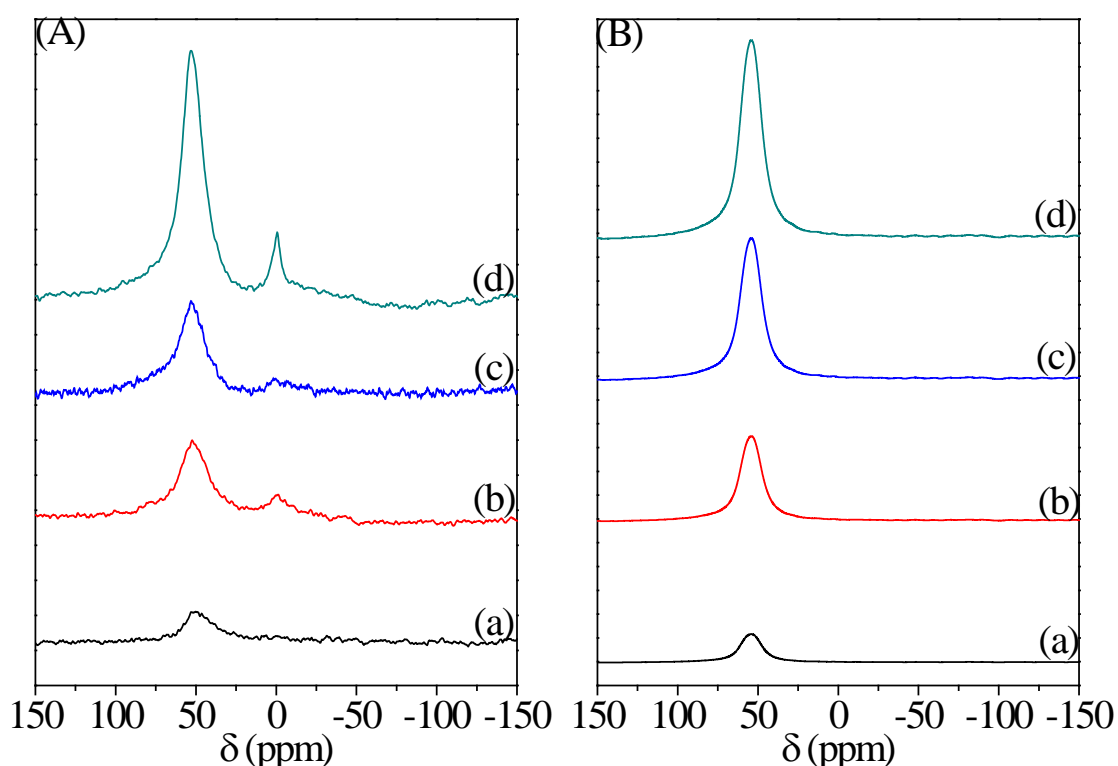

Fig. 3-10 Solid state ^{27}Al MAS NMR spectra of calcined (A) Al-SBA-1-alk, (B) Al-ZSBA-1 with various Al/Si molar ratios: (a) 1% (b) 3% (c) 5% (d) 7%.

The acidities of the calcined Al-ZSBA-1 materials assembled from zeolite seeds were examined by carrying out the NH$_3$-TPD experiment and the profiles were compared with those of Al-SBA-1-alk and ZSM-5 (Fig. 3-11). Commercial ZSM-5 owns the largest acid strength among the studied materials. Two strong and broad

signals are seen with the maximum at 484 K and 706 K, indicating that there are two acid sites in ZSM-5. In contrast, the Al-ZSBA-1 materials have only one signal covering 373–573 K with the maximum at 450 K. All the Al-SBA-1-alk materials have similar NH_3-TPD profiles as that of Al-ZSBA-1. However, the Al-ZSBA-1 materials have one shoulder peak at 573 K, indicating that the Al-ZSBA-1 materials assembled from zeolite seeds have slightly stronger acidic strength as that of Al-SBA-1-alk.
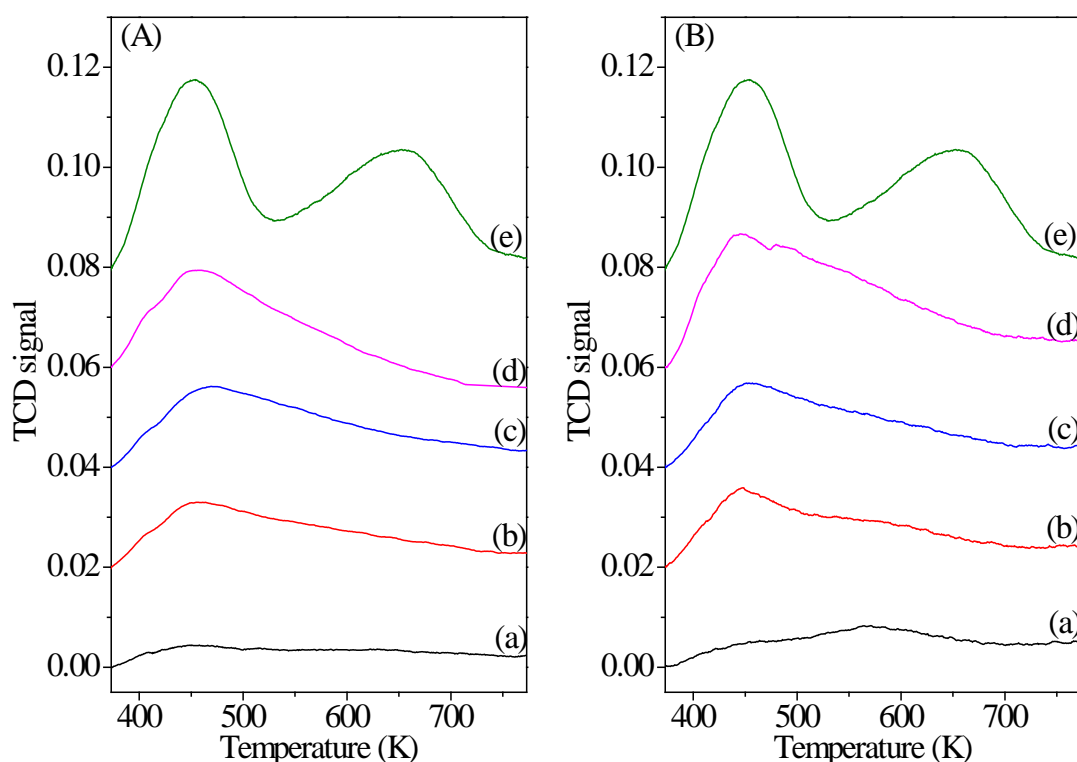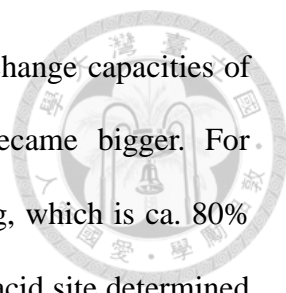
Fig. 3-11 NH_3-TPD profiles of Al-SBA-1-alk and Al-ZSBA-1 calcined (A) Al-SBA-1-alk, (B) Al-ZSBA-1 with various Al/Si molar ratios: (a) 1% (b) 3% (c) 5% (d) 7% (e) ZSM-5.

The accessibility of acidic sites in the Al-containing porous samples was studied by ion-exchange of the protons on the Brønsted acidic sites with cations of different sizes and the exchange capacities were determined by titrating the filtrate with NaOH

aqueous solution[134][135]. The results are shown in Table 3-2. The exchange capacities of all samples decreased when the size of ion-exchange agent became bigger. For 5Al-ZSM-5 sample, the exchange capacity with Na^+ is 0.67 mmol/g, which is ca. 80% of Al content. This ratio is almost the same as the ratio of Brønsted acid site determined by IR spectra of adsorbed pyridine versus tetrahedral Al content determined by NMR reported by Datka et al.[136] The exchange capacity with TMA^+ is slightly lower (0.62 mmol/g) and that with TBA^+ decreases abruptly to 0.11 mmol/g. The ratio of TBA^+/Na^+ exchange capacities is 16%. These results indicate that the micropore diameter of ZSM-5 is too small to accommodate TBA^+ ions. On the other hand, both mesoporous SBA-1 samples have Na^+ exchange capacities around 0.5 mmol/g, which is ca. 55% and 62% of Al contents in 5Al-SBA-1-alk and 5Al-ZSBA-1, respectively. It is reported that the ratios of Brønsted/Lewis acidic sites on Al-SBA-15 which has 2D hexagonal structure are ca. 0.5 and much lower than those of zeolites.[137] Our results show that Al-SBA-1 has higher ratios of Brønsted/Lewis acidic sites than Al-SBA-15, but lower than ZSM-5.

For 5Al-SBA-1-alk assembled from sodium silicate, the exchange capacities only decreases slightly when the size of exchange agent increases from Na^+ to bulky TBA^+. In comparison, more significant decrease is seen on 5Al-ZSBA-1 assembled from zeolite seeds. The ratios of TBA^+/Na^+ exchange capacities are 92% and 82% for 5Al-SBA-1-alk and 5Al-ZSBA-1, respectively. These results confirmed that most of the Brønsted acidic sites on mesoporous SBA-1 materials are accessible by bulky TBA^+ ions. However, the 5Al-ZSBA-1 sample assembled from zeolite seeds has ca. 10% of the acidic sites probably buried inside the micropores and not accessible by bulky TBA^+ ions.

From above characterizations on Al-ZSBA-1 samples, we proposed that the wall of Al-ZSBA-1 samples is partially crystalline. The wall mainly composes of silicate in amorphous structure but is also incorporated with building units of MFI structure.
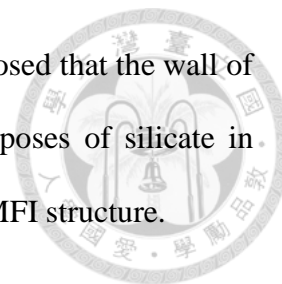
Table 3-2. Al contents and cation-exchange capacities of various samples

Sample	Al content (mmol/g_{cat})[a]	Exchange capacity (mmol/g_{cat})			Ratio of accessibility[b]
		Na+	TMA+	TBA+	
5Al-ZSM-5	0.84	0.67	0.62	0.11	16%
5Al-SBA-1-alk	0.92	0.51	0.50	0.47	92%
5Al-ZSBA-1	0.80	0.50	0.48	0.41	82%

[a]Measured by ICP-MS; [b]Calculated from the ratio of exchange capacities (TBA$^+$/Na$^+$)

3.2 Catalytic alkylation of 2,4-di-*tert*-butylphenol by cinnamyl alcohol

The Friedel-Crafts alkylation of DTBP with cinnamyl alcohol and the subsequent isomerization of 2,4-di-*tert*-butyl-6-cinnamylphenol (DTBCP) to yield flavan (Scheme 3-1) in the liquid phase was chosen as a model reaction to evaluate the catalytic activities of Al-containing cubic *Pm*3*n* mesoporous silica. All the possible reactions are depicted in Scheme 3-2. There are two side reactions which are polymerization of cinnamyl alcohol and disproportionation of DTBP.

Table 3 compares several solvents commonly used in the literature. Among them, isooctane and dimethylacetamide (DMAc) could reach a reaction temperature of 368 K, while acetonitrile (ACN) could only reach 355 K due to its relatively lower boiling point. Highest DTBP conversion and flavan yield were observed in isooctane. In contrast, no catalytic activity was seen using DMAc of a high dielectric constant of 37.8 as the solvent. It is attributed to that DMAc of high polarity and also as a weak base (pKa of its conjugate acid around -0.5) will hinder the reaction by adsorbing strongly on the catalytic active sites. On the other hand, acetonitrile gave a lower DTBP conversion and DTBCP yield than isooctane, but no flavan was formed. It is attributed to that the isomerization of DTBCP to flavan is an endothermic reaction and unfavorable at low reaction temperature. Consequently, isooctane is the most suitable solvent among the studied solvents, and it is used hereafter.
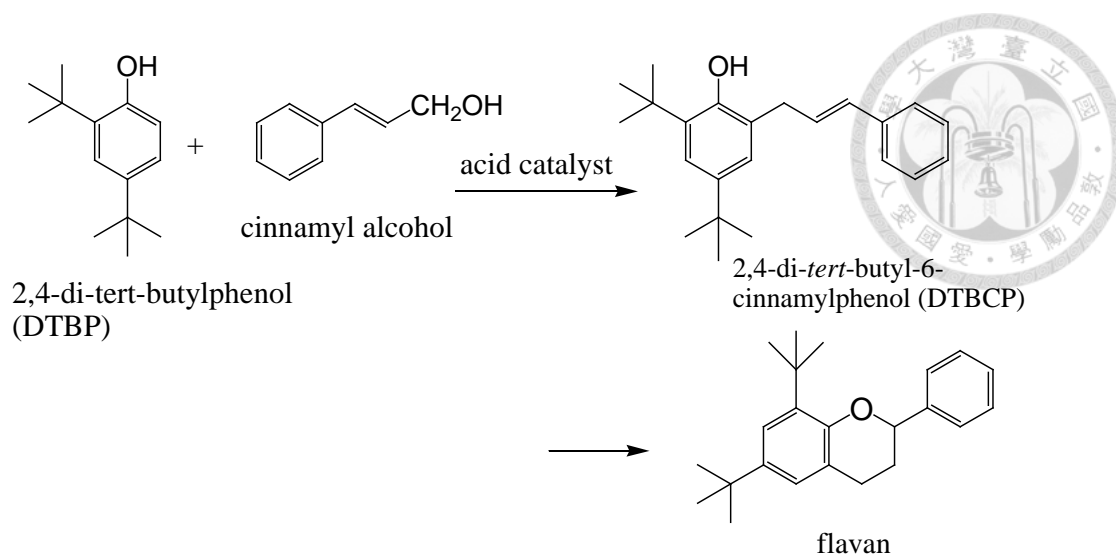
Scheme 3-1 Reaction paths of alkylation of 2,4-di-*tert*-butylphenol with cinnamyl alcohol to form flavan.
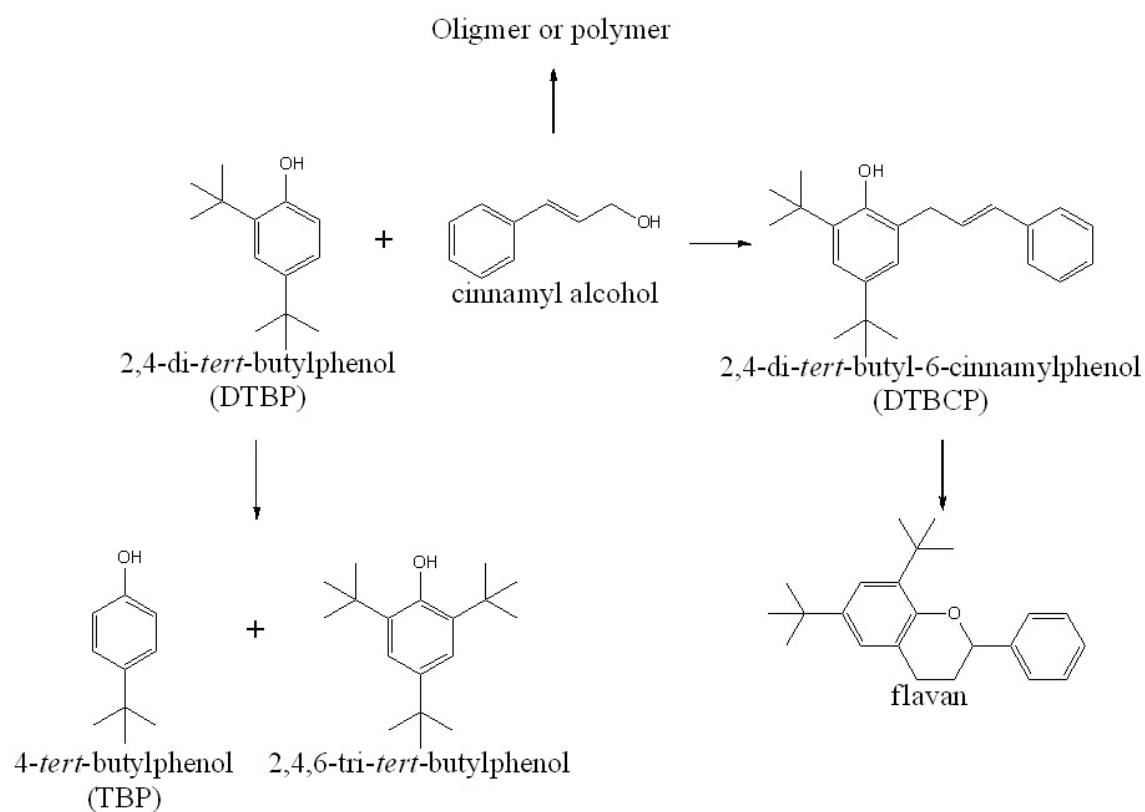
Scheme 3-2 The other possible reactions pathway of alkylation of 2,4-di-*tert*-butylphenol with cinnamyl alcohol.

Table 3-3 Alkylation of 2,4-di-*tert*-butylphenol with cinnamyl alcohol with different solvents

Solvent	Dielectric constant	DTBP conv.(%)	Selectivity (%)	Flavan yield (%)	DTBCP yield (%)	TBP yield (%)
isooctane	1.94	53	60	32	5	6
ACN [a]	37.5	20	0	0	18	0
DMAc	37.8	<1	0	0	0	0

Reaction condition: 0.25 mmol DTBP, 0.25 mmol cinnamyl alcohol, 125 mg catalyst (5Al-SBA-1-alk), 12.5 mL solvent, 5 h.

Fig. 3-12 and Table 3-4 show the DTBP conversion and product yields over 5Al-SBA-1-alk catalyst as a function of reaction period. In the initial reaction period of 10 min., two different reactions proceed simultaneously. One is Friedel-Crafts alkylation of DTBP with cinnamyl alcohol, and the other is polymerization of cinnamyl alcohol to form oligomers or polymers[138]. The cinnamyl alcohol was found to be completely consumed in 10 min., while the DTBP conversion is only 35% at this stage. This result indicates that the polymerization of cinnamyl alcohol is much fast than Friedel-Crafts alkylation.

Fig. 3-12 shows that after the consumption of cinnamyl alcohol, the DTBP conversion still increases steadily with reaction time. It is due to the proceeding of transalkylation between DTBP molecules. As a result, 4-*tert*-butylphenol (TBP) and 2,4,6-tri-*tert*-butylphenol (TTBP) are formed as the side products. The main product in the liquid phase at 10 min. is DTBCP formed through Friedel-Crafts alkylation of DTBP with cinnamyl alcohol. The yield of DTBCP decreases while that of flavan increases with reaction time due to the isomerization of DTBCP to form flavan through Michael reaction. All the DTBCP are converted to flavan, and the flavan yield reaches maximum after 5 h of reaction. All the reaction pathways are illustrated in Scheme 3-3.
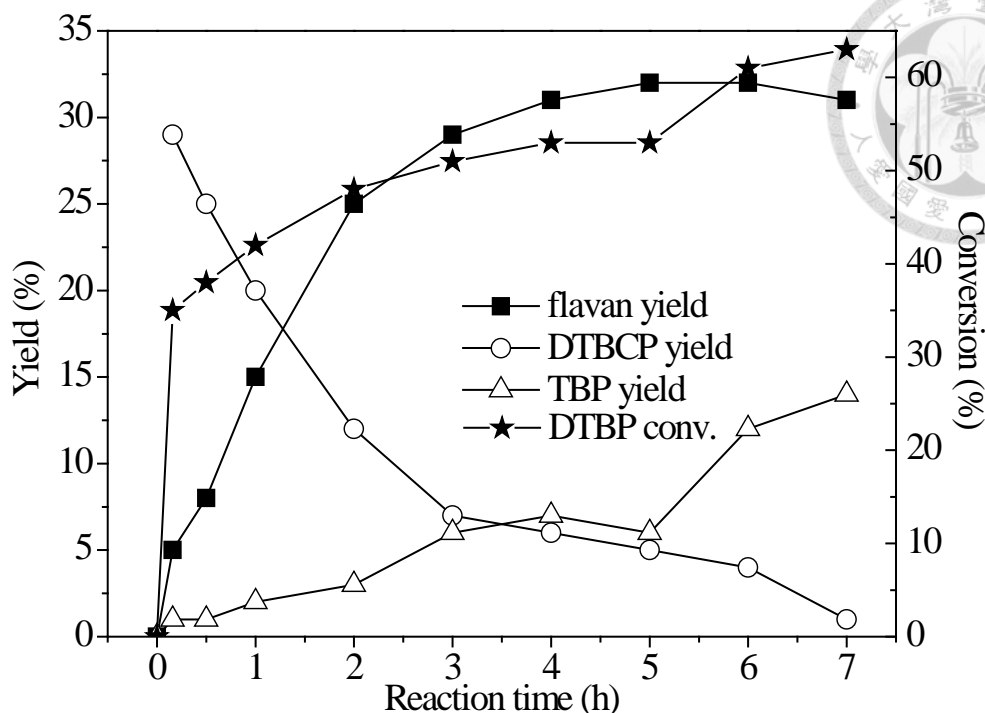
Fig. 3-12 The DTBP conversion and the product yield as a function of reaction time over 5Al-SBA-1-alk. (■: flavan yield, ○: DTBCP yield, △: TBP yield, and ★: DTBP conversion)

Table 3-4 Alkylation of DTBP with cinnamyl alcohol with different periods

Reaction period (h)	DTBP conv. (%)	Flavan Select. (%)[a]	Flavan yield (%)	DTBCP yield (%)	TBP yield (%)
0.16	35	15	5	29	<1
0.5	38	21	8	25	1
1	42	35	15	20	2
2	48	52	25	12	3
3	51	57	29	7	6
4	53	58	31	6	7
5	53	60	32	5	6
6	61	52	32	4	12
7	63	49	31	<1	14

Reaction condition: 0.25 mmol DTBP, 0.25 mmol cinnamyl alcohol, 125 mg 5Al-SBA-1-alk catalyst, 12.5 mL isooctane, 368K; [a]selectivity = flavan yield/ DTBP conversion.
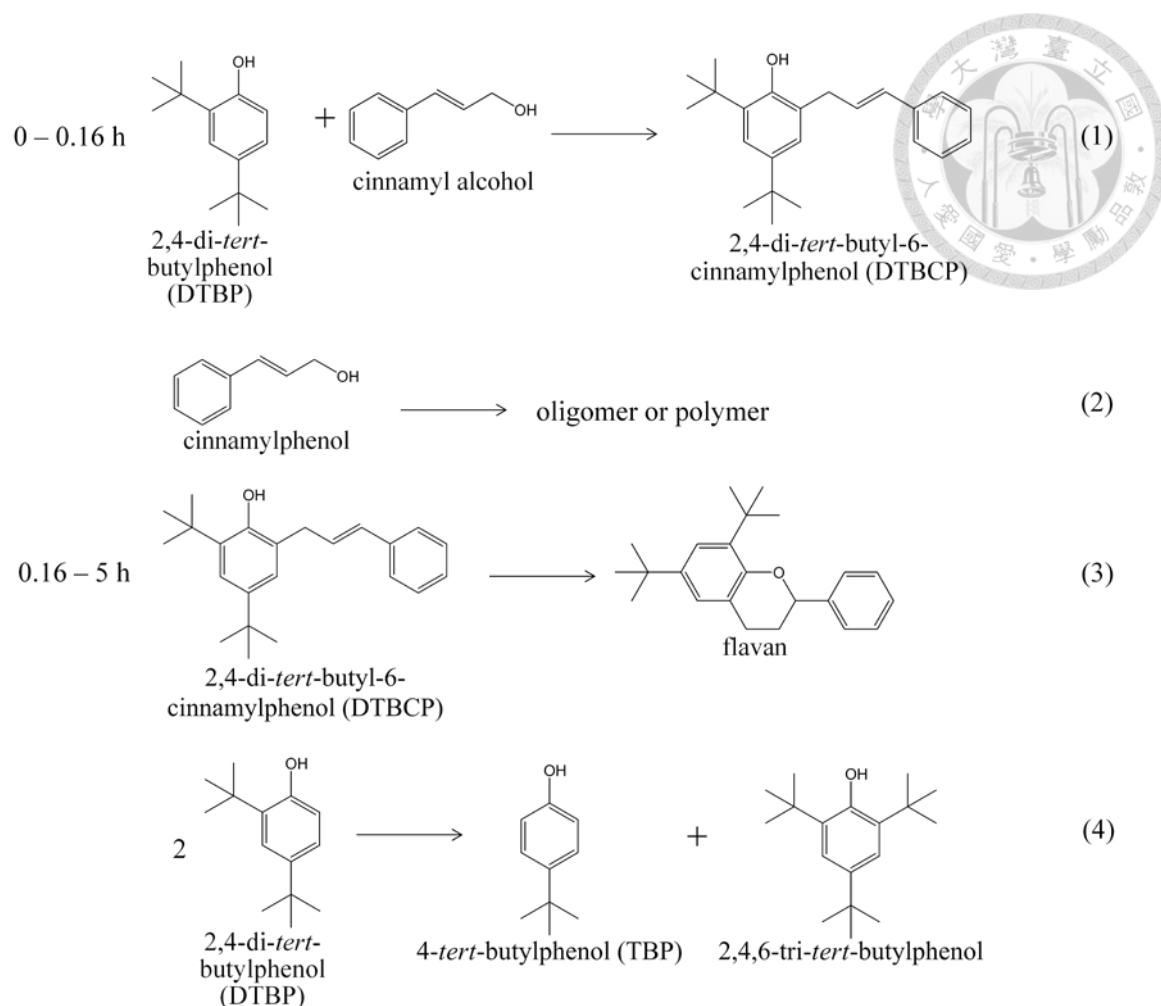
Scheme 3-3. Reaction pathway in different periods.

The catalytic performance of 5Al-ZSBA-1 catalyst in alkylation reaction of DTBP as a function of reaction period is examined in Fig. 3-13. The flavan yield will reach maximum after reaction time of 6 h. The DTBP conversion increases dramatically after reaction time of 5 h. These performances of 5Al-ZSBA-1 are similar to those of 5Al-SBA-1-alk except that 5Al-ZSBA-1 catalyst has higher initial rate for DTBP conversion and flavan yield due to its stronger acidity.
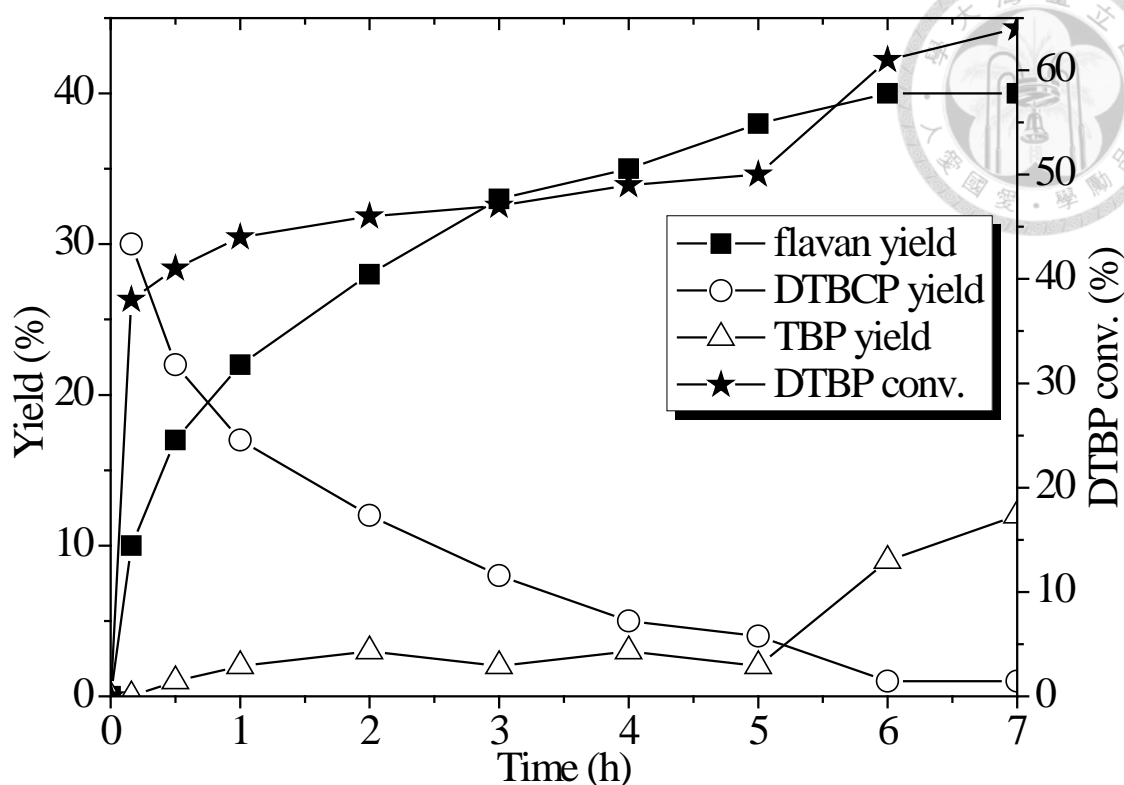
Fig. 3-13 The DTBP conversion and the product yield as a function of reaction time over 5Al-ZSBA-1. (■: flavan yield, ○: DTBCP yield, △: TBP yield, and ★: DTBP conversion)

The effect of reaction temperature on the catalytic results over 5Al-SBA-1 is shown in Table 3-5. The DTBP conversion increases with reaction temperature. However, no flavan product is formed at low reaction temperature of 333 K, and the flavan selectivity reaches 60% at 368 K. It is attributed to that the isomerization of DTBCP to flavan is an endothermic reaction. It is also noticeable that the total yields of flavan and DTBCP do not change significantly with the reaction temperature, and the total yields maintain around 37%. The increased conversion of DTBP at higher temperatures is thus contributed by transalkylation reaction between DTBP molecules. It is to say that transalkylation reaction is also an endothermic reaction.

In order to minimize the consumption of cinnamyl alcohol in polymerization reaction, the amount of cinnamyl alcohol in reactants was decreased. Table 3-6 shows that DTBP conversion indeed increases with increasing the molar ratio of DTBP/cinnamyl alcohol. However, the flavan yield reaches the maximum when the molar ratio of DTBP/cinnamyl alcohol is 1. Therefore, an equimolar mixture of DTBP and cinnamyl alcohol is the optimal ratio of the reactants for this reaction.

Table 3-5. Alkylation of 2,4-di-*tert*-butylphenol with cinnamyl alcohol with different reaction temperature

Reaction Temp. (K)	DTBP conv.(%)	Selectivity (%)	Flavan yield (%)	DTBCP yield (%)	TBP yield (%)
333	34	0	0	35	0
353	43	24	10	29	0
368	53	60	32	5	6

Reaction condition: 0.25 mmol DTBP, 0.25 mmol cinnamyl alcohol, 125 mg catalyst (5Al-SBA-1-alk), 12.5 mL isooctane, 5 h.
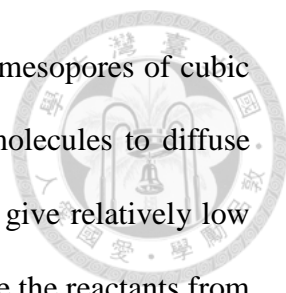
Table 3-6 Alkylation of 2,4-di-*tert*-butylphenol with cinnamyl alcohol with different DTBP/cinnamyl alcohol ratios

DTBP/cinnamyl alcohol	DTBP conv.(%)	Selectivity (%)	Flavan Yield (%)	DTBCP yield (%)	TBP yield (%)
0.5	39	13	5	35	0
1	53	60	32	5	6
2	61	51	31	0	13

Reaction condition: 0.25 mmol DTBP, 0.125-0.5 mmol cinnamyl alcohol, 125 mg catalyst (5Al-SBA-1-alk), 12.5 mL isooctane, 368 K, 5 h.

Table 3-7 compares the Al contents and catalytic activities of Al-ZSBA-1 and Al-SBA-1-alk materials with those of ZSM-5 and Beta zeolites. Elemental analyses by ICP-MS show that the amounts of Al(III) ions incorporated in either Al-ZSBA-1 assembled from zeolite seeds or Al-SBA-1-alk prepared using sodium silicate as the silica source were close to those in the synthesis solutions up to Al/Si atomic ratio of 5%. Nevertheless, the Al contents in Al-SBA-1-alk materials are slightly higher than those of Al-ZSBA-1, except those of lowest Al contents, saying samples 1Al-ZSBA-1 and 1Al-SBA-1-alk.

The DTBP conversions over all the Al-SBA-1-alk materials are higher than those over Al-ZSBA-1. Since even 1Al-SBA-1-alk, which has lower Al content than 1Al-ZSBA-1, has higher DTBP conversion than 1Al-ZSBA-1, it is probably because of the relatively higher surface areas of Al-SBA-1-alk materials. However, the flavan selectivities over Al-ZSBA-1 materials are higher than those over Al-SBA-1-alk. These results demonstrate that the Al-ZSBA-1 materials assembled with zeolite seeds can catalyze the Michael reaction more efficiently than mesoporous materials of amorphous walls. Moreover, the flavan selectivities over Al-ZSBA-1 materials are similar to that over ZSM-5, except 1Al-ZSBA-1 which has lowest acidity. This is an indication that Al-ZSBA-1 materials own strong acidities from the zeolite seeds incorporated on the pore walls. On the other hand, the TOF was calculated as yield of flavan molecule per Al atom per hour and it is average TOF because the time was 5 hours. The TOF decreases with the increase in Al loading for both Al-SBA-1-alk and Al-ZSBA-1 materials, indicating that a portion of aluminum may be buried inside the silica framework and not accessible by the reactants. Nevertheless, higher TOFs are obtained over the mesoporous Al-SBA-1-alk and Al-ZSBA-1 catalysts in comparison to those of

microporous zeolites of similar Al contents, inferring that the large mesopores of cubic *Pm*3*n* silica should facilitate the bulky reactant and intermediate molecules to diffuse and access the acidic sites inside the pores. In contrast, the zeolites give relatively low conversions due to its pore sizes of smaller than 1 nm, which obstacle the reactants from diffusing into the pores and accessing the acidic sites. Among the catalysts studied, 5Al-ZSBA-1 and 7Al-ZSBA-1 catalysts give the highest flavan yield around 38-39%, relatively high DTBP conversion of over 50%, and selectivity around 75% in the alkylation of DTBP with cinnamyl alcohol.

After the catalytic reactions, the 5Al-ZSBA-1 and 5Al-SBA-1-alk catalysts were regenerated by calcination at 823 K for 4 h. The regenerated catalysts were used under the same reaction condition as that of the fresh catalysts, and the results are also listed in Table 7. The catalytic activities are well retained over both regenerated catalysts in the second run. Besides, no aluminum leaching occurred during the catalytic reaction based on Al/Si analysis by ICP-MS technique on the regenerated catalysts.

Because DTBP is a bulky molecule which can't diffuse into the microporous channel, the modified TOFs are listed in Table 3-7 and its meaning is yield of flavan per accessible Al atom per hour. It is defined as followed:

$$\text{Modified TOF} = \text{TOF} \times \left(\text{Al content} \times \frac{\text{exchange capacity of TBA}^+}{\text{exchange capacity of Na}^+} \right)$$

The results show that the value of modified TOF of 5Al-ZSM-5 is higher largely than two other mesoporous materials, 5Al-SBA-1-alk and 5Al-ZSBA-1, indicating that the Al center in zeolites has great catalytic activity on this reaction. It is noticeable that 5Al-ZSBA-1 has higher modified TOF than 5Al-SBA-alk due to its partially crystallite wall.

82

The particle size is an important factor for catalytic activity. The smaller particle size, the shorter diffusion path and the larger external surface area. The higher catalytic activity over 5Al-ZSBA-1 is possibly attributed to its smaller particle sizes. However, the value of ion-exchange capacity with TBA$^+$ ion of 5Al-ZSBA-1 listed in Table 3-2 is similar to that of 5Al-SBA-1-alk, indicating that the external surface areas of these two catalysts are the exactly same. Therefore, the higher catalytic activity over 5Al-ZSBA-1 is attributed to its partially crystallite wall instead of particle size.

Table 3-7 Alkylation of 2,4-di-*tert*-butylphenol with cinnamyl alcohol over Al-SBA-1-alk and Al-ZSBA-1 with different Al-loadings.

Sample	Al/Si[a] (%)	DTBP conv.(%)	Flavan select. (%)	Flavan yield (%)	DTBCP yield (%)	TBP yield (%)	TOF (h^{-1})[b]	Modified TOF (h^{-1})
1Al-ZSBA-1	1.1	30	0	0	29	0	0	-
3Al-ZSBA-1	2.6	45	71	32	5	3	0.30	-
5Al-ZSBA-1	4.8	50	76	38	4	3	0.19	0.27
5Al-ZSBA-1[c]	4.8	48	75	36	5	3	0.18	-
7Al-ZSBA-1	5.7	52	75	39	4	4	0.16	-
1Al-SBA-1-alk	1.0	37	0	0	36	0	0	-
3Al-SBA-1-alk	3.4	47	49	23	14	4	0.16	-
5Al-SBA-1-alk	5.5	53	60	32	5	6	0.14	0.16
5Al-SBA-1-alk[c]	5.4	52	60	31	6	6	0.14	-
7Al-SBA-1-alk	5.9	58	60	35	5	6	0.14	-
5Al-ZSM-5	5.0	28	72	20	2	3	0.10	1.04
Beta[d]	2	25	48	12	14	0	0.14	-

Reaction condition: 0.25 mmol DTBP, 0.25 mmol cinnamyl alcohol, 125 mg catalyst, 12.5 mL isooctane, 368 K, 5 h; [a]Measured by ICP-MS; [b]Based on flavan yield.; [c]Regenerated catalyst for second run; [d]CP814E, Zeolyst International

3.3 Conclusions

Aluminum incorporated cubic mesoporous silica of *Pm3n* phase was successfully synthesized using Al-doped ZSM-5 seeds as the silica source and CTEABr as the template at pH around 9. The XRD patterns showed that well-ordered mesopores were retained with the Al/Si molar ratio up to 5% in the synthesis solution. Elemental analysis by ICP-MS showed that the amounts of Al(III) ions incorporated in the solids were close to those in the synthesis solutions up to Al/Si atomic ratio of 5%. From NH_3-TPD experiments, the acidic strength of Al-ZSBA-1 solids assembled from zeolite seeds were higher than that of Al-SBA-1-alk prepared using sodium silicate as the silica source, but lower than that of ZSM-5. Base on ^{27}Al MAS NMR, a high uniformity of Al in tetrahedral coordination, corresponding to the pore wall with secondary zeolite-building unit was observed in Al-ZSBA-1 samples with Al/Si ratios up to 5% in the synthesis solutions. The higher ratio of Brønsted/Lewis acidic sites of Al-ZSBA-1 than Al-SBA-1-alk was seen by using ion-exchanged method.

The Al-incorporated cubic *Pm3n* mesoporous silica materials were efficient catalysts for the alkylation of DTBP by cinnamyl alcohol to yield flavan. The highest activity was obtained over 5Al-ZSBA-1 and 7Al-ZSBA-1, which gave over 50% conversion and 38-39% flavan yield. In contrast, microporous Beta and ZSM-5 zeolites gave relatively low activities, due to the diffusion limitation of the bulky reactant molecules into the small zeolitic pores. The results demonstrate that Al-ZSBA-1 materials assembled from zeolite seeds combine the advantages of strong acidity from zeolites and good diffusivity from mesoporous molecular sieves.
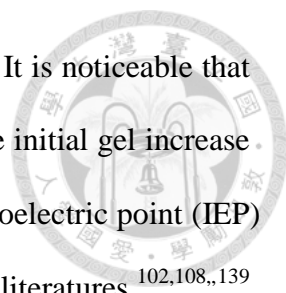
Chapter 4   Direct gas phase epoxidation of propylene over Au/Ti-SBA-1 and Au/Ti-ZSBA-1 materials
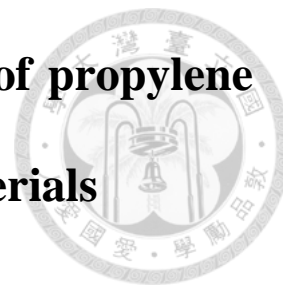
4.1 Characterization

The small angle XRD patterns of the Ti-SBA-1-alk and gold-deposited samples with various Ti/Si molar ratios was shown in Fig. 4-1. The gold-deposited 1Ti-SBA-1-alk series have three distinct diffraction peaks at 2θ~1.5–2.5° indexed to the (200), (210), and (211) planes of cubic $Pm3n$ symmetry. Several weaker diffraction peaks are also observed at 2θ~3–4° assigning to the (222), (320), (321), and (400) planes[19]. However, the three main peaks become unresolved and their intensity decreases when the Ti/Si molar ratios is larger than 3%. Fig. 4-2 show that all the samples have type IV isotherms and H1 hysteresis loops at P/P_o = 0.25－0.35 and the textural properties derived from sorption isotherms are listed in Table 4-1. All these samples possess mesopores size of 2.0-2.3 nm in diameter, high surface area (800-1100 m^2/g) and large pore volume (0.7-0.9 cm^3/g). The surface areas and pore volumes decrease with the increase in Ti loading, indicating the disturbance of self-assembly of CTEABr micelle and silicate by titanium precursors. Besides, the physical properties of gold-deposited Ti-SBA-1-alk is similar to their parents, implying that after gold deposition, the cubic structure is still retained.

The chemical compositions of the calcined materials are tabulated in Table 4-1. The Ti contents and gold loadings in the solid products are determined by ICP–MS technique. The Ti/Si molar ratios in the solids are close to those in the synthesis gels, implying that most Ti(IV) ions are incorporated in the mesoporous materials. The Ti content does not change before and after gold deposition, suggesting that during gold

85

deposition process, no Ti leaching occurs in the acidic environment. It is noticeable that the gold loadings of samples with the same gold concentration in the initial gel increase with Ti/Si molar ratios. This phenomenon can be explained by the isoelectric point (IEP) of the support and similar phenomena have been reported in several literatures.[102,108,,139]

Due to the IEP value of the silica support is about 2-3[140], higher pH environment results in negative charges on the support surface, which repulse the $Au[(OH)_3Cl]^-$ or $Au(OH)_4^-$ anions from the surface of the support, hindering their adsorption on the supports. When Ti is incorporated in the silica support, more gold anions is captured, attributing that the IEP of TiO_2 is about 4-5[140] and less negative charge produce on the surface. The IEP values of pure silica SBA-1 and 5Ti-SBA-1-alk are measured by zeta potential and the data are shown in Fig. 4-3. The IEP value of   5Ti-SBA-1-alk is higher than that of SBA-1. This result is contributed to a stronger interaction between 5Ti-SBA-1-alk and gold anions and hence a higher Au loading efficiency. In addition, the ICP-MS datas in Table 4-1 show that little Na+ ion is remain on the fresh catalysts.
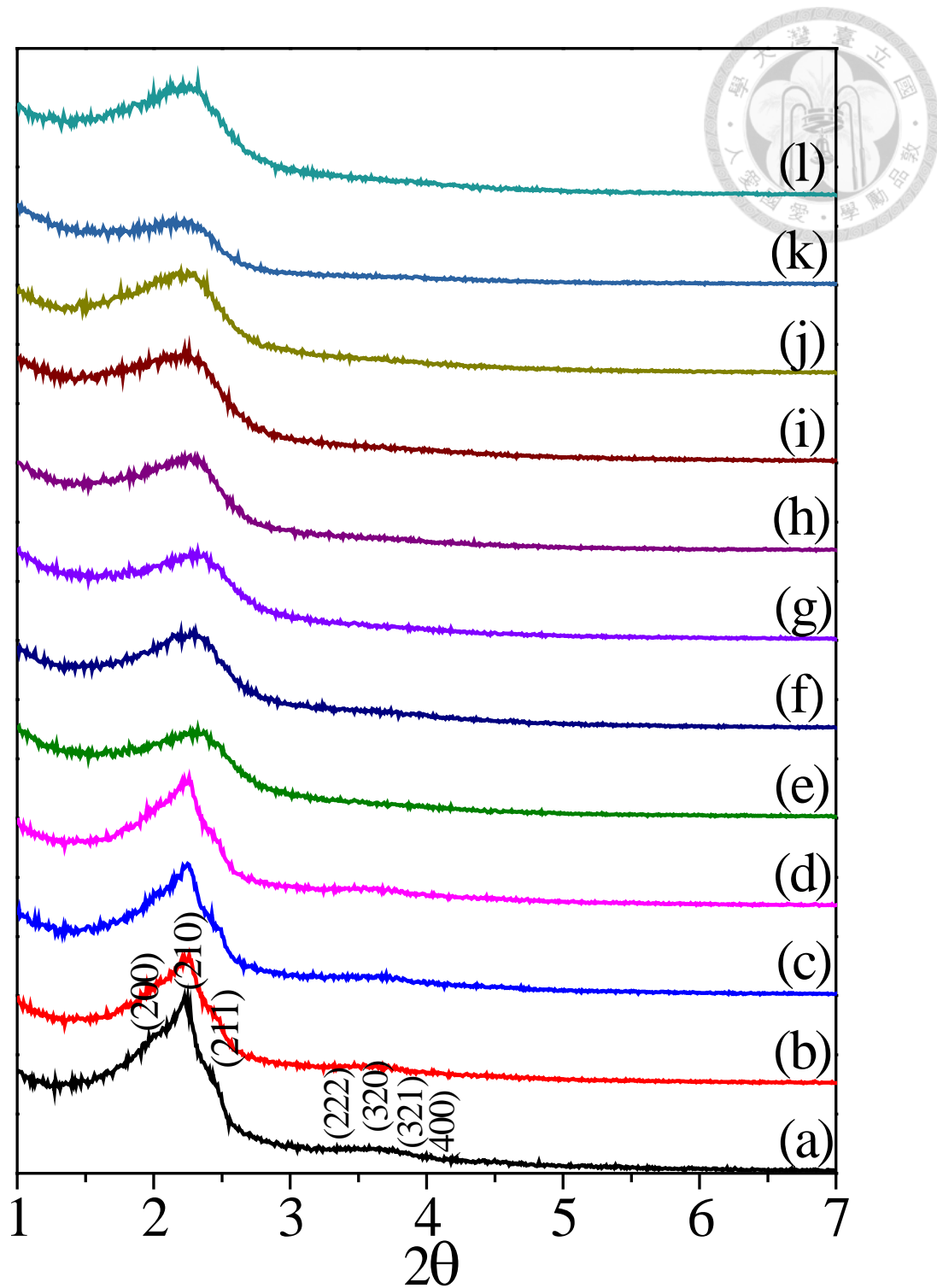
Fig. 4-1 XRD patterns of various samples: (a) 1Ti-SBA-1-alk (b) $5Au^{3+}/1Ti$ (c) $10Au^{3+}/1Ti$ (d) $20Au^{3+}/3Ti$ (e) 3Ti-SBA-1-alk (f) $5Au^{3+}/3Ti$ (g) $10Au^{3+}/3Ti$ (h) $20Au^{3+}/1Ti$ (i) 5Ti-SBA-1-alk (j) $5Au^{3+}/5Ti$ (k) $10Au^{3+}/5Ti$ (l) $20Au^{3+}/5Ti$
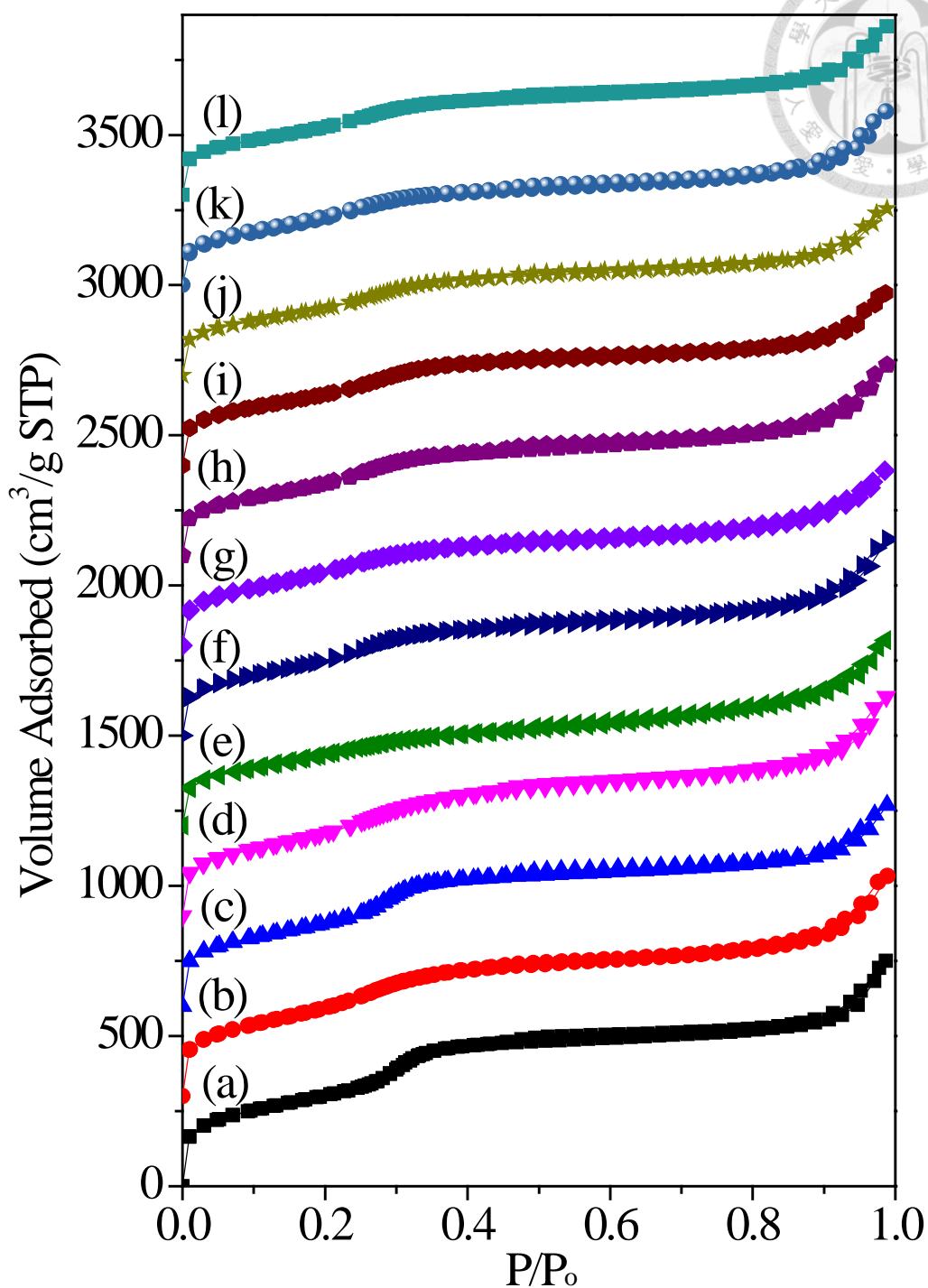
Fig. 4-2 N$_2$ adsorption-desorption isotherms of various samples: (a) 1Ti-SBA-1-alk (b) 5Au^{3+}/1Ti (c) 10Au^{3+}/1Ti (d) 20Au^{3+}/1Ti (e) 3Ti-SBA-1-alk (f) 5Au^{3+}/3Ti (g) 10Au^{3+}/3Ti (h) 20Au^{3+}/3Ti (i) 5Ti-SBA-1-alk (j) 5Au^{3+}/5Ti (k) 10Au^{3+}/5Ti (l) 20Au^{3+}/5Ti (shifted in vertical axis by 200 cm^3/g STP between each samples).

Table 4-1 Physical and chemical properties of various $10Au^{3+}$/Ti samples.

Sample	Ti/Si (mol%)[a]	Au (wt%)[a]	Na (wt%)	d_{210} (nm)	a_o (nm)	S_{BET} (m²/g)	D_p (nm)[b]	V_{total} (cm³/g)[c]
1Ti-SBA-1-alk	1.1	0	-	4.0	8.9	1100	2.3	0.93
$5Au^{3+}$/1Ti	1.0	0.10	n.d.	3.9	8.7	1091	2.2	0.93
$10Au^{3+}$/1Ti	1.1	0.28	n.d.	3.9	8.7	1012	2.3	0.85
$20Au^{3+}$/1Ti	1.1	0.60	<0.1	4.0	8.9	1027	2.2	0.92
3Ti-SBA-1-alk	3.1	0	-	3.8	8.5	885	2.0	0.77
$5Au^{3+}$/3Ti	3.1	0.17	n.d.	3.8	8.5	940	2.1	0.79
$10Au^{3+}$/3Ti	3.0	0.48	n.d.	3.8	8.5	933	2.0	0.76
$20Au^{3+}$/3Ti	3.0	1.26	<0.1	3.9	8.7	893	2.1	0.78
5Ti-SBA-1-alk	5.0	0	-	3.9	8.7	873	2.2	0.73
$5Au^{3+}$/5Ti	5.1	0.26	n.d.	3.9	8.7	828	2.2	0.69
$10Au^{3+}$/5Ti	4.9	0.82	<0.1	3.9	8.7	851	2.1	0.71
$20Au^{3+}$/5Ti	5.0	1.92	<0.1	3.9	8.7	840	2.2	0.69

[a]determined by ICP-MS [b]calculated from desorption branch [c]calculated at $P/P_o = 0.95$
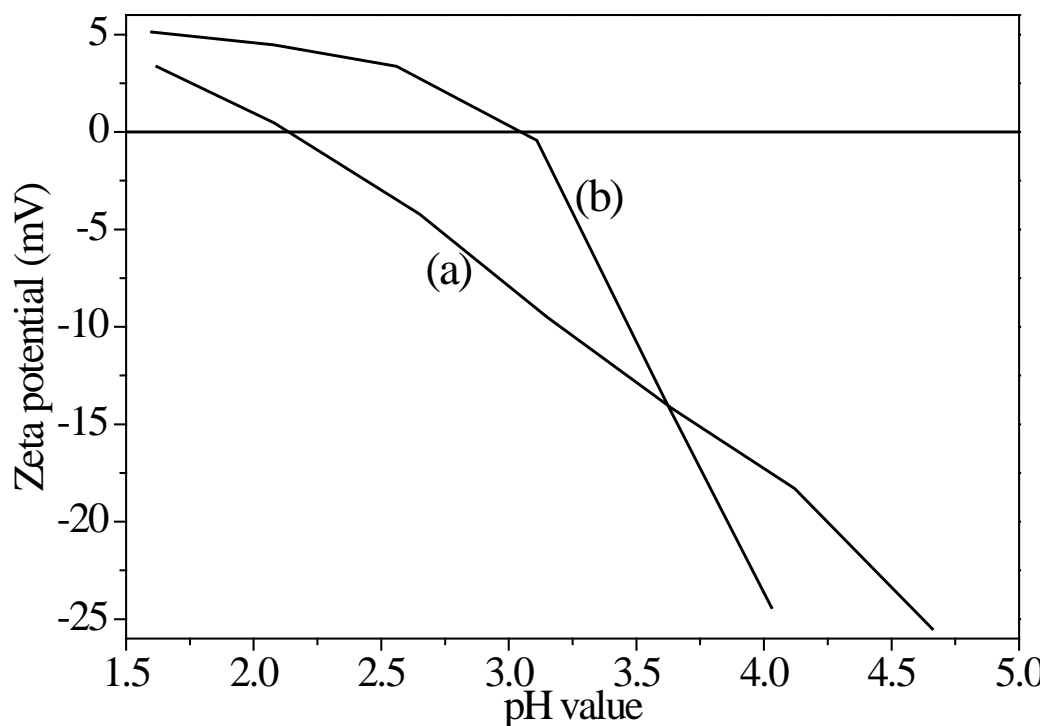
Fig. 4-3 Zeta potentials of (a) SBA-1 and (b) 5Ti-SBA-1-alk supports versus pH values.

The UV-Vis spectra of the calcined Ti-SBA-1-alk samples show a strong absorption around 220 nm, which is corresponding to the charge transfer band of O → Ti in tetrahedral (T_d) coordination (Fig. 4-4). The intensity of the 220 nm band increases with Ti loading in the Ti-SBA-1-alk samples, suggesting that more isolated Ti species are incorporated. When the Ti/Si ratio in gels is increased to 3-5mol%, one moderate absorption band appears around 260 nm., which is assigned to the LMCT (ligand to metal charge transfer) from O to Ti in octahedral coordination.[141,142,143] If Ti substitutes Si in the silica framework, it should be in T_d coordination. The presence of O_h-coordinated Ti infers the formation of extra-framework TiO_2 clusters. The 260 nm shoulder becomes intense when Ti loading increases up to 5mol%, indicating that the amount of Ti in tetrahedral coordination reach maximum and the residual Ti become the extra-framework TiO_2 clusters.

Fig. 4-5 shows SEM images of calcined Ti-SBA-1-alk samples with different Ti/Si molar ratios. The particle sizes of the materials synthesized in alkaline condition varies in a large range from 50 nm to 1 μm in diameter. They are different from the particles of SBA-1 synthesized by acidic route, which have well-defined external morphology with crystal facets, and the particle size was usually in 3–15 μm.[36,39] It is noticeable that the morphology of Ti-SBA-1-alk samples is less uniform than Al-SBA-1-alk shown in Fig. 3-7.
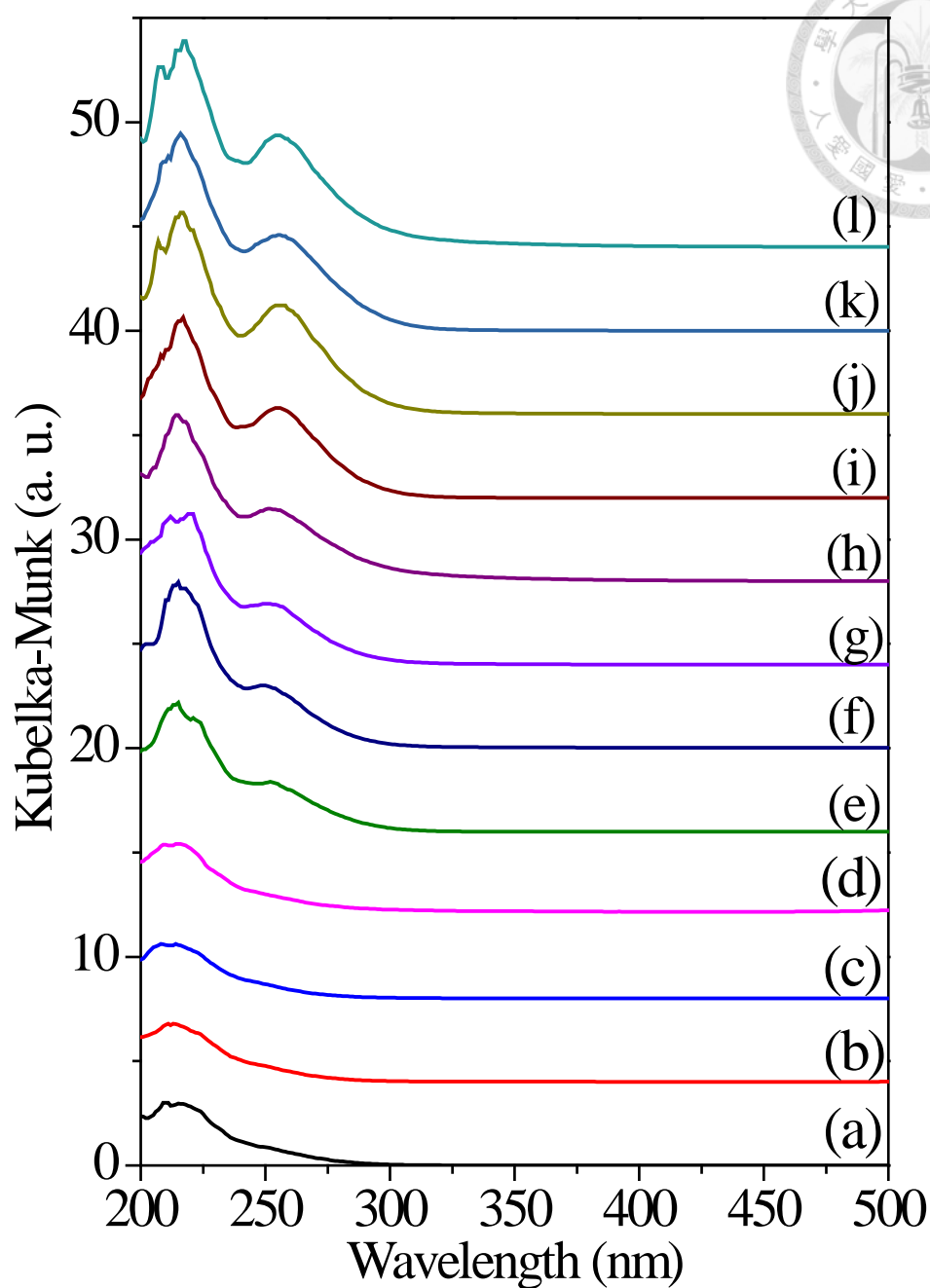
Fig. 4-4 Diffuse reflectance UV-Vis spectra of various samples: (a) 1Ti-SBA-1-alk (b) 5Au^{3+}/1Ti (c) 10Au^{3+}/1Ti (d) 20Au^{3+}/1Ti (e) 3Ti-SBA-1-alk (f) 5Au^{3+}/3Ti (g) 10Au^{3+}/3Ti (h) 20Au^{3+}/3Ti (i) 5Ti-SBA-1-alk (j) 5Au^{3+}/5Ti (k) 10Au^{3+}/5Ti (l) 20Au^{3+}/5Ti
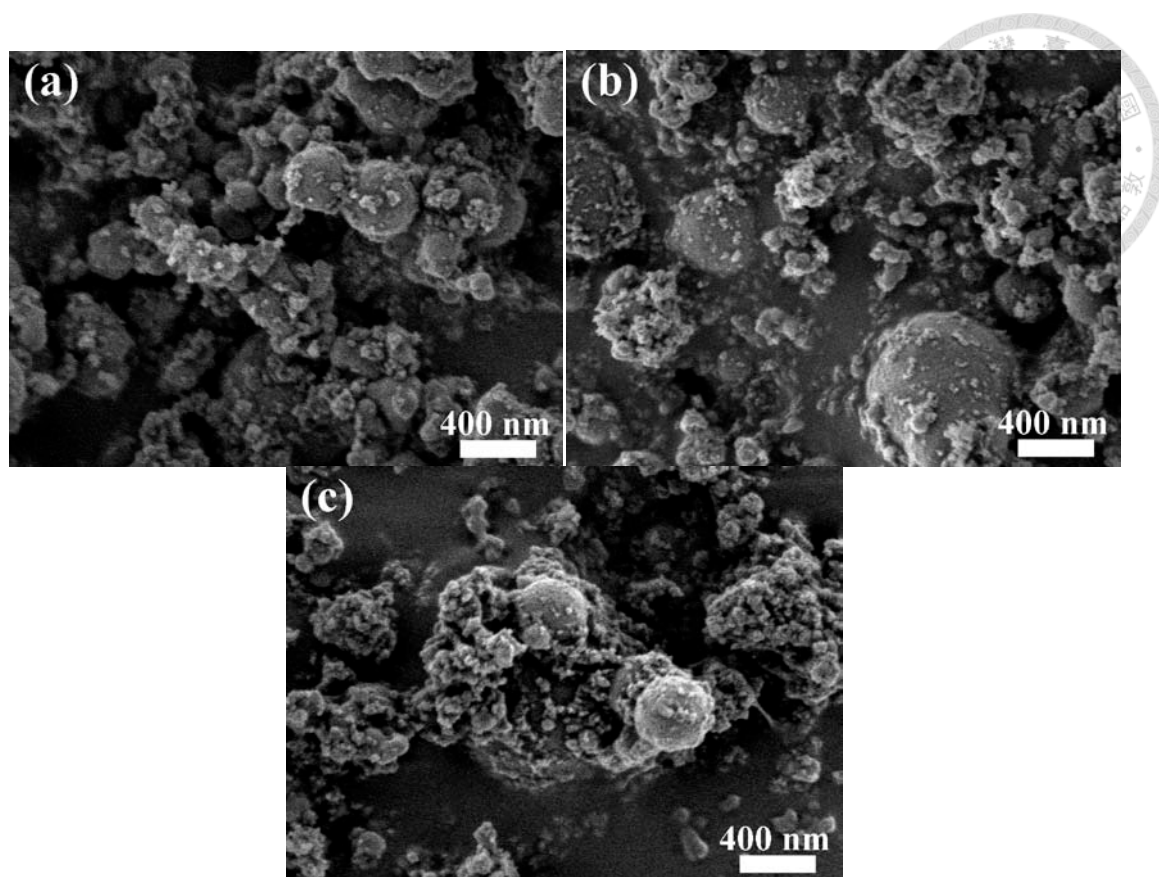
Fig. 4-5 SEM images of calcined Ti-SBA-1-alk samples with different Ti/Si molar ratio percents: (a) 1% (b) 3% (c) 5%.

4.2 Catalytic studies

4.2.1 Effect of the amount of catalyst and reaction temperature

Fig. 4-6 and Table 4-2 show the effect of catalyst amount on the catalytic performance over the $10Au^{3+}/3Ti$ catalyst. The propylene conversion increases slightly and PO selectivity decreases with the space velocity decreasing from 15000 to 5000 mL g_{cat}^{-1} h^{-1}. Higher contact time result in both polymerization of PO to blockage of active sites, and further oxidation of PO to side products, contributing to the relatively low conversion and PO selectivity reduction. The catalyst deactivation is also close related to the degree of polymerization of PO. As shown in Fig. 4-6, when the catalyst amount is raised from 0.1 g to 0.3 g, the conversions of 5.1, 6.2, 7.4% at initial time decay to 2.5,

2.7, 3.0% after reaction time of 600 min. The decay rates increase from 51 to 59% with the catalyst amount increasing. Besides, the propylene conversion decreases with the reaction time but H_2 conversion, implying that the coke formation takes place mainly on Ti active site instead of gold surface.

Fig. 4-7 shows the catalytic performance over $10Au^{3+}/3Ti$ catalyst with different reaction temperature. The propylene conversion increases to 9.3% when the reaction temperature is conducted at 200 ^{o}C while PO selectivity decreases simultaneously. This result infers that at higher reaction temperature, the rate of PO formation reaction is much fast but the formation of oligomers and further oxidation of PO may also be accelerated considerably.

Furthermore, As shown in Table 4-2, H_2 conversion and H_2 selectivity are very sensitive to the reaction temperature. When the reaction temperature is raised from 160 ^{o}C to 200 ^{o}C, H_2 conversion increases from 17.7% to 50.9% and H_2 selectivity decrease for 38.3% to 6.5%, suggesting that most of H_2 is not involved in the epoxidation reaction and the rate of decomposition of H_2O_2 is boosted at higher reaction temperature. It is noticeable that the acrolein selectivity increased to 54.2 at the reaction temperature of 200 ^{o}C. The reason for this result is still unclear so far. All possible reaction pathway are illustrated in Scheme 4-1. The main reaction is the epoxidation of propylene to form the PO and the side product is H_2O. The side reaction is the isomerization of PO to acetone and propanal.[144,145] The other side reaction is acrolein formation through oxidation of propene.

It is noticeable that H_2 conversion almost keeps the constant with the reaction time increasing for different reaction condition. It is inferred that the coke will be formed around the Ti site instead of gold nanoparticles. In addition, O_2 conversion/H_2

conversion is only dependant on the reaction temperature. The higher reaction temperature, the higher ratio of O_2 conversion/H_2 conversion. In higher reaction temperature, the ratio of O_2 conversion/H_2 conversion is larger than 1, indicating that the side reactions such as acrolein formation, total oxidation to CO_2 and decomposition of H_2O_2 are more favored.
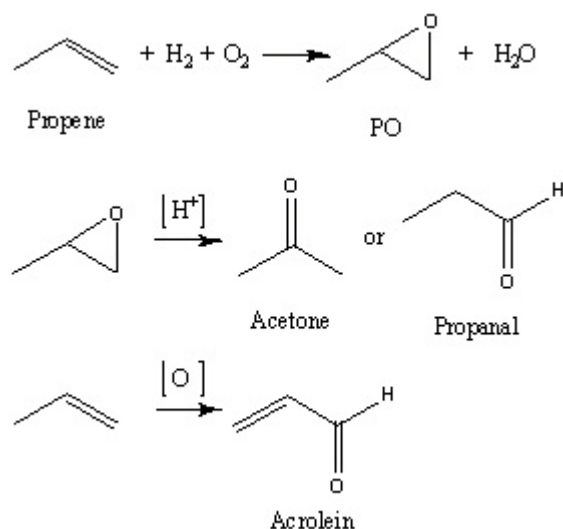
Scheme 4-1 Possible reaction ways for direct phase propylene epoxidation with H_2 and O_2.
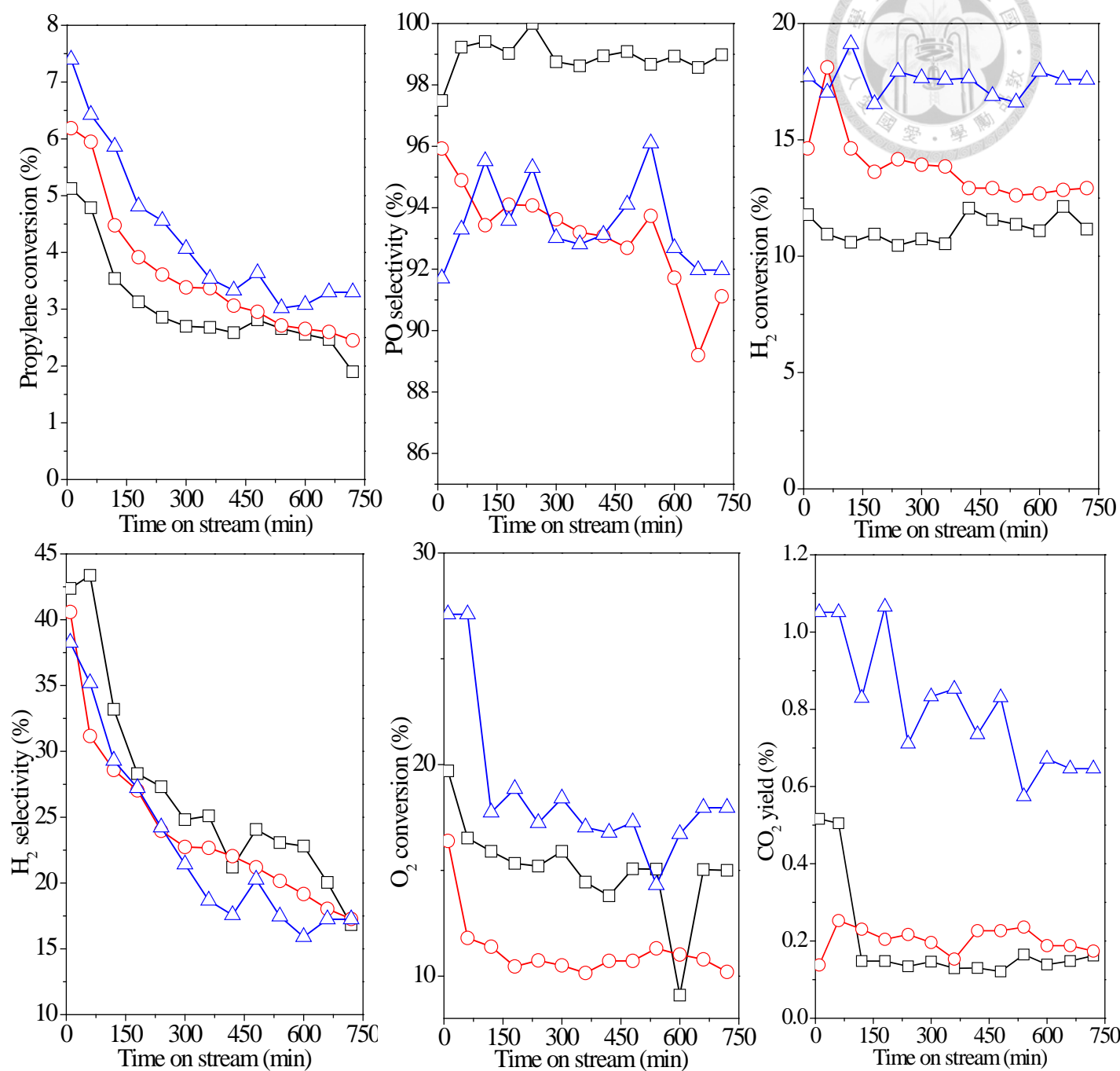
Fig. 4-6 Effect of catalyst amount on propylene conversion, PO selectivity, H_2 conversion, H_2 selectivity, O_2 conversion and CO_2 yield over $10Au^{3+}/3Ti$: (□) 0.1 g (○) 0.2 g (△) 0.3g.
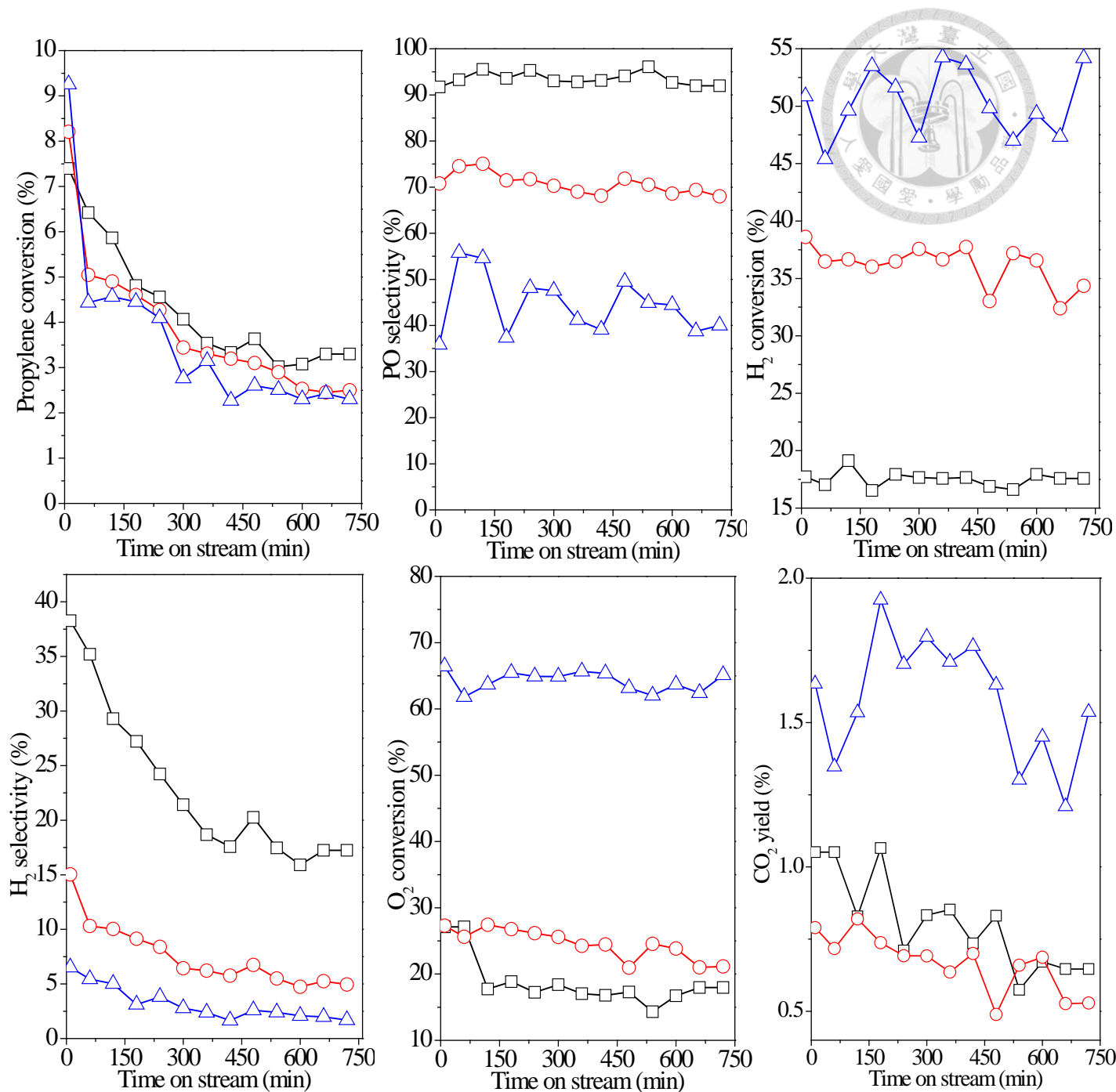
Fig. 4-7 Effect of reaction temperature on propylene conversion, PO selectivity, H_2 conversion, H_2 selectivity, O_2 conversion and CO_2 yield over $10Au^{3+}/3Ti$: (□) 160 ^{o}C (○) 180 ^{o}C (△) 200 ^{o}C.

Table 4-2 Catalytic performance over $10Au^{3+}/3Ti$ catalyst with different catalyst amounts and reaction temperature.

Reaction temp. (^{o}C)	Catalyst amount (g)	Propene conv. (%)	PO yield (%)	H_2 conv. (%)	H_2 select. (%)	Selectivity (%) PO	PA	ACR	ACE	CO_2
160	0.1	5.1	5.0	11.8	42.3	97.5	0.1	1.9	0.5	0.1
160	0.2	6.2	5.9	14.6	40.6	95.9	2.2	1.8	0.1	0.1
160	0.3	7.4	6.8	17.7	38.3	91.7	4.0	2.4	1.8	0.1
180	0.3	8.2	5.8	38.6	15.0	70.2	8.9	22.2	0.2	0.8
200	0.3	9.3	3.3	50.9	6.5	35.9	9.9	54.2	0.1	1.4

[a]reaction condition: reaction time of 10 min, space velocity: 5000 mL min^{-1} g$_{cat}$$^{-1}$ [b]PO: propylene oxide, ACR: acrolein, PA: propanal, ACE: acetone

4.2.2 Influence of gold loadings on the catalytic performance

The catalytic performances of $Au^{3+}/1Ti$ catalysts with different gold loadings are shown in Fig. 4-8. No propylene conversion and H_2 conversion are obtained over $5Au^{3+}/1Ti$ catalyst with the actual gold content of 0.1wt% because of insufficient gold clusters, which is an active site for hydrogen peroxide formation.[110] As the gold loading increases from 0.1 to 0.6wt%, H_2 conversions proportionally increase, implying that H_2 reacted with O_2 on the gold surface and then more H_2O_2 is produced, giving rise to the increase in the propylene conversion.

Besides, the size of gold nanoparticles is particularly important for epoxidation reaction. The particle size and its size distribution of reacted catalysts are examined by TEM, shown in Fig. 4-9. Although 5Au/1Ti and 10Au/1Ti catalysts both have actual gold loadings, no gold clusters are observable because it is hard to find out gold clusters with the diameter of smaller than 2 nm in TEM images. It is suggested that for 5Au/1Ti and 10Au/1Ti catalysts, the size of gold clusters is smaller than 2 nm. However, the 20Au/1Ti catalyst has higher propylene conversion, suggesting that gold clusters with the diameter of about 3 nm may be more active for epoxidation reaction.
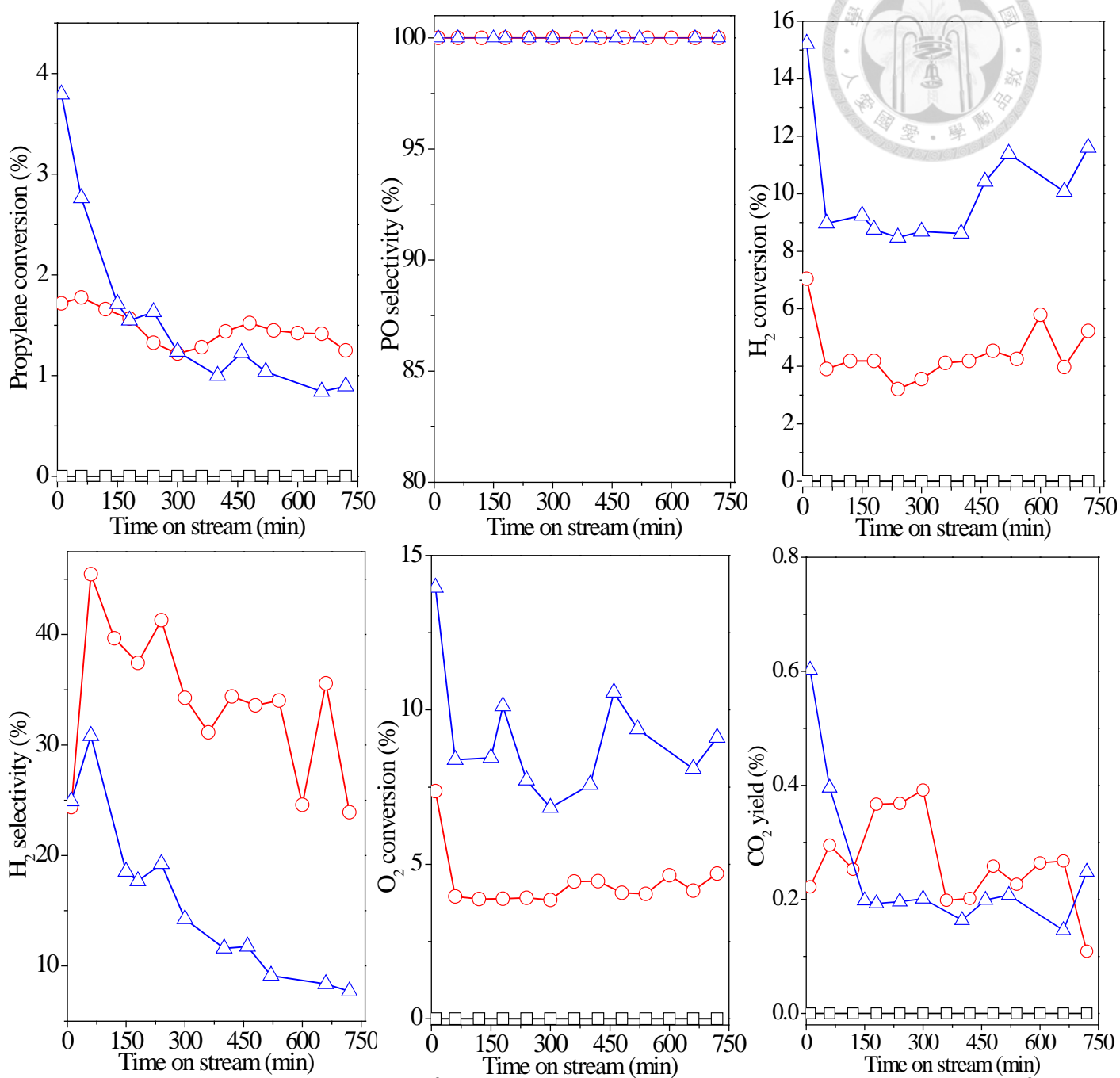
Fig. 4-8 Catalytic performance over $Au^{3+}/1Ti$ catalysts with different gold loadings: (□) $5Au^{3+}/1Ti$ (○) $10Au^{3+}/1Ti$ (△) $20Au^{3+}/1Ti$.

Fig. 4-9 TEM images of Au/1Ti catalysts with different gold loadings and its particle size distribution: (a) 5Au/1Ti (b) 10Au/1Ti (c, c') 20Au/1Ti.

Fig. 4-10 and Fig. 4-12 show catalytic performances of Au^{3+}/3Ti and Au^{3+}/5Ti catalysts as the function of time. These two series of catalysts have the same trend: the highest propylene conversion and PO yield are achieved when the gold loading is 10wt% in the synthesis solution. The poor performance of $20Au^{3+}$/3Ti and $20Au^{3+}$/5Ti catalysts is attributed to the presence of larger gold clusters (Fig. 4-11(c) and Fig. 4-13(c)), which is less active for PO formation and will block Ti sites. Although increasing gold loading will enhance H_2 conversion, the size of gold clusters will also grow up, contributing to low propylene conversion and PO yield. Conversely, the

10Au^{3+}/3Ti and 10Au^{3+}/5Ti catalysts with less actual gold loadings (0.48 and 0.82wt%) have higher propylene conversion and PO yield. The higher catalytic activity over these two catalysts probably results from the smaller gold particle sizes of 3 nm (Fig. 4-11(b') and Fig. 4-13 (b')).

The TEM images show that the sizes of most of gold particle are in range of 3 to 4 nm and the values are bigger than the pore size of SBA-1 materials listed in Table 4-1 The explanation is that the gold particle is still confined in the pore shown in Fig. 4-11 (c) but the particle will expand to about 4 nm after catalytic reaction.
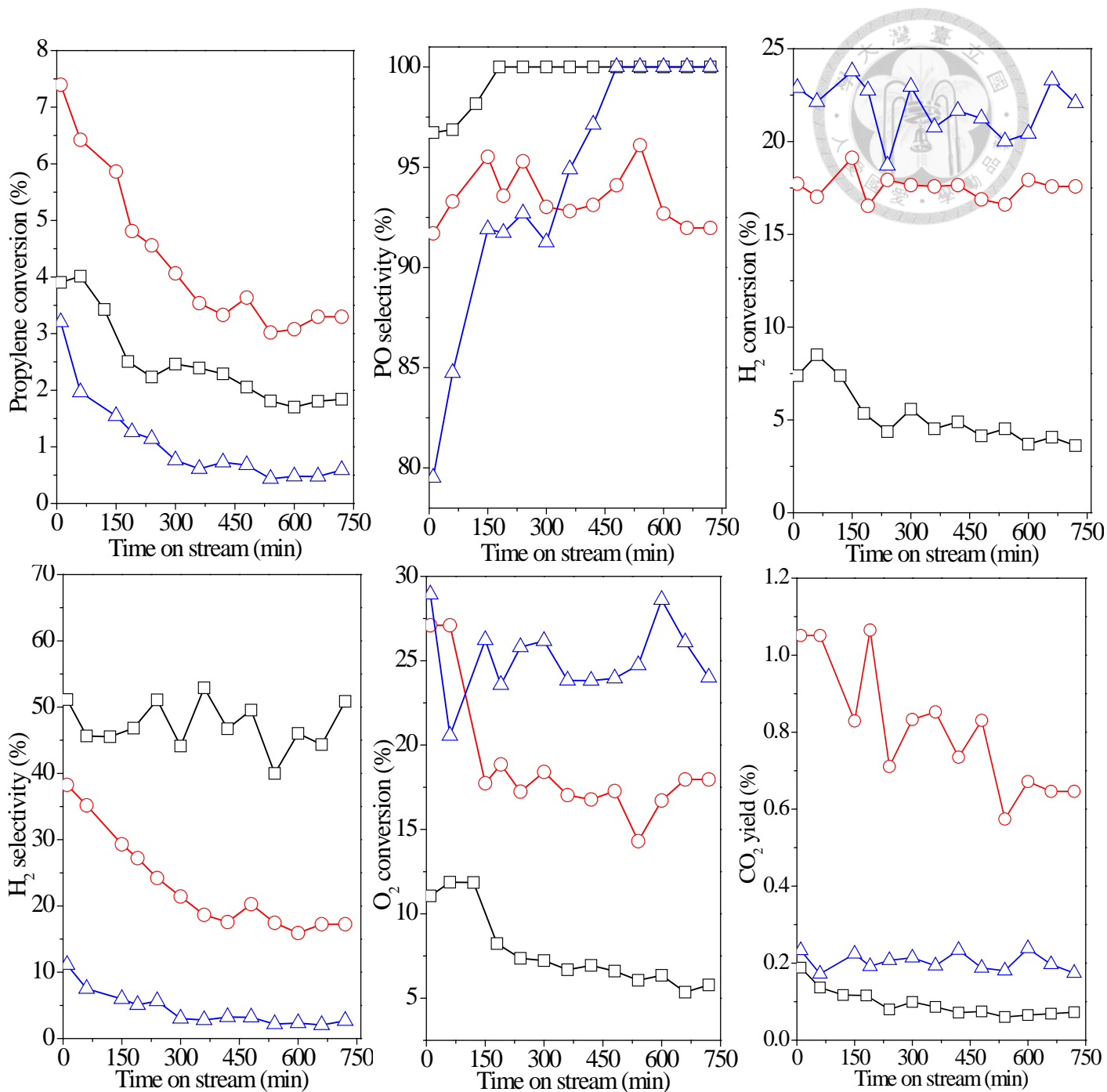
Fig. 4-10 Catalytic performance over Au^{3+}/3Ti catalysts with different gold loadings: (□) 5Au^{3+}/3Ti (○) 10Au^{3+}/3Ti (△) 20Au^{3+}/3Ti.
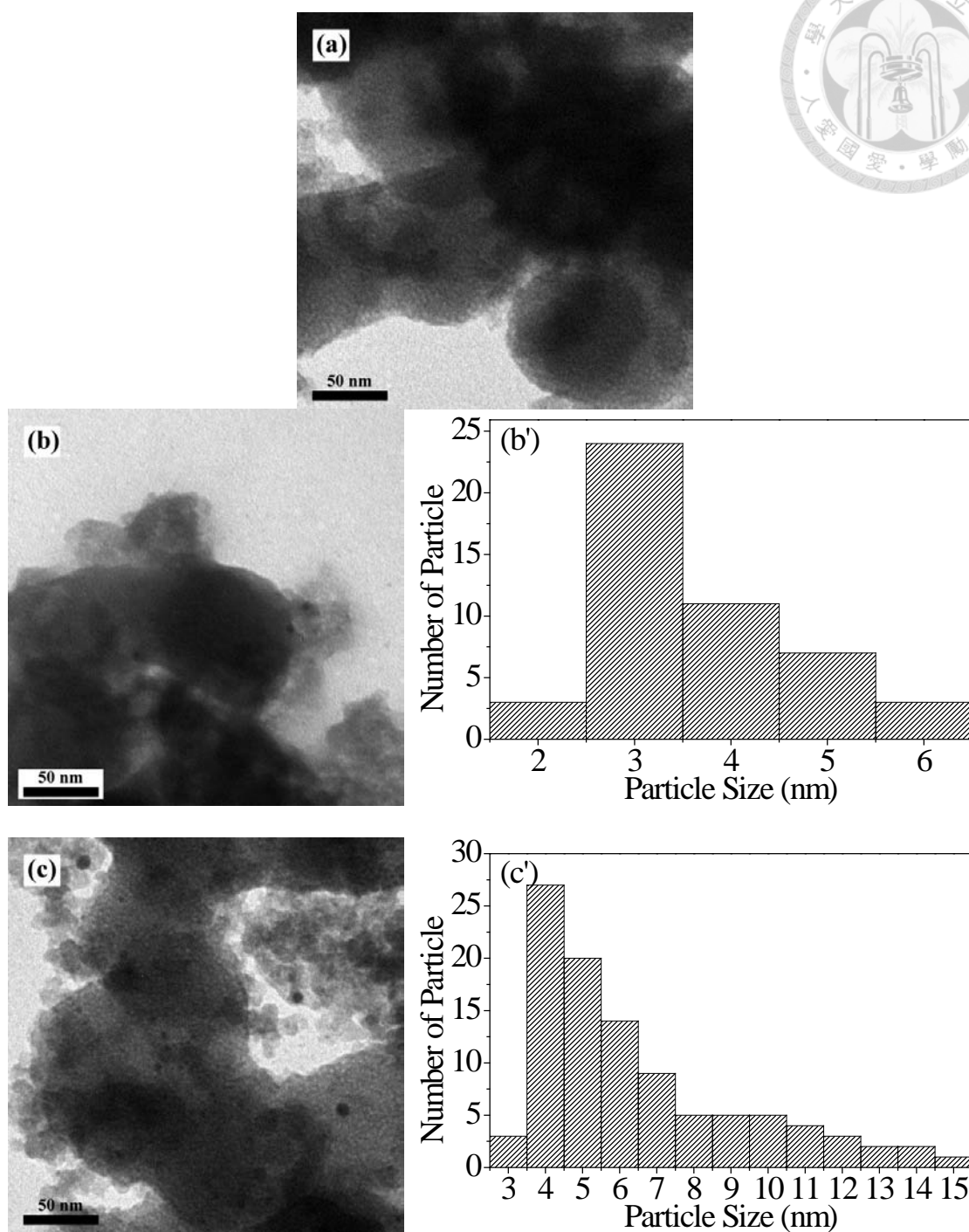
Fig. 4-11 TEM images of Au/3Ti catalysts with different gold loadings and their particle

size distribution: (a) 5Au/3Ti (b, b') 10Au/3Ti (c, c') 20Au/3Ti.
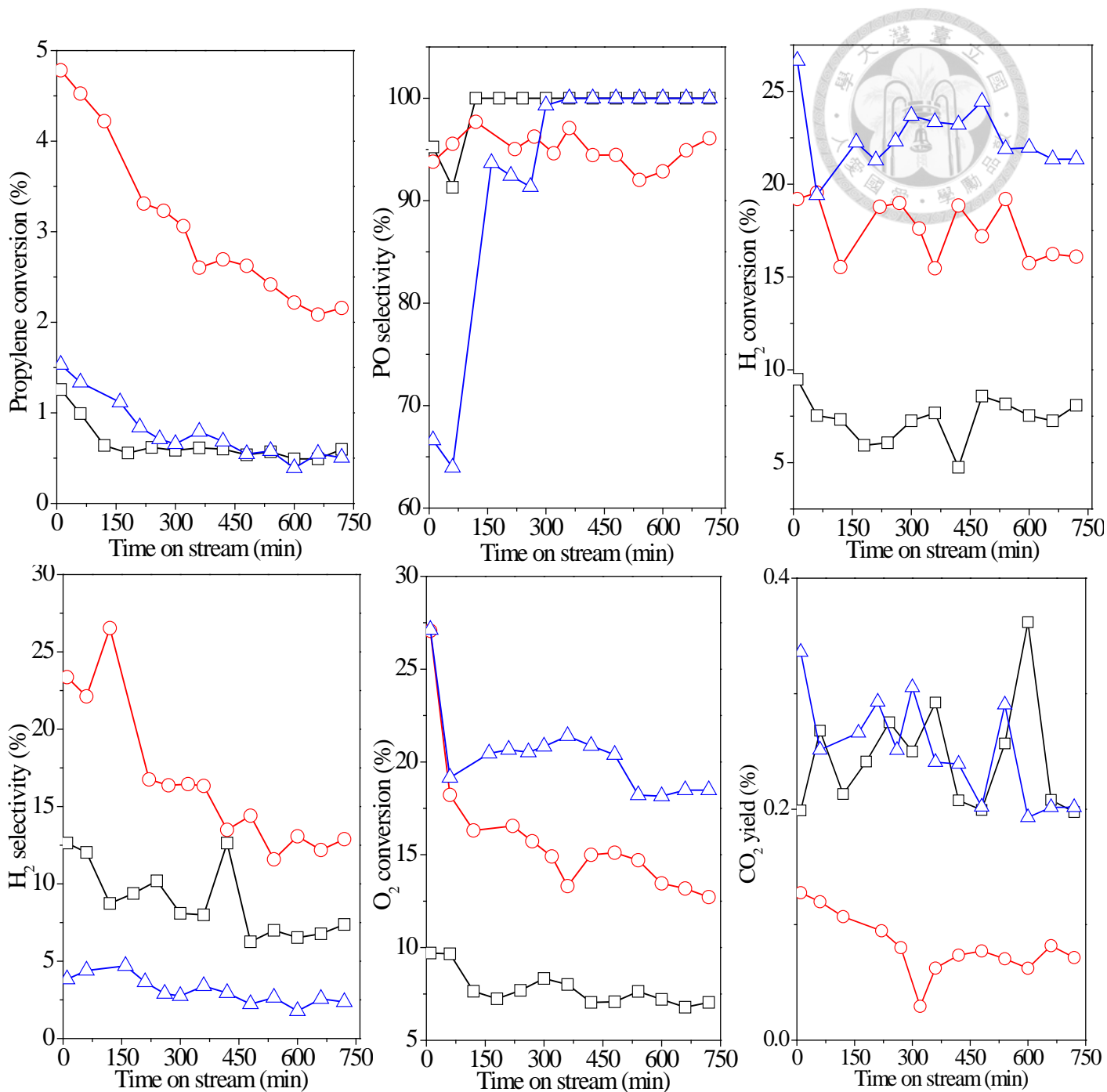
Fig. 4-12 Catalytic performance over $Au^{3+}/5Ti$ catalysts with different gold loadings: (□) $5Au^{3+}/5Ti$ (○) $10Au^{3+}/5Ti$ (△) $20Au^{3+}/5Ti$.
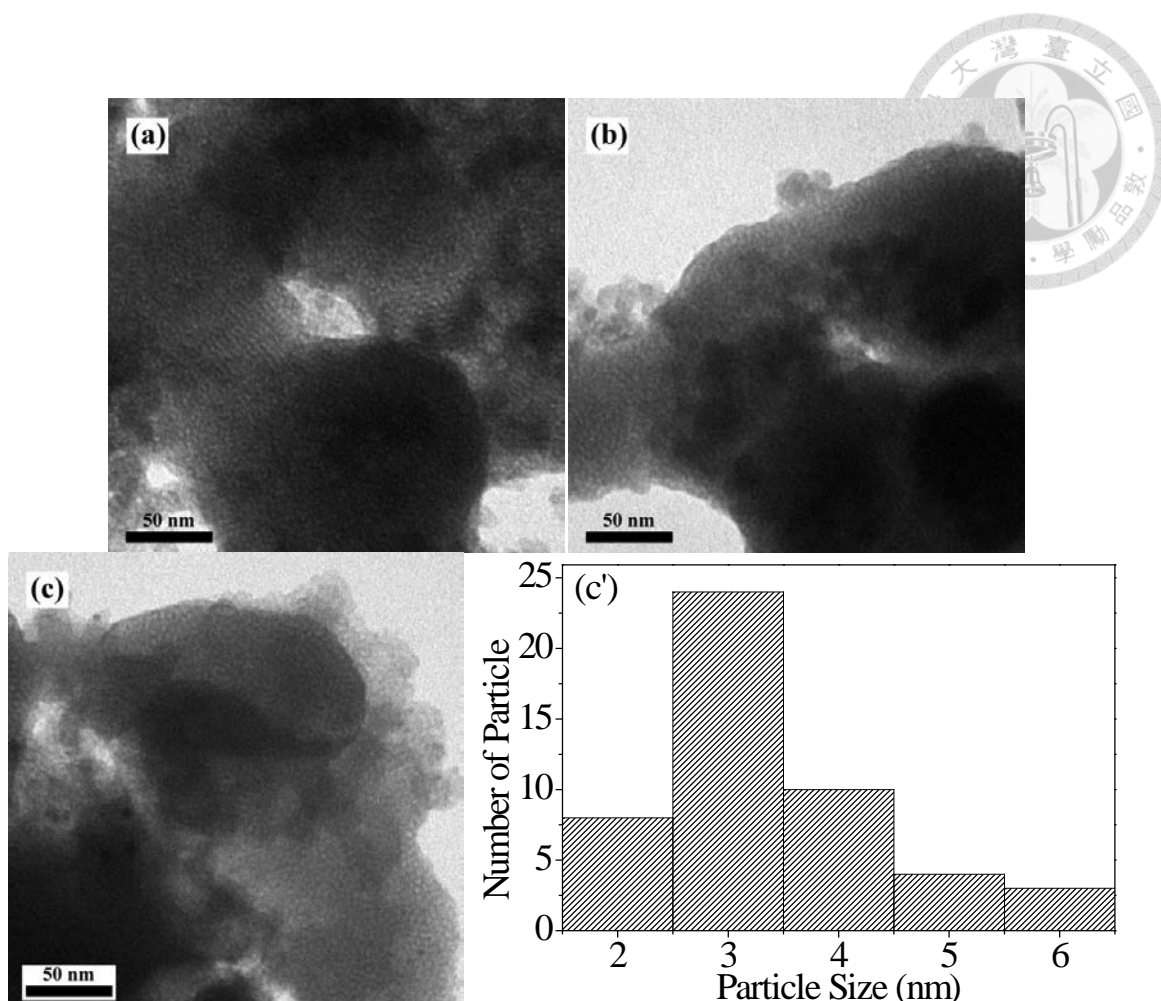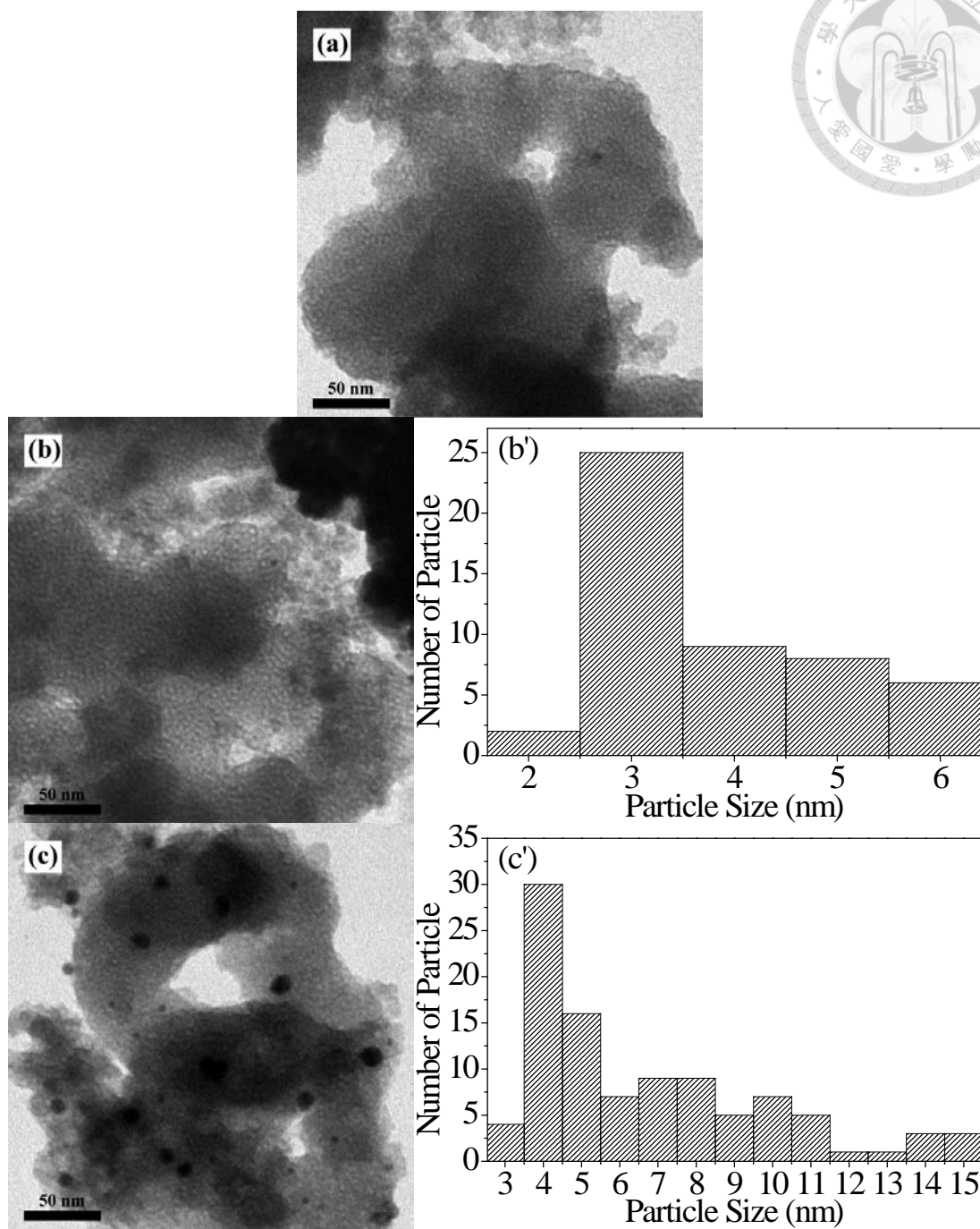
Fig. 4-13 TEM images of Au/5Ti catalysts with different gold loadings and their particle

size distribution: (a) 5Au/5Ti (b, b') 10Au/5Ti (c, c') 20Au/5Ti.

Fig. 4-14 and Fig. 4-15 show XRD patterns and diffuse reflectance UV-Vis spectra of reacted catalysts. Except 20Au/3Ti and 20Au/5Ti catalysts, no diffraction peaks are detected, suggesting that the particle sizes of gold clusters are smaller than 5 nm. The 20Au/3Ti and 20Au/5Ti catalysts have broad diffraction peak for cubic gold at $2\theta = 38^{\circ}$, which correspond to the crystal planes of (111). The UV-Vis spectra of these two catalysts also display one weak band at 520 nm, which is assigned to surface plasma resonance (SPR) band of the metallic gold. These results from XRD and UV-Vis are inferring that the 20Au/3Ti and 20Au/5Ti catalysts have larger average particle size, which is corresponding to TEM data. In addition, the catalysts with actual gold loadings of smaller than 1wt% exhibit no SPR band due to the size is too small to be detectable[146].

X-ray absorption near edge spectroscopy (XANES) provides very useful information on chemical oxidation state and coordination geometry of target elements[147,148,149]. Fig. 4-16 shows the Au L_3-edge XANES of reacted samples and all samples have absorption edge at 11919 eV, indicating that Au^{3+} ion will be reduced to metallic gold during the catalytic reaction.

For particles with diameters smaller than 5 nm, the coordination number is a strong and nonlinear function of the particle diameter. This property has been widely used in extended X-ray absorption fine structure spectroscopy (EXAFS) analysis to determine the size of nanoparticles[150,151,152,153,154]. Furthermore, the amplitude of the EXAFS is indirectly related to the particle sizes. Fig. 4-17 ~ Fig. 4-19 show Au L_3-edge k_3-weighted Fourier transform magnitude of the reacted samples. The FT magnitudes increase with the actual gold loadings. This results is inferred that the size of gold nanoparticles will increase with the actual gold loadings, corresponding to TEM data.

The gold foil with the coordination number of 12 give the highest FT magnitudes in Fig. 4-17.
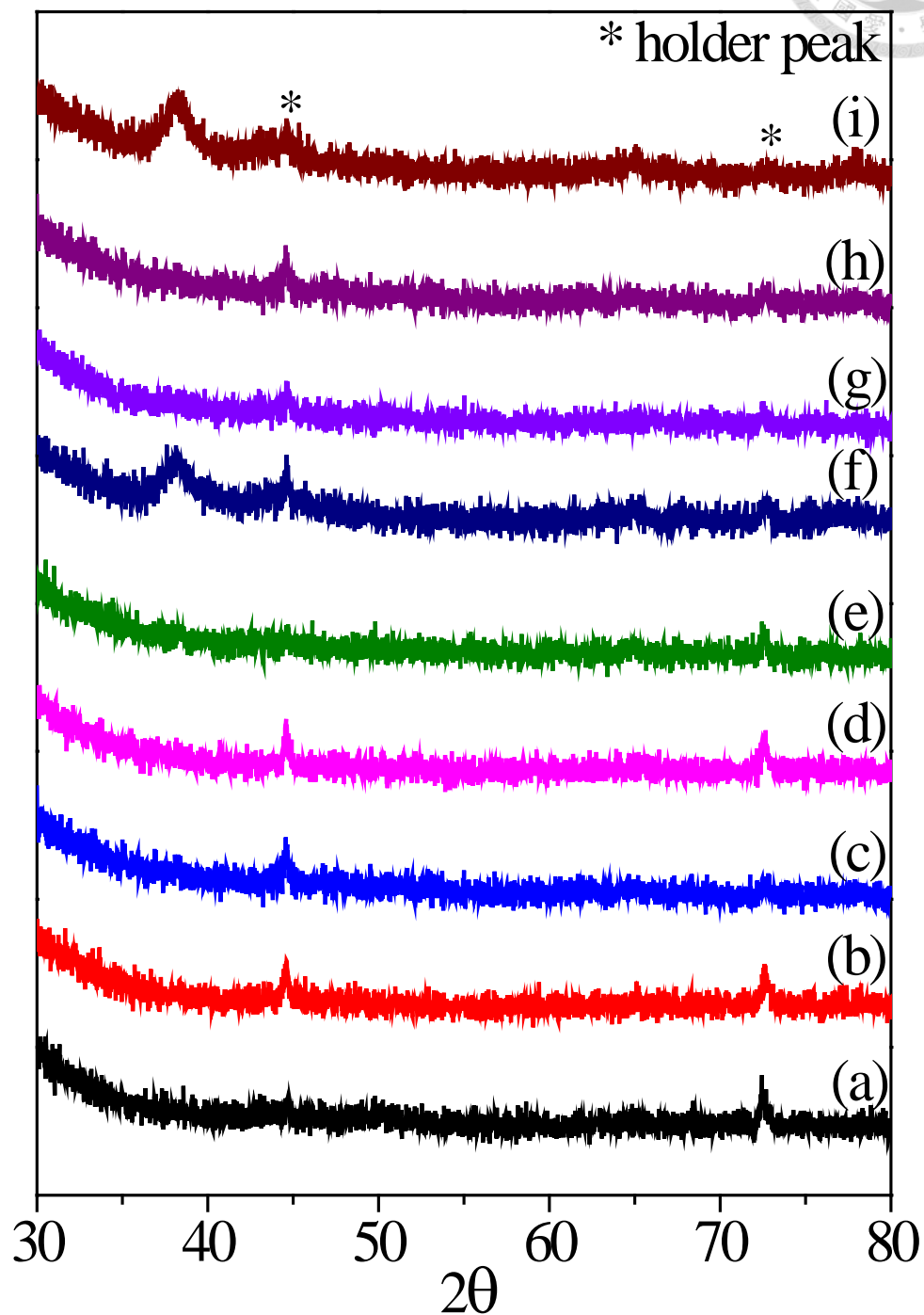
Fig. 4-14 XRD patterns of reacted samples: (a) 5Au/1Ti (b) 10Au/1Ti (c) 20Au/1Ti (d) 5Au/3Ti (e) 10Au/3Ti (f) 20Au/3Ti (g) 5Au/5Ti (h) 10Au/5Ti (i) 20Au/5Ti.
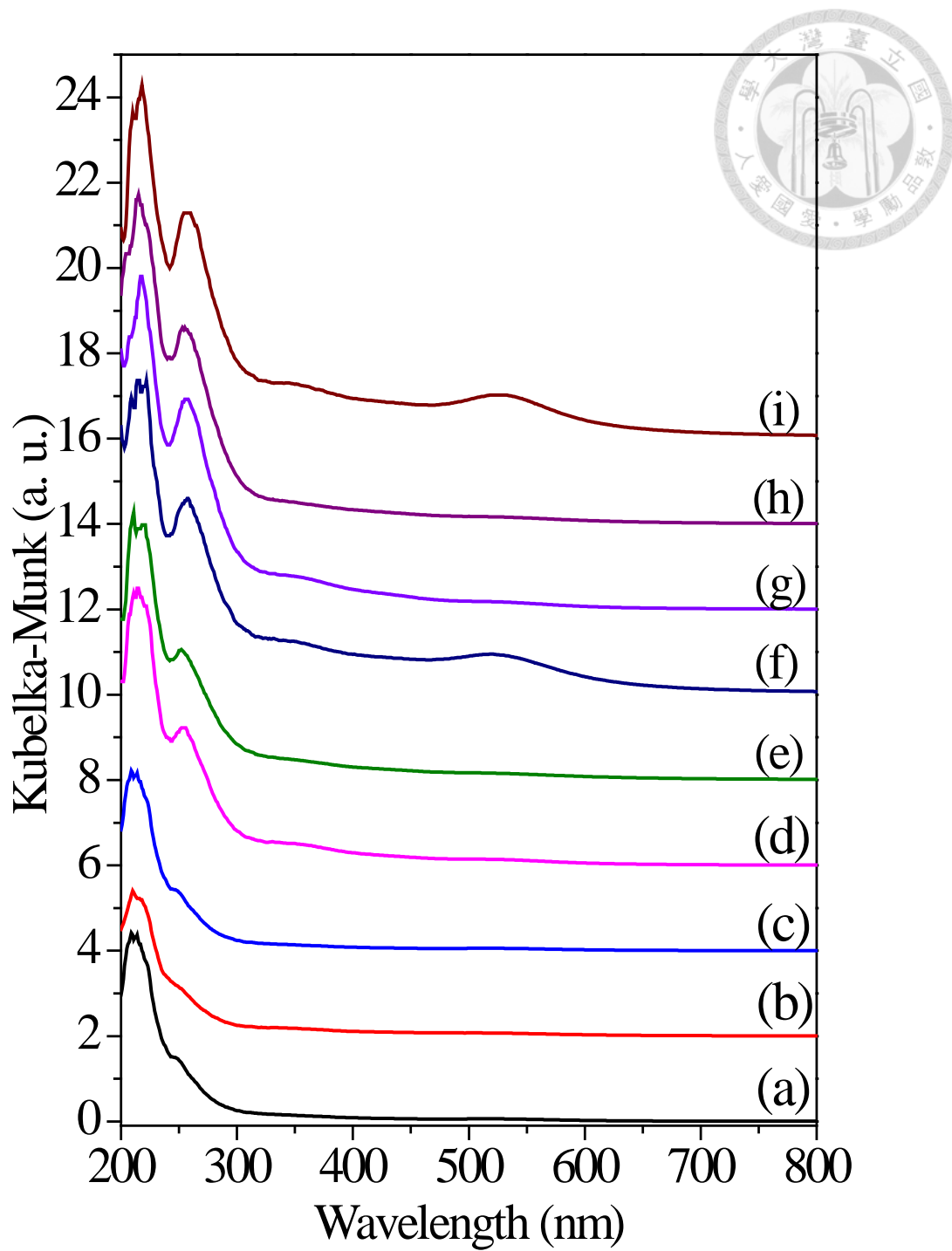
Fig. 4-15 Diffuse reflectance UV-Vis spectra of reacted samples: (a) 5Au/1Ti (b) 10Au/1Ti (c) 20Au/1Ti (d) 5Au/3Ti (e) 10Au/3Ti (f) 20Au/3Ti (g) 5Au/5Ti (h) 10Au/5Ti (i) 20Au/5Ti.
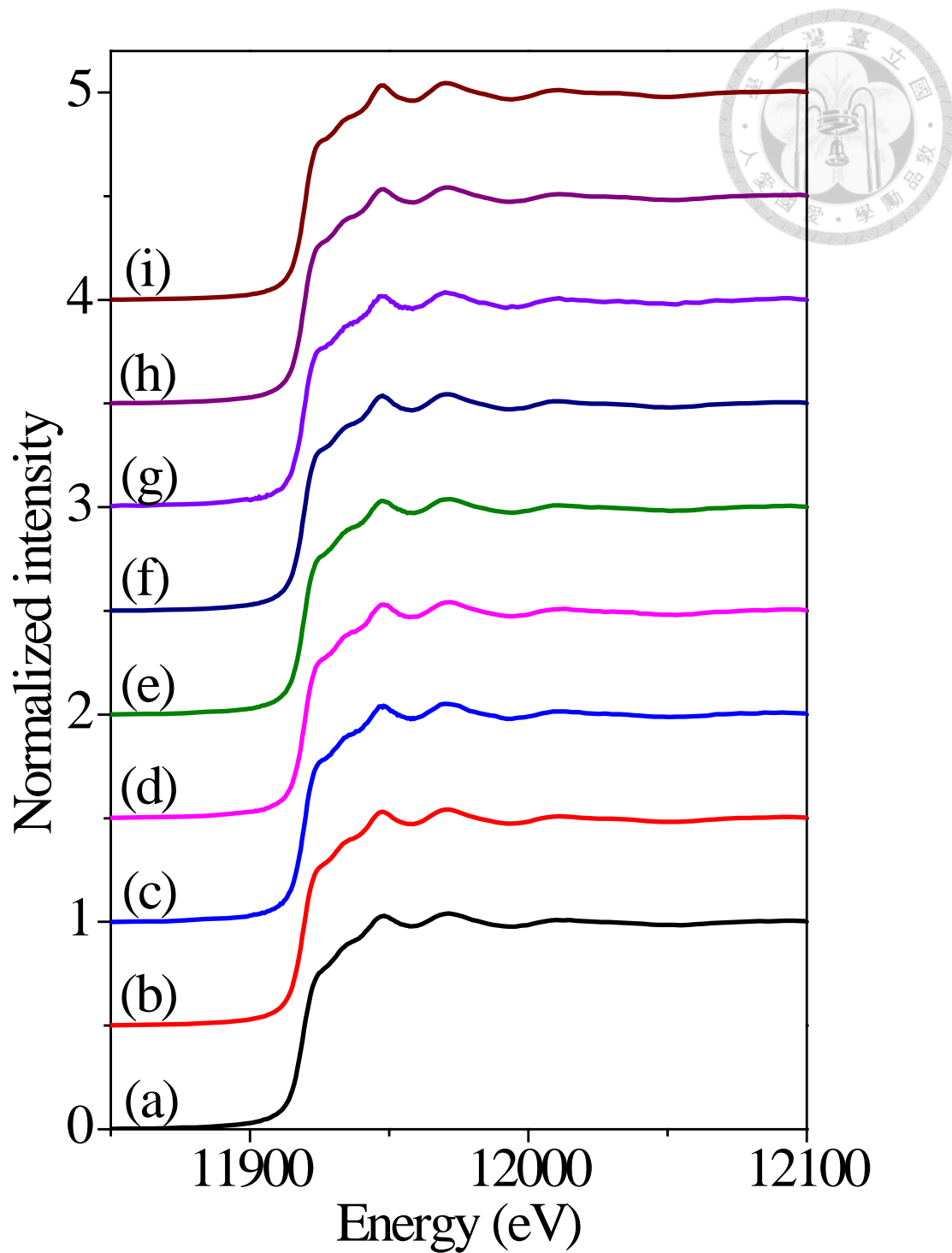
Fig. 4-16Au L$_3$-edge XANES spectra of reacted samples: (a) 5Au/1Ti (b) 10Au/1Ti (c) 20Au/1Ti (d) 5Au/3Ti (e) 10Au/3Ti (f) 20Au/3Ti (g) 5Au/5Ti (h) 10Au/5Ti (i) 20Au/5Ti.
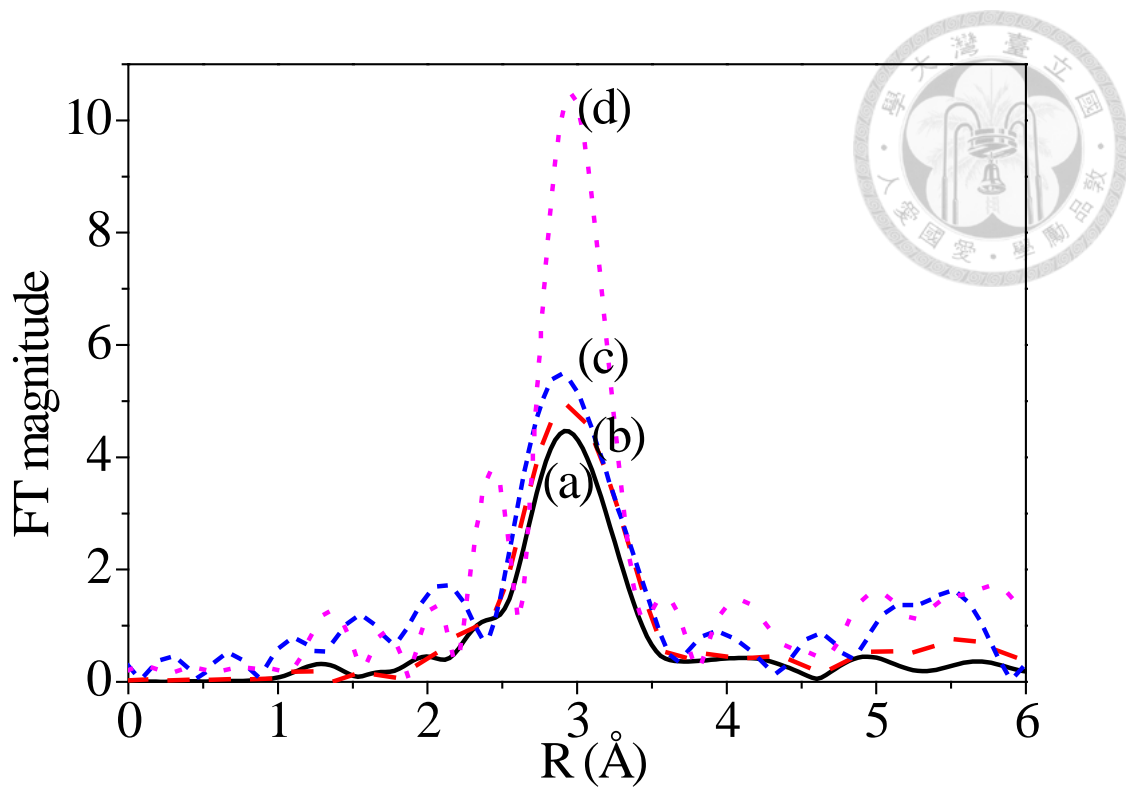
Fig. 4-17 Au L$_3$-edge k_3-weighted Fourier transform magnitude of the (a) 5Au/1Ti (b)

10Au/1Ti (c) 20Au/1Ti (d) Au foil
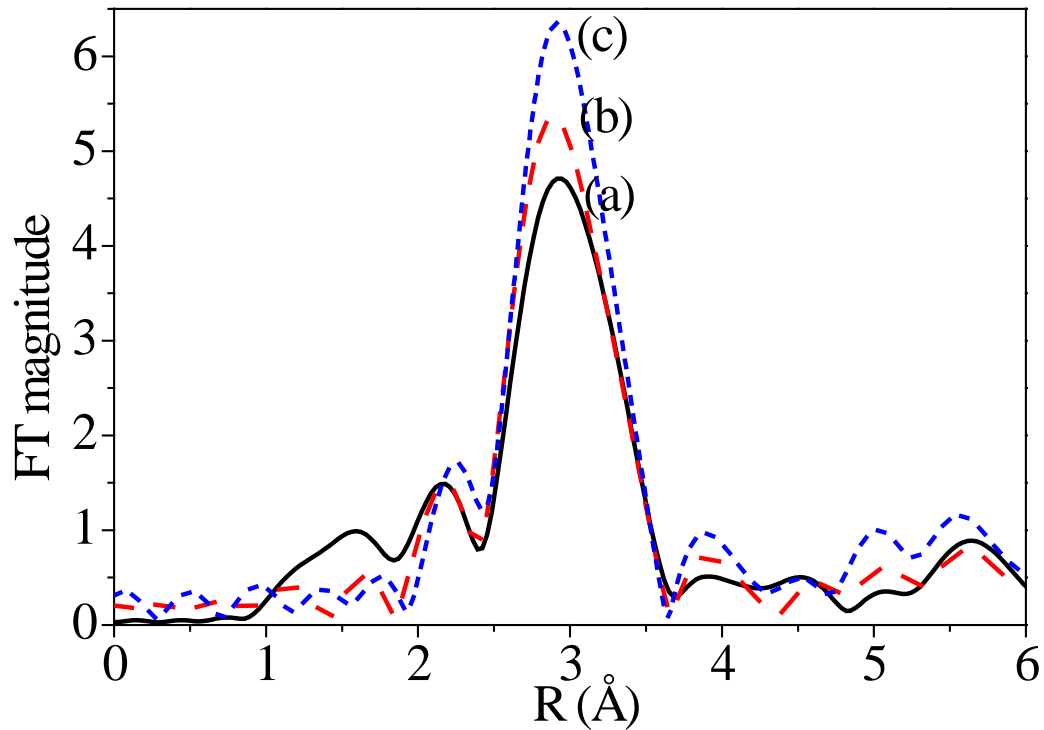
Fig. 4-18 Au L$_3$-edge k_3-weighted Fourier transform magnitude of the (a) 5Au/3Ti (b)

10Au/3Ti (c) 20Au/3Ti.
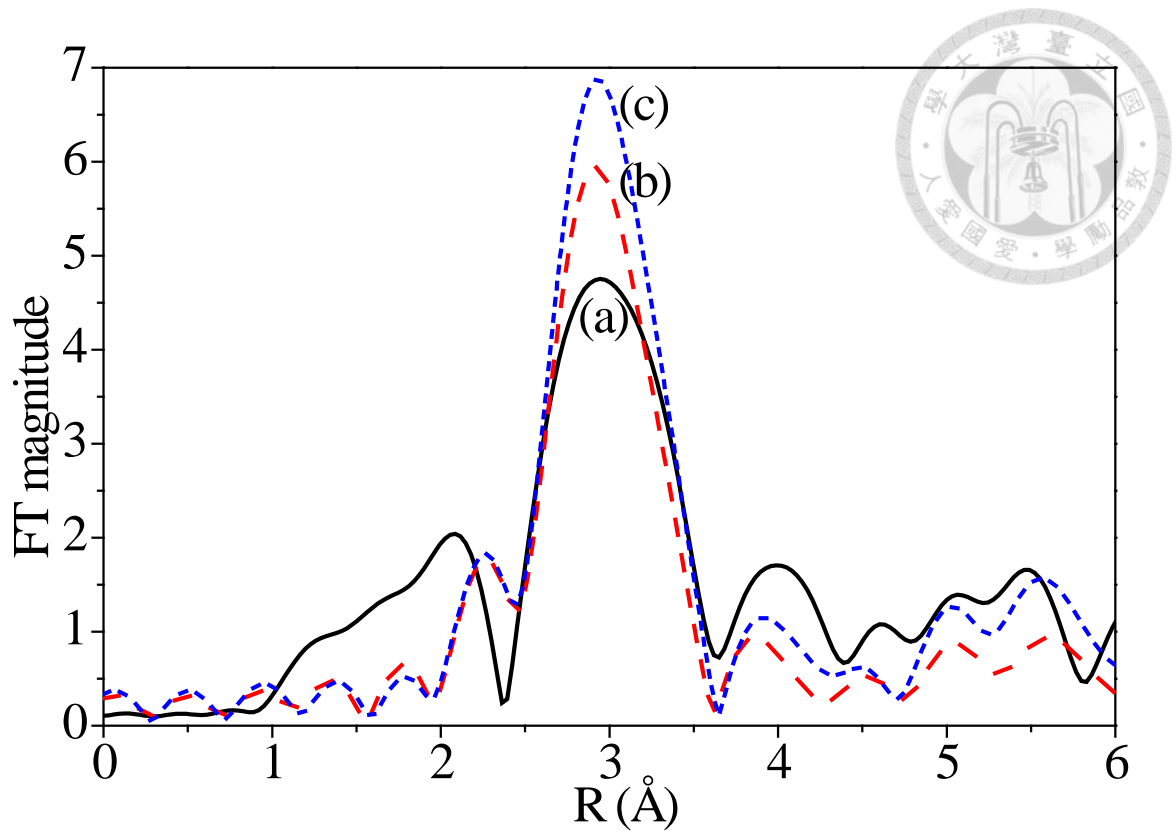
Fig. 4-19 Au L$_3$-edge k_3-weighted Fourier transform magnitude of the (a) 5Au/5Ti (b)

10Au/5Ti (c) 20Au/5Ti

4.2.3 Influence of Ti/Si molar ratio on the catalytic performance

The effect of Ti/Si molar ratio on catalytic performance for $5Au^{3+}/Ti$ catalysts is presented in Fig. 4-20. As Ti content increasing, propylene conversion increases, indicating that Ti site plays an important role for the epoxidation reaction. However, in case of $10Au^{3+}/Ti$ catalysts, the highest conversion and PO yield are obtained when Ti/Si molar ratio is 3% instead of 5% (Fig. 4-21), even though they have similar particle size of 3 nm (Fig. 4-11(b), Fig. 4-13(b)), actual gold loadings (0.48wt%, 0.82wt%) and H_2 conversions. The lower propylene conversion for $10Au^{3+}/5Ti$ is attributed to the extra-framework TiO_2 clusters may catalyze the decomposition of hydrogen peroxide.[155] The other possible explanation is that TiO_2 clusters may block the active sites from the access by H_2O_2 molecules. For the $20Au^{3+}/Ti$ catalysts as shown in Fig. 4-22, the size of gold clusters increases with Ti content increasing, contributing to the lowest propylene conversion of $20Au^{3+}/5Ti$ catalysts.

The catalytic performances of various catalysts with reaction time of 10 min are listed in Table 4-3. Among these samples, the $10Au^{3+}/3Ti$ catalyst with moderately actual gold loadings (0.48wt%) give 7.4% propylene conversion and 6.8% PO yield and H_2 selectivity is 38.3%. It is noticeable that the catalyst with above 1wt% actual gold loadings have higher acrolein selectivity. The reason is still unclear. The blank experimental are tested by 3Ti-SBA-1-alk and $10Au^{3+}/SBA-1$ catalyst. No catalytic activity are shown, indicating that both tetrahedral Ti^{4+} sites and metallic gold nanoparticles are indispensable for propylene epoxidation reaction. Besides, the distance of tetrahedral Ti^{4+} sites and gold nanoparticles is another key factor for this reaction. No catalytic activity is observable when we use the physical mixture of 3Ti-SBA-1-alk and $10Au^{3+}/SBA-1$ as a catalyst.

112
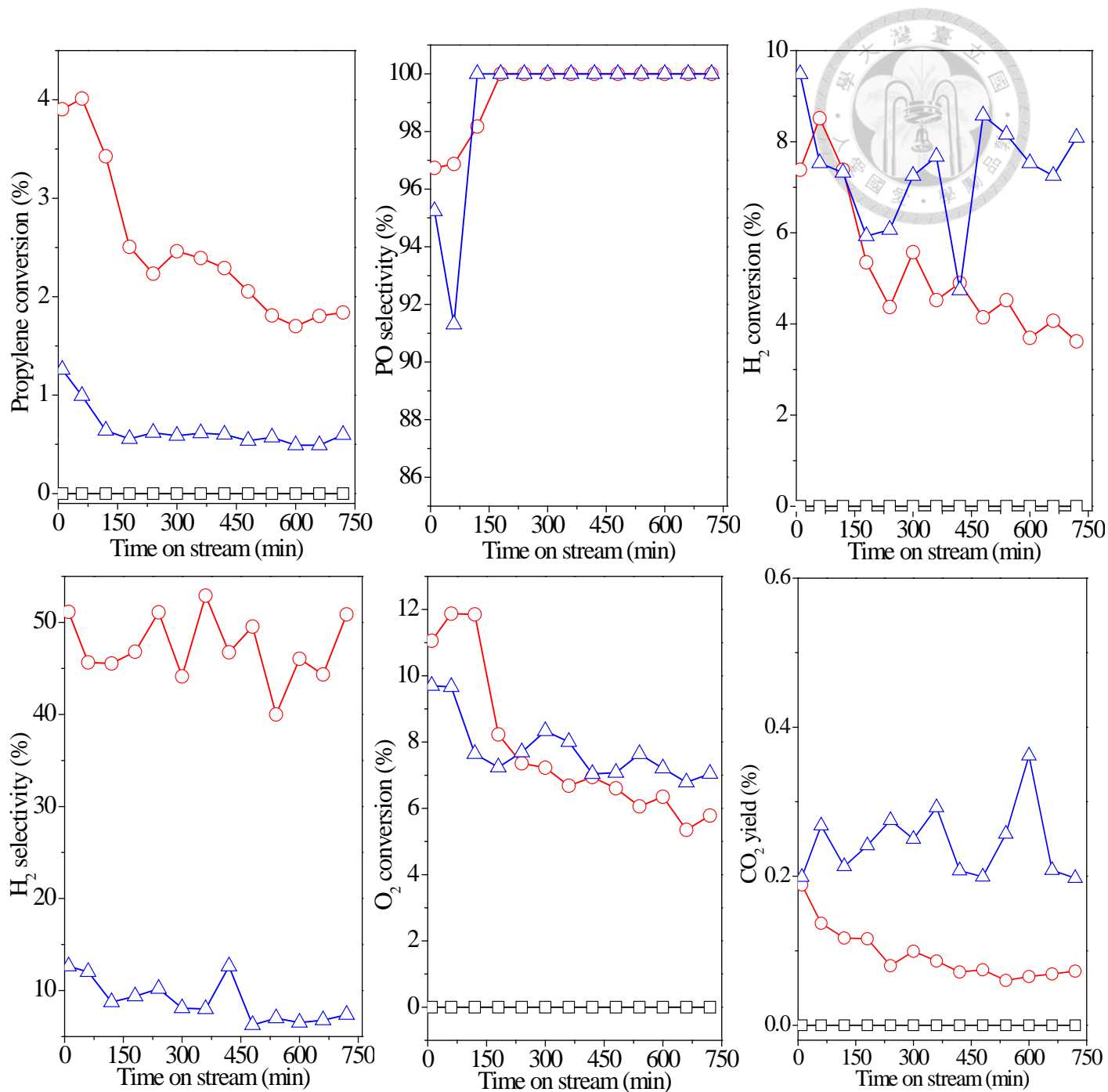
Fig. 4-20 Catalytic performance over 5Au^{3+}/Ti catalysts with different gold loadings: (□) 5Au^{3+}/1Ti (○) 5Au^{3+}/3Ti (△) 5Au^{3+}/5Ti.
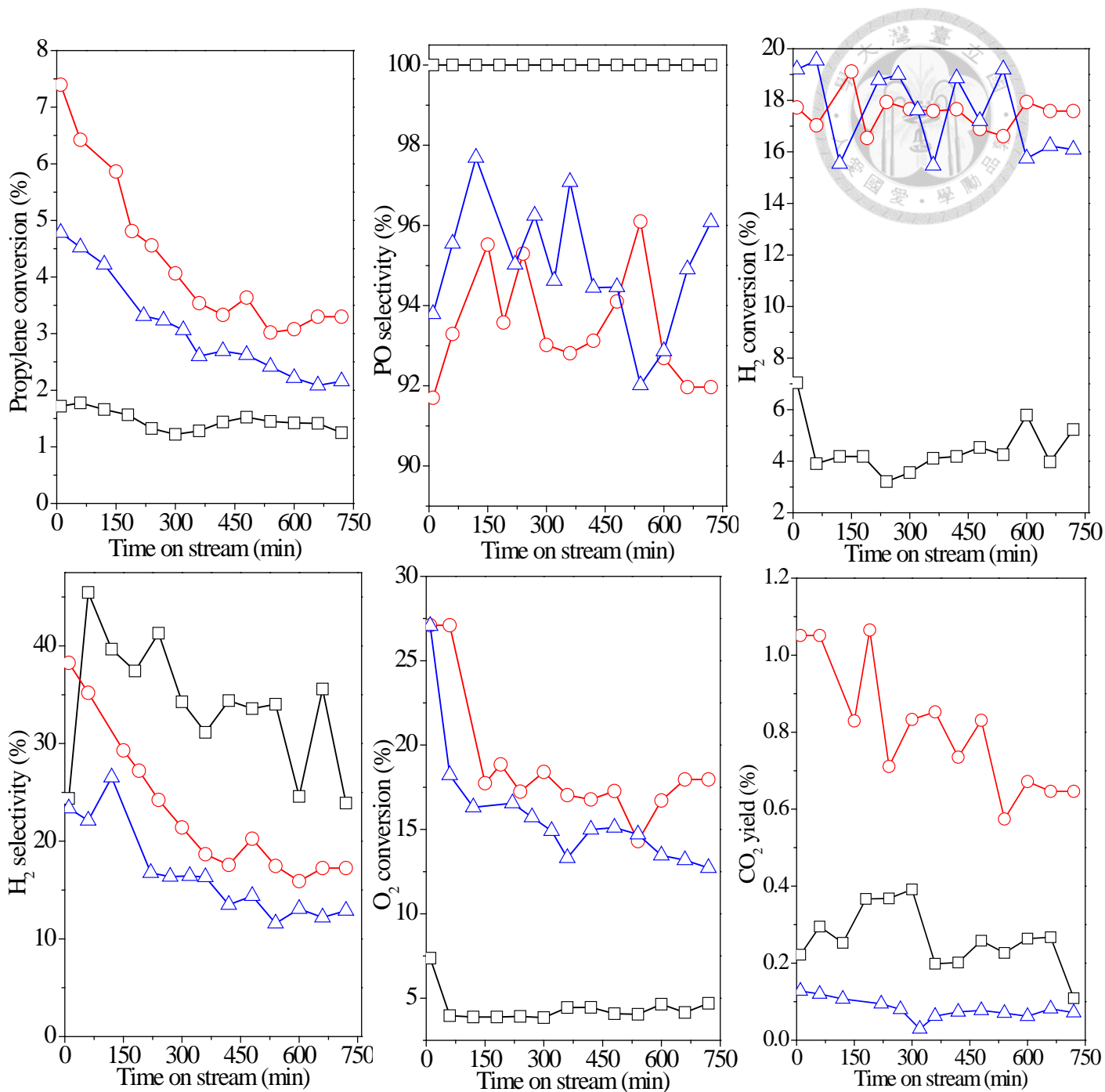
Fig. 4-21 Catalytic performance over $10Au^{3+}/Ti$ catalysts with different gold loadings: (□) $10Au^{3+}/1Ti$ (○) $10Au^{3+}/3Ti$ (△) $10Au^{3+}/5Ti$.

114
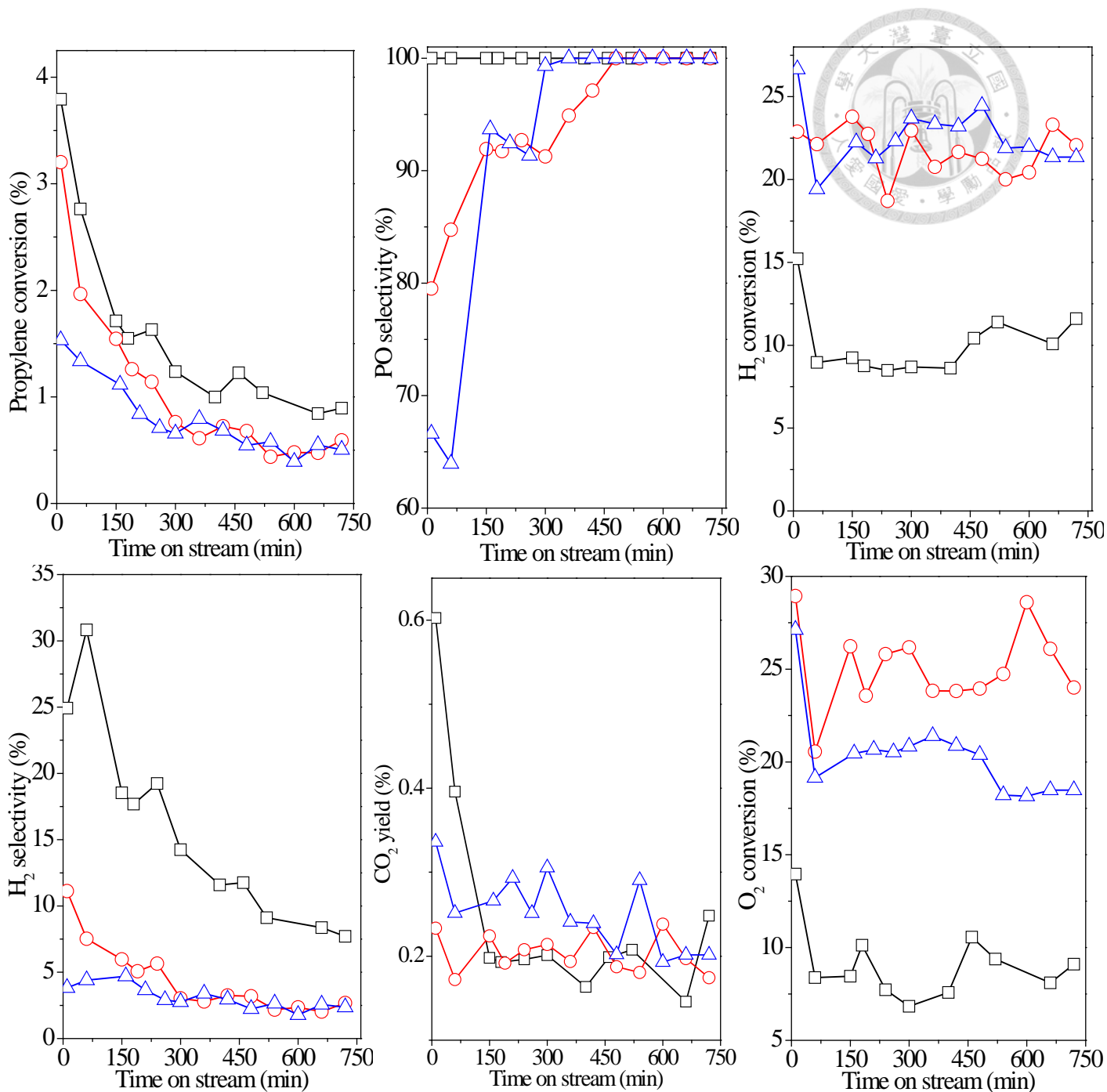
Fig. 4-22 Catalytic performance over 20Au^{3+}/Ti catalysts with different gold loadings: (□) 20Au^{3+}/1Ti (○) 20Au^{3+}/3Ti (△) 20Au^{3+}/5Ti.

Table 4-3 Catalytic performance over various Au^{3+}/Ti catalysts

Catalyst	Propene conv. (%)	PO yield (%)	H_2 conv. (%)	H_2 selectivity (%)	Selectivity (%)				
					PO	PA	ACR	ACE	CO_2
3Ti-SBA-1	< 0.1	-	<1	-	-	-	-	-	-
$10Au^{3+}$/SBA-1	< 0.1	-	<1	-	-	-	-	-	-
$10Au^{3+}$/SBA-1 +3Ti-SBA-1-alk[a]	< 0.1	-	<1	-	-	-	-	-	-
$5Au^{3+}$/1Ti	< 0.1	-	<1	-	-	-	-	-	-
$10Au^{3+}$/1Ti	1.7	1.7	7.0	24.4	99.9	0	0	0	0.1
$20Au^{3+}$/1Ti	3.8	3.8	15.2	24.9	99.9	0	0	0	0.1
$5Au^{3+}$/3Ti	3.9	3.7	7.4	51.1	96.7	0	3.2	0	0.2
$10Au^{3+}$/3Ti	7.4	6.8	17.7	38.9	91.7	4.0	2.4	1.8	0.1
$20Au^{3+}$/3Ti	3.2	2.5	22.9	11.2	79.5	0	20.5	0	0.3
$5Au^{3+}$/5Ti	1.3	1.2	9.4	12.6	95.2	2.8	1.9	0	0.2
$10Au^{3+}$/5Ti	4.8	4.6	19.2	23.4	93.8	2.0	3.3	0.9	0.1
$20Au^{3+}$/5Ti	1.5	1.0	26.7	3.8	66.6	2.4	31.0	0	0.3

[a]catalyst: physical mixture of 0.15 g $10Au^{3+}$/SBA-1 and 0.15 g 3Ti-SBA-1-alk [b]reaction condition: 0.3 g catalysts, 160 °C, 10 min, space velocity: 5000 mL min^{-1} g_{cat}^{-1}

4.2.4 Comparison of catalytic performance over Ti-ZSBA-1 and Ti-SBA-1-alk materials on propylene epoxidation

The hydrothermal time of seed crystallization is a critical factor to synthesize Ti-ZSBA-1 materials. The longer hydrothermal time, the well crystallinity of TS-1 seeds and the larger the particle sizes. However, the size of TS-1 seed is necessarily smaller than 2 nm, which is the wall thickness of SBA-1. Fig. 4-23 show XRD patterns of as-synthesized TS-1 seed for different hydrothermal time. After hydrothermal time of 36 h, all samples were precipitated and detectable by XRD, indicating that the particle size of all samples were larger than 5 nm. The size was too large to be a TS-1 seed. The solution conditions for different hydrothermal time were listed as followed:

Hydrothermal time (h)	Solution condition
0.5	clear
1	clear
2	clear
4	clear
20	clear
24	suspense
36	solid
48	solid
60	solid
72	solid

The clear solution could be obtained before hydrothermal time of 20 h and therefore, the appropriate hydrothermal time is 20 h.
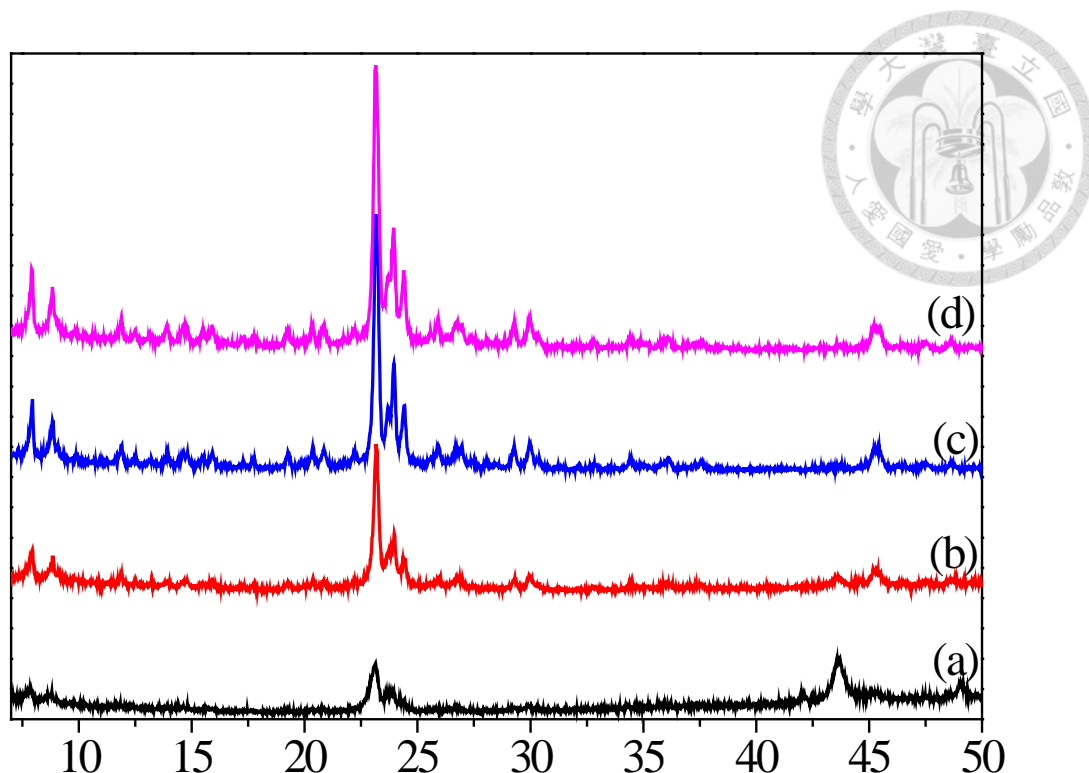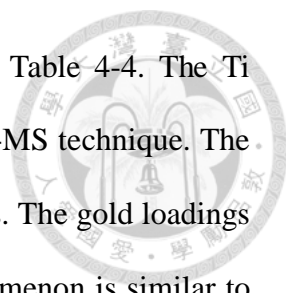
Fig. 4-23 XRD patterns of as-synthesized TS-1 seeds for different hydrothermal time: (a) 36 h (b) 48 h (c) 60 h (d) 72 h.

The gold-deposited Ti-ZSBA-1 materials are prepared by using TS-1 seeds as silica source instead of sodium silicate and XRD patterns are shown in Fig. 4-24. The cubic structures of $10Au^{3+}$/TiZ samples are less order than that of $10Au^{3+}$/Ti samples due to the flexibility of silica source. TS-1 seeds with primary or secondary building units are less flexible than silicate, attributing that it is hard to self-assembly with micelle for TS-1 seeds. Fig. 4-25 show that $10Au^{3+}$/TiZ samples with various Ti loadings have type IV isotherms and H1 hysteresis loops at $P/P_o = 0.25 - 0.35$ and the textural properties derived from sorption isotherms are listed in Table 4-4. All these samples possess mesopores size of 2.0-2.2 nm in diameter, high surface area (900-1100 m^2/g) and large pore volume (0.7 cm^3/g). The physical properties of $10Au^{3+}$/TiZ samples are similar to that of $10Au^{3+}$/Ti samples.

118

The chemical properties of $10Au^{3+}$/TiZ samples are listed in Table 4-4. The Ti content and gold loadings in the solid product are measured by ICP-MS technique. The Ti/Si molar ratios in the solids are close to those in the synthesis gels. The gold loadings of $10Au^{3+}$/TiZ samples increase with Ti/Si molar ratios. This phenomenon is similar to $10Au^{3+}$/Ti samples mentioned in chapter 4.1 Characterization. Besides, the gold loadings of $10Au^{3+}$/1TiZ, $10Au^{3+}$/3TiZ and $10Au^{3+}$/5TiZ samples are 0.31, 0.51, 0.88wt%, respectively. Their gold loadings also similar to $10Au^{3+}$/Ti samples (0.28, 0.48 and 0.91wt% for $10Au^{3+}$/1Ti, $10Au^{3+}$/3Ti and $10Au^{3+}$/5Ti in Table 4-1Table 4-1 Physical and chemical properties of various $10Au^{3+}$/Ti samples.). The UV-Vis spectra of $10Au^{3+}$/TiZ samples with different Ti content are shown in Fig. 4-26. The band at 220 nm is assigned to T^d-coordinated Ti and its intensity increase with Ti/Si molar ratio. The other band at 260 nm is obviously observed for $10Au^{3+}$/5TiZ samples, indicating that the amount of framework Ti sites reach maximum and the extra-framework Ti is formed in higher Ti loadings samples. The particle sizes and morphology of Ti-SBA-1-alk and Ti-ZSBA-1 are examined by SEM shown in Fig. 4-5 and Fig. 4-27. The particle sizes of Ti-ZSBA-1 are in range from 50 nm to 1 μm, similar to those of Ti-SBA-1-alk. From the above characterization, $10Au^{3+}$/TiZ and $10Au^{3+}$/Ti samples both have similar physical and chemical properties.
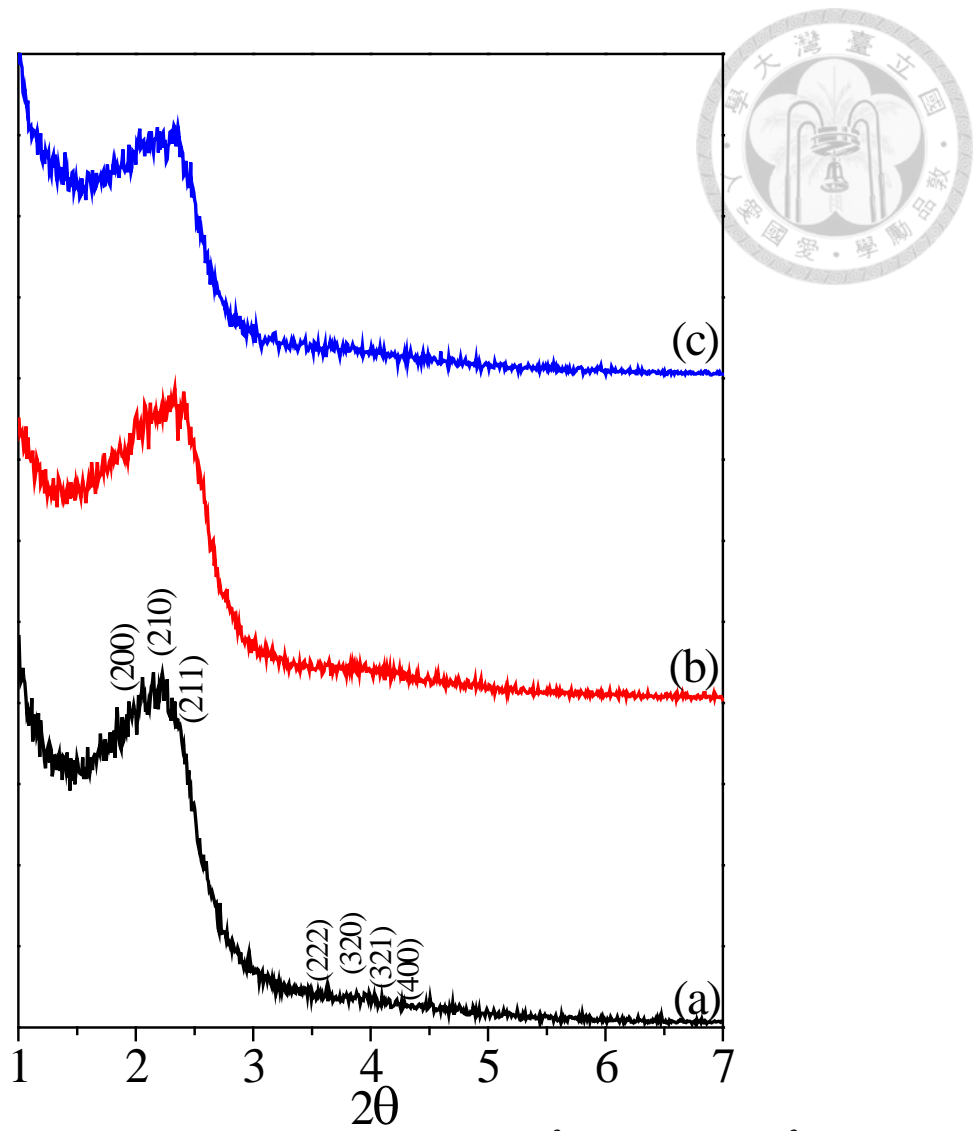
Fig. 4-24 XRD patterns of various samples: (a) $10Au^{3+}/1TiZ$ (b) $10Au^{3+}/3TiZ$ (c) $10Au^{3+}/5TiZ$.
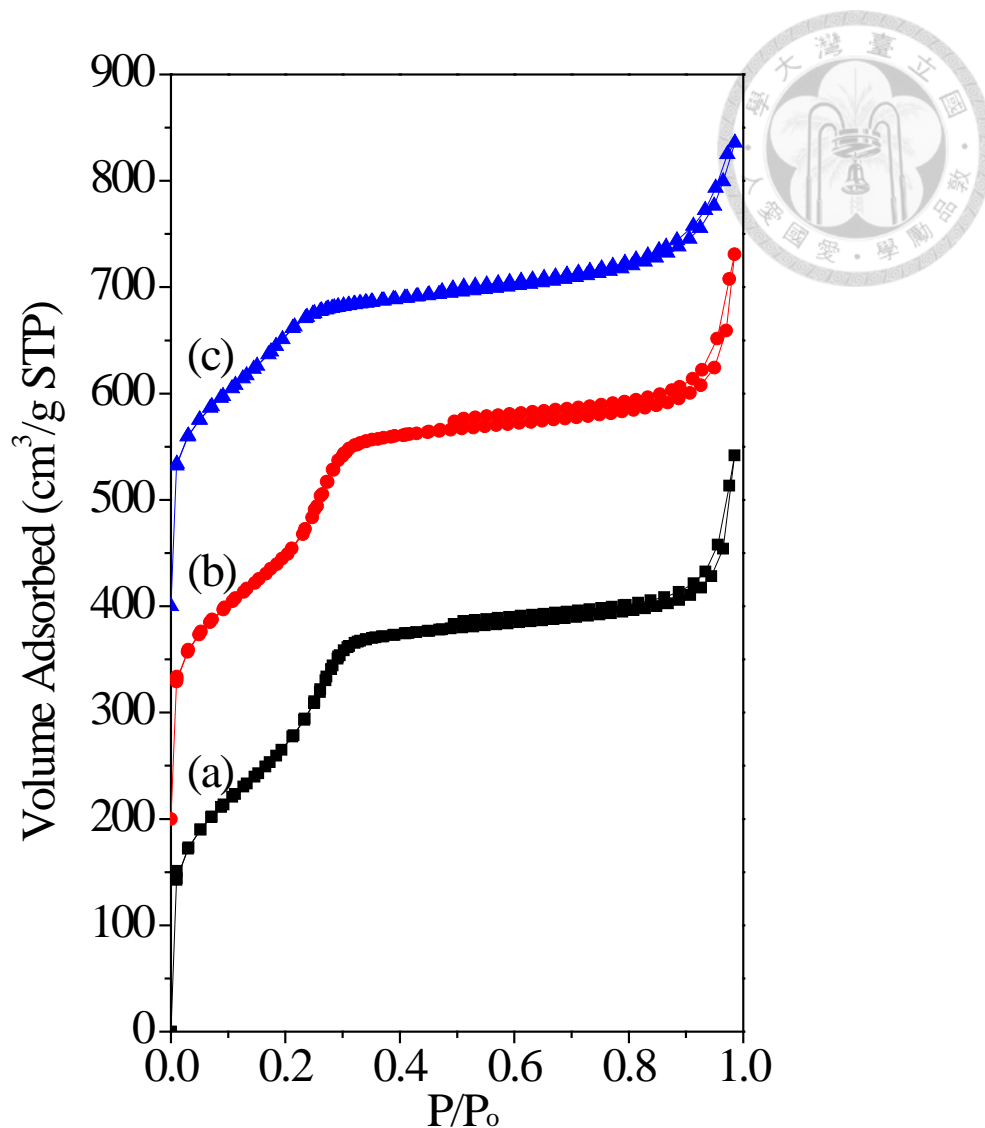
Fig. 4-25 N$_2$ adsorption-desorption isotherms of various samples: (a) 10Au^{3+}/1TiZ (b) 10Au^{3+}/3TiZ (c) 10Au^{3+}/5TiZ. (shifted in vertical axis by 200 cm^3/g STP)

Table 4-4 Physical and chemical properties of various 10Au^{3+}/TiZ samples.

Sample	Ti/Si (mol%)[a]	Au (wt%)	S$_{BET}$ (m^2/g)	D$_p$ (nm)[b]	V$_p$ (cm^3/g)[c]
10Au^{3+}/1TiZ	1.2	0.31	1008	2.2	0.66
10Au^{3+}/3TiZ	3.2	0.51	915	2.2	0.66
10Au^{3+}/5TiZ	5.8	0.88	958	2.0	0.58

[a]determined by ICP-MS [b]calculated from desorption branch [c]calculated at P/P$_o$ = 0.95
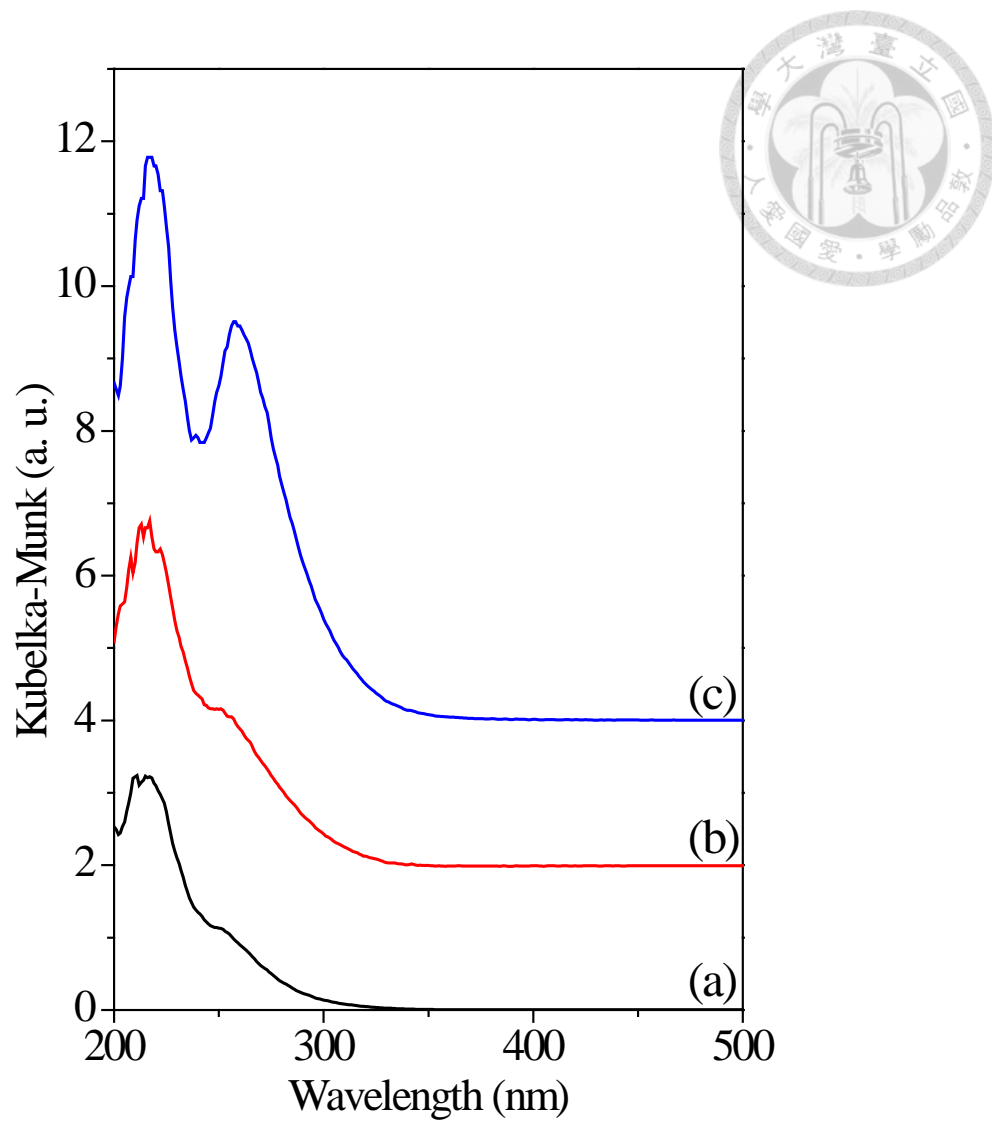
Fig. 4-26 Diffuse reflectance UV-Vis spectra of various samples: (a) $10Au^{3+}/1TiZ$ (b) $10Au^{3+}/3TiZ$ (c) $10Au^{3+}/5TiZ$.
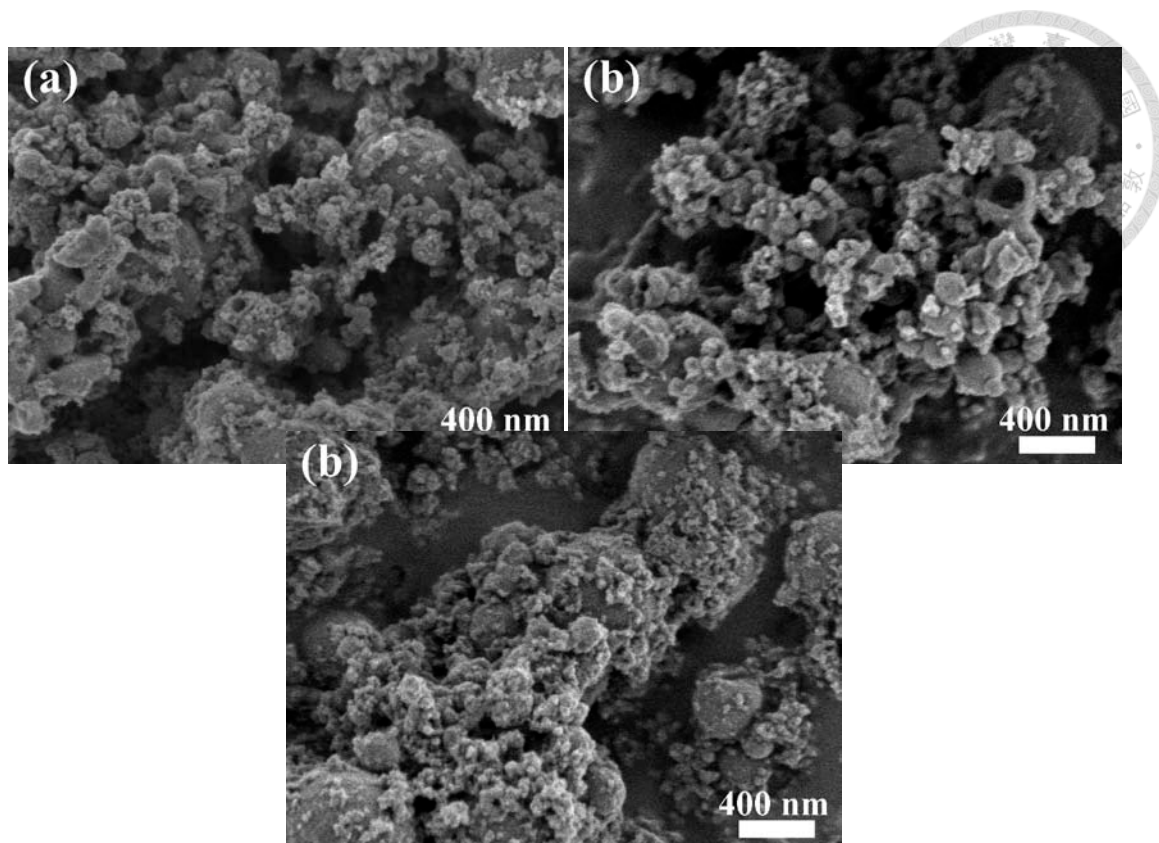
Fig. 4-27 SEM images of calcined Ti-ZSBA-1 samples with different Ti/Si molar ratio percents: (a) 1% (b) 3% (c) 5%.

The comparisons of catalytic performance between $10Au^{3+}$/TiZ and $10Au^{3+}$/Ti with different Ti content are shown in Fig. 4-28~Fig. 4-30 and Table 4-5. For example, the decay rate of $10Au^{3+}$/3TiZ catalyst is 31.1%, which is much smaller than 55.4% of 10Au3+/3Ti catalyst. In 2001, Moulijn group[156] have proposed that the catalyst deactivation occurs via a propoxy species over acid sites of the titanosilicate support. Our catalytic results show that $10Au^{3+}$/TiZ catalysts prepared by using TS-1 seeds as silica source deactivate more slowly. Based on Moulijn group's studies, this result is probably due to a decrease in the number of silanol group, which is acid sites responsible for deactivation. In addition, higher catalytic activity on propylene epoxidation over $10Au^{3+}$/TiZ catalysts is attributed to its more crystallite wall,

123

containing the primary and secondary building units of MFI structure. Beside, the catalytic results collected at reaction time of 600 min are shown in Table 4-5. After reaction time of 60 min, the decay rates are much lower than reaction time of 10 min, indicating that the coke deposit on the external surface instead of active sites.

The catalytic performance of various catalysts on propylene epoxidation are summarized in Table 4-6. The PO formation rate is related to the space velocity. The lower space velocity, the higher PO formation rate. Our catalyst show the PO formation rate of 95 g_{PO} kg_{cat}^{-1} h^{-1} even though the space velocity is low. It is indicated that our materials is a potential catalyst on direct phase propylene epoxidation with H_2 and O_2.
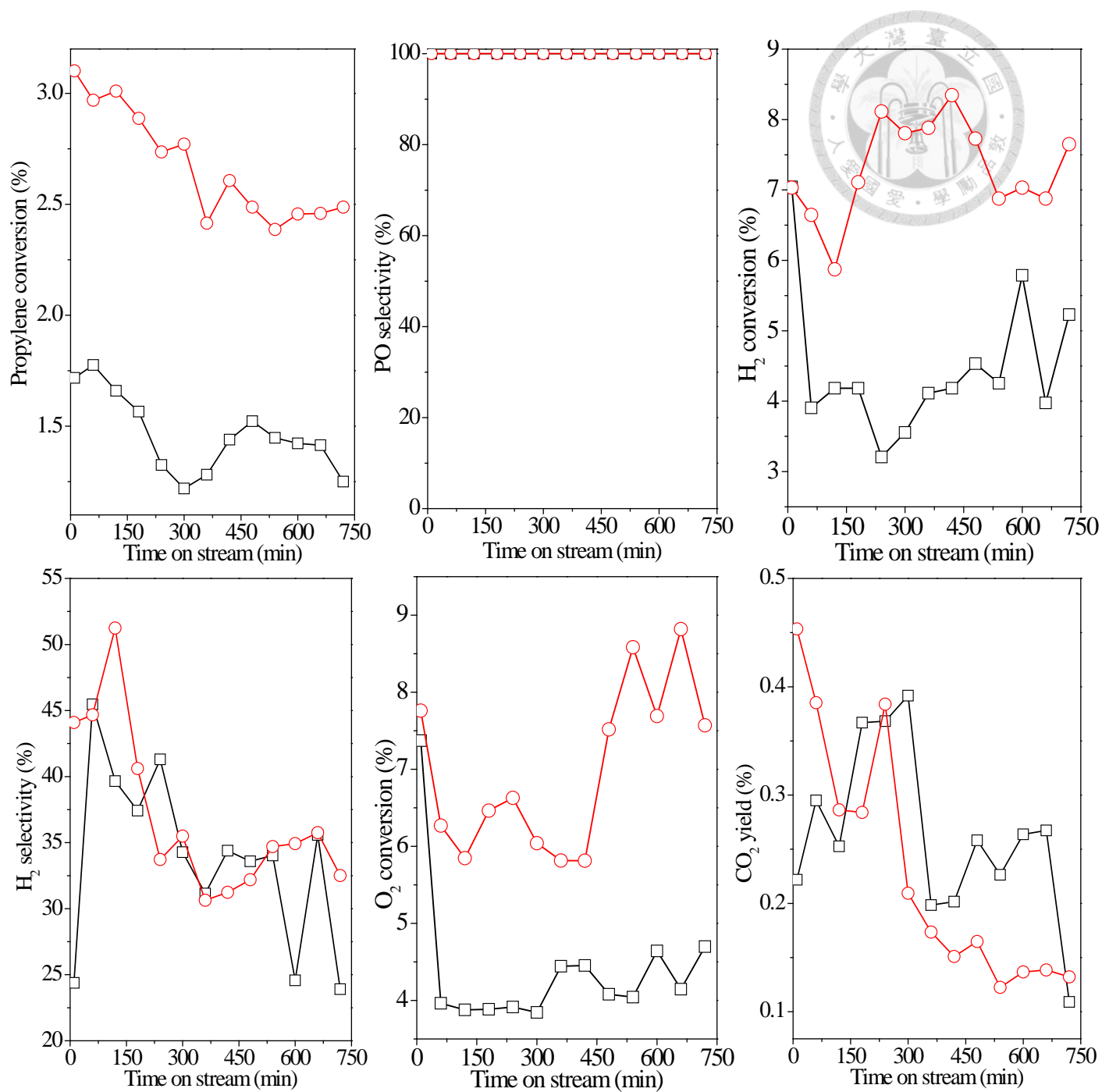
Fig. 4-28 Catalytic performance over (□) 10Au^{3+}/1Ti (○) 10Au^{3+}/1TiZ catalysts.
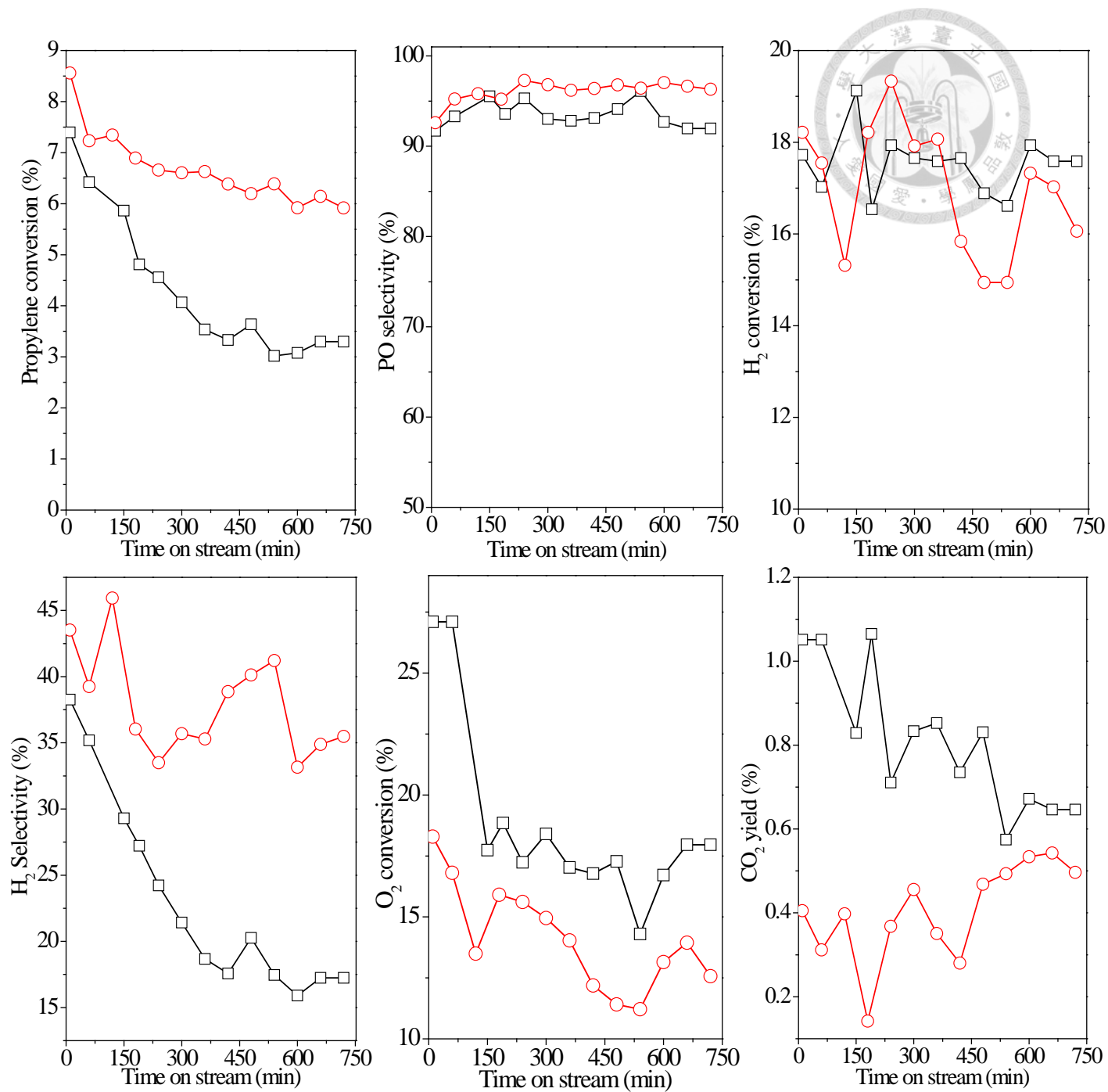
Fig. 4-29 Catalytic performance over (□) 10Au³⁺/3Ti (○) 10Au³⁺/3TiZ catalysts.
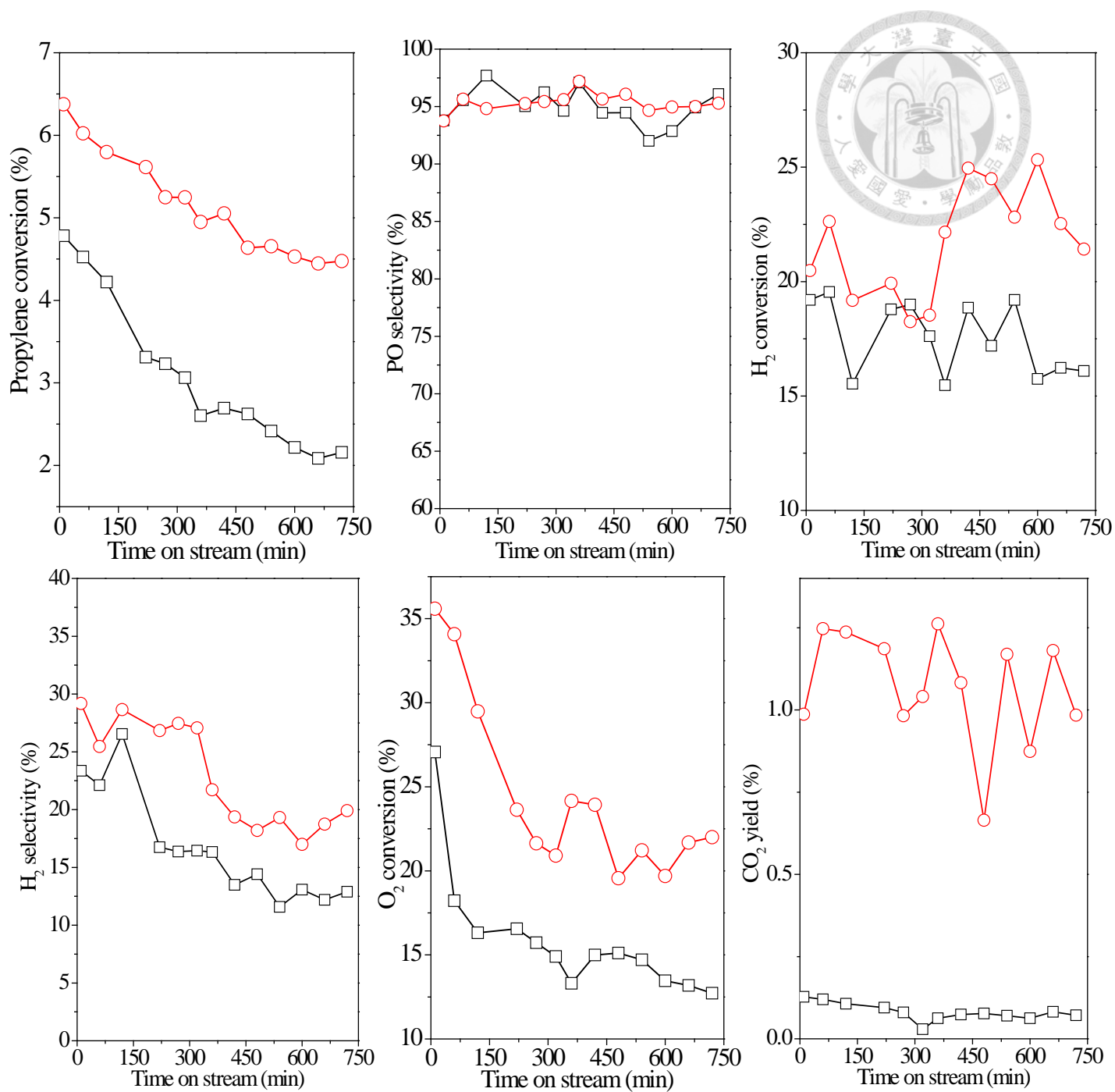
Fig. 4-30 Catalytic performance over (□) 10Au^{3+}/5Ti (○) 10Au^{3+}/5TiZ catalysts.

Table 4-5 Comparison of catalytic performance between $10Au^{3+}/Ti$ and $10Au^{3+}/Ti$ catalysts with different Ti content

Catalyst	Rxn time (min)	Propene conv.(%)	PO yield (%)	H_2 conv. (%)	H_2 select. (%)	Selectivity (%)					Decay rate (%)[a]
						PO	PA	ACR	ACE	CO_2	
	10										
$10Au^{3+}/1Ti$		1.7	1.7	7.0	24.4	99.9	0	0	0	0.1	27.0
$10Au^{3+}/1TiZ$		3.1	3.1	7.0	44.1	99.5	0	0	0	0.5	19.7
$10Au^{3+}/3Ti$		7.4	6.8	17.7	38.9	91.7	4.0	2.4	1.8	0.1	55.4
$10Au^{3+}/3TiZ$		8.6	7.9	18.2	43.5	92.6	1.6	2.9	2.9	0.4	31.1
$10Au^{3+}/5Ti$		4.8	4.6	19.2	23.4	93.8	2.0	3.3	0.9	0.1	54.8
$10Au^{3+}/5TiZ$		6.4	6.0	20.5	29.2	93.8	2.6	2.6	1.0	0.2	29.8
	600										
$10Au^{3+}/1Ti$		1.4	1.4	5.8	24.6	99.8	0	0	0	0.2	7
$10Au^{3+}/1TiZ$		2.5	2.5	7.0	34.9	99.9	0	0	0	0.1	0
$10Au^{3+}/3Ti$		3.1	2.9	17.9	15.9	92.7	3.0	0.5	1.3	0.4	0
$10Au^{3+}/3TiZ$		5.9	5.7	17.3	33.1	97.0	1.2	1.2	0	0.3	0
$10Au^{3+}/5Ti$		2.7	2.4	12.7	18.0	91.7	5.0	1.4	0	0.5	3
$10Au^{3+}/5TiZ$		4.5	4.3	19.7	21.8	95.0	2.7	0.7	1.0	0.2	1

[a](propene conv. at 10 min or 600 min- propene conv. at 720 min)/ propene conv. at 10 min or 600 min. [b]reaction condition: 0.3 g catalysts, 160 ^{o}C, 10 min, space velocity: 5000 mL min^{-1} g_{cat}^{-1}

Table 4-6 Comparison of catalytic performance of several catalysts.

Catalyst	Propylene conv. (%)	PO selectivity (%)	Reaction temperature (^{o}C)	Space velocity (mL g_{cat}^{-1} h^{-1})	PO formation rates (g_{PO} kg_{cat}^{-1} h^{-1})	Ref.
0.25wt% Au/TS-1(48)-Na1	8.8	82	200	8000	137	114
silylated Au/Ti−SiO$_2$	5.75	98.4	150	4000	52	120
meso-Ti-Si	7	90	150-160	4000	60	104
0.05Au/TS-1(36)	8.8	81	200	7000	118	108
0.33Au/PCTS-1(28)	9.7	87	200	7000	132	157
0.5Au/TS-1(35)-IL	10.1	72.1	300	7000	120	158
Au/TS-1-B	-	-	200	14000	125	121
0.146Au/TS-1(99)	-	-	200	14000	160	159
0.16Au/TS-1(121)Cs	11.4	88.8	200	14000	320	117
10Au^{3+}/3TiZ	8.6	92.6	160	5000	95	Our study

4.3 Conclusions

Ti-incorporated mesoporous silica materials of cubic $Pm3n$ structure were successfully synthesized at pH around 9 using CTEABr as the template and sodium silicate as the silica sources and then gold was deposited on these supports by DP method. The X-ray diffraction studies showed that the resultant materials owned well-ordered cubic $Pm3n$ mesostructure before and after gold deposition. Elemental analysis by ICP-MS showed that the amounts of Ti(IV) ions incorporated in the mesoporous silica materials were close to those in the synthesis solutions and the gold loadings increased with Ti content increasing. The UV-Vis spectra showed that when Ti/Si increased up to 5% extra-framework TiO_2 clusters were formed

The optimal reaction condition was conducted as followed: reaction temperature is 160 ^{o}C and catalyst amount is 0.3 g. The $10Au^{3+}/3Ti$ catalyst with having 0.48wt% actual gold loading and Ti/Si molar ratio of 3.0% gave the higher propylene conversion of 7.4% and PO yield of 6.8%. The best performance is attributed to suitable size of gold clusters (3 nm) and less extra-framework TiO_2 clusters.

Furthermore, gold deposited on Ti-ZSBA-1 materials with zeolitic wall were successfully prepared by using TS-1 seeds as silica source and CTEABr as surfactants. The physical and chemical properties of Ti-ZSBA-1 materials characterized by XRD, N_2 adsorption-desorption isotherms, ICP-MS and UV-Vis spectra were similar to those of Ti-SBA-1-alk materials. The highest conversion of 8.6% and PO yield of 7.9% were obtained over $10Au^{3+}/3Ti$-ZSBA-1 catalyst with actual gold loading of 0.48wt%. Moreover, the catalyst deactivation was improved significantly due to its crystallite wall.

Chapter 5　References

1　P. S. Goyal, V. K. Aswal, *Current Sci.* **2001**, *80*, 972.

2　Q. S. Huo, D. I. Margolese, G. D. Stucky, *Chem. Mater.* **1996**, *8*, 1147.

3　J. N. Israelachvili, D. J. Mitchell, B. W. Niham, *J. Chem. Soc.*, *Faraday Trans. 2*, **1976**, *72*, 1525.

4　J. N. Israelachvili, D. J. Mitchell, B. W. Niham, *Biochim. Biophys. Acta* **1977**, *470*, 185.

5　S. Segota, D. Tezak, *Adv. Colloid. Interfac.* **2006**, *121*, 51.

6　C. T. Kresge, M. E. Leonowicz, W. J. Roth, J. C. Vartuli J. S. Beck, *Nature* **1992**, *359*, 710.

7　J. S. Beck, J. C. Vartuli, W. J. Roth, M. E. Leonowicz, C. T. Kresge, K. D. Schmitt, C. T. -W. Chu, D. H. Olson, E. W. Sheppard, S. B. Higgins J. L. Schlenker*, J. Am. Chem. Soc*, **1992**, *114*, 10834.

8　A. Sayari, *Chem. Mater.* **1996**, *8*, 1840.

9　R. C. Hayward, P. A. Henning, B. F. Chemlka, G. D. Stucky, *Micropor. Mesopor. Mater*. **2001,** *44*, 619.

10　B. J. Scott, G. Wirnsberger, G. D. Syucky, *Chem. Mater.* **2001**, *13*, 3140.

11　J. Y. Ying, C. P. Mehnert, M. S. Wong, *Angew. Chem. Int. Ed.* **1999**, *38*, 56.

12　P. Behrens, *Adv. Mater.* **1993**, *5*, 127.

13　J. C. Vartuli, C. T. Kresge, M. E. Leonowicz, A. S. Chu, S. B. McCullen, I. D. Johnson, E. W. Sheppard, *Chem. Mater.* **1994**, *6*, 2070.

14　C. Y. Chen, S. L. Burkett, H. X. Li, M. E. Davis, *Microporous Mater.* **1993**, *2*, 27.

15　A. Monnier, F. Schüth, Q. Huo, D. Kumar, D. Margolese, R. S. Maxwell, G. D.

Stucky, M. Krishnamurty, P. Petroff, A. Firouzi, M. Janicke, B. F. Chmelka, *Science* **1993**, *261*, 1299.

16 A. Steel, S. W. Carr, M. W. Anderson, *J. Chem. Soc. Chem. Commun.* **1994**, 1571.

17 A. Firouzi, D. Kumar, L. M. Bull, T. Besier, P. Sieger, Q. Huo, S. A. Walker, J. A. Zasadzinski, C. Glinka, J. Nicol, D. Margolese, G. D. Stucky, B. F. Chmelka, *Science* **1995**, *267*, 1138

18 Q. Huo, D. I. Margolese, U. Ciesla, P. Feng, T. E. Gier, P. Sieger, R. Leon, P. M. Petroff, F. Schüth, G. D. Stucky, *Nature* **1994**, *368*, 317.

19 Q. Huo, D. I. Margolese, U. Ciesla, D. G. Demuth, P. Feng, T. E. Gier, P. Sieger, A. Firouzi, B. F. Chmelka, F. Schuth, G. D. Stucky, *Chem. Mater.* **1994**, *6*, 1176.

20 G. J. D. Soler-illia, C. Sanchez, B. Lebeau, J. Patarin, *Chem. Rev.* **2002**, *102*, 4093.

21 A. K. Cheetham, G. Ferey, T. Loisean, *Angew. Chem. Int. Ed.* **1999**, *38*, 3268.

22 H. de St. Claire Deville, *Compt. Rend. Seances Acad. Sci.* **1862**, *54*, 324.

23 R. M. Barrer, *J. Chem. Soc.* **1948**, 127.

24 R.M. Milton, US Patent 2 882 244, 1959.

25 R. M. Barrer, P. J. Denny, *J. Chem. Soc*. **1961**, 971.

26 G. T. Kerr, G. T .Kokotailo, *J. Am. Chem. Soc*. **1961**, *83*, 4675.

27 G. T. Kerr, *Inorg. Chem*. **1966**, *5*, 1537.
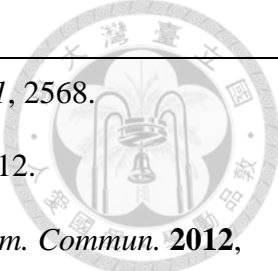
28 R. J. Argouer, G. R. Landolt, US Patent 3 702 866, 1972.

29 G. T. Kokotailo, S. L. Lawton, D. H. Olson, W. M. Meier, *Nature* **1978**, *272*, 437.

30 D. H. Olson, G. T. Kokotailo, S. L. Lawton, W. M. Meier, *J. Phys. Chem.* **1981**, *85*, 2238.

31 A. Croma, *J. Catal*. **2003**, *216*, 298.
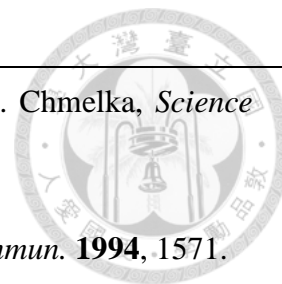
32 M. Kruk, M. Jaroniec, R. Ryoo, J. M. Kim, *Chem. Mater.* **1999**, *11*, 2568.

33 Y. Hao, Y. Chong, S. Li, H. Yang, *J. Phys. Chem. C* **2012**, *116*, 6512.

34 P. J. Lebed, K. de Souza, F. Bilodeau, D. Lariviere, F. Kleitz, *Chem. Commun.* **2012**, *47*, 11525.

35 C. Pirez, J. -M. Caderon, J. -P. Dacquin, A. F. Lee, K. Wilson, *ACS Catal.* **2012**, *2*, 1607.

36 Y. Sakamoto, M. Kaneda, O. Terasaki, D. Y. Zhao, J. M. Kim, G. Stucky, H. J. Shin, R. Ryoo, *Nature* **2000**, *408*, 449.

37 M. J. Kim, R. Ryoo, *Chem. Mater.* **1999**, *11*, 487.

38 S. Che, Y. Sakamoto, O. Terasaki, T. Tatsumi, *Chem Mater.* **2001**, *13*, 2237.

39 S. Che, S. Lim, M. Kaneda, H. Yoshitake, O. Terasaki, T. Tatsumi, *J. Am. Chem. Soc.* **2002**, *124*, 13962.

40 S. Che, H. Li, S. Lim, Y. Sakamoto, O. Terasaki, T. Tatsumi, *Chem. Mater.* **2005**, *17*, 4103.

41 S. Che, Y. Sakamoto, O. Terasaki, T. Tatsumi, *Micropo. Mesopo. Mater,* **2005**, *85*, 207.

42 M. C. Liu, H. S. Sheu, S. Cheng, *Chem. Commun.* **2002**, 2854.

43 M. Ogura, H. Miyishi, S. P. Naik, T. Okubo, *J. Am. Chem. Soc.* **2004**, *126*, 10937

44 M. C. Liu, H. S. Sheu, S. Cheng, *J. Am. Chem. Soc.* **2009**, *131*, 3998.

45 M. C. Chao, D. S. Wang, H. P. Lin, C. M. Mou, *J. Mater. Chem.* **2003**, *13*, 2853.

46 M. C. Chao, D. S. Wang, H. P. Lin, C. M. Mou, *Chem. Lett.* **2004**, *33*, 374.

47 A. Vinu, V. Murugesan, M. Hartmann, *Chem. Mater.* **2003**, *15*, 1385.

48 H. -M. Kao, C. -C. Ting, A. S. T. Chiang, C. -C. Teng, C. -H. Chen, *Chem Commun.*
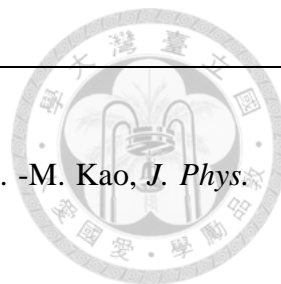
2005, 1058.

49 C. -C. Ting, H. -Y. Wu, Y. -C. Pan, S. Vetrivel, G. T. K. Fey, H. -M. Kao, *J. Phys. Chem. C* **2010**, *114*, 19322.

50 D. Ji, R. Zhao, G, Lv, G. Qian, L. Yan, J. Suo, *Appl. Catal. A: General* **2005**, *281*, 39.

51 A. Vinu, T. Krithiga, V. Balasubramanian, A. Asthana, P. Srinivasu, T. Mori, K. Ariga, G. Ramanath, P. G. Ganesan, *J. Phys. Chem. B* **2006**, *110*, 11924.

52 V. V. Balasubramanian, C. Anand, R. R. Pal, T. Mori, W. Böhlmann, K. Ariga, A. K. Tyagi, A. Vinu, *Micropor. Mesopor. Mater.* **2009**, *121*, 18.

53 R. Brzozowski, A. Vinu, B. Gil, *Appl. Catal. A: General* **2010**, *377*, 76.

54 M. -C. Liu, C. -S. Chang, J. C. C. Chan, H. -S. Sheu, S. Cheng, *Micropor. Mesopor. Mater.* **2009**, *121*, 41.

55 Y. Tao, H. Kanoh, L. Abrams, K. Kaneko, *Chem. Rev.* **2006**, *106*, 896.

56 J. Cejka, S. Mintova, *Catal. Rev. - Sci. Eng.* **2007**, *49*, 457.

57 K. Egeblad, C. H. Christensen, M. Kustova, C. H. Christensen, *Chem. Mater.* **2008**, *20*, 946.

58 J. Perez-Ramirez, C. H. Christensen, K. Egeblad, C. H. Christensen, J. C. Groen, *Chem. Soc. Rev.* **2008**, *37*, 2530.

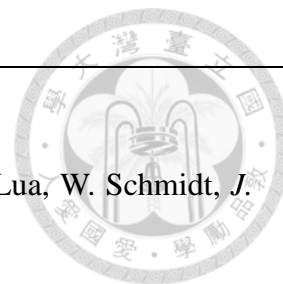59 K. Na, M. Choi, R. Ryoo, *Micropor. Mesopor. Mater.* **2013**, *166*, 3.

60 K. R. Kloetstra, H. van Bekkum, J. C. Jansen, *Chem. Commun.* **1997**, 2281.

61 L. Huang, W. Guo, P. Deng, Z. Xue, Q. Li, *J. Phys. Chem. B* **2000**, *104*, 2817.

62 A. Karlsson, M. Stocker, R. Schmidt, *Micropor. Mesopor. Mater.* **1999**, *27*, 181.

63 A. Sakthivel, S. -J. Huang, W. -H. Chen, Z. -H. Lan, K. -H. Chen, H. -P. Lin, C. -Y.

Mou, S. -B. Liu, *Adv. Funct. Mater.* **2005**, *15*, 253.

64 X. Gu, T. Jiang, H. Tao, S. Zhou, X. Liu, J. Ren, Y. Wang, G. Lua, W. Schmidt, *J. Mater. Chem.* **2011**, *21*, 880.

65 Z. Zhang, Y. Han, F. -S. Xiao, S. Qiu, L. Zhu, R. Wang, Y. Yu, Z. Zhang, B. Zou, Y. Wang, H. Sun, D. Zhao, Y. Wei, *J. Am. Chem. Soc.* **2001**, *123*, 5014.

66 Y. Han, S. Wu, Y. Sun, D. Li, F .-S. Xiao, J. Liu, X. Zhang, *Chem. Mater.* **2002**, *14*, 1144.

67 Y. Liu, T. J. Pinnavaia, *J. Mater. Chem.* **2002**, *12*, 3179.

68 Y. Liu, T.J. Pinnavaia, *Chem. Mater.* **2002**, *14*, 3.

69 D. P. Serrano, R. A. Garcia, G. Vicente, M. Linares, D. Prochazkova, J. Cejka, *J. Catal.* **2011**, *279*, 366.

70 R. Le van Mao, S. T. Le, D. Ohayon, F. Caillibot, L. Gelebart, G. Denes, *Zeolites* **1997**, *19*, 270.

71 A. Cizmek, B. Suboti, I. Smit, A. Tonejc, R. Aiello, F. Crea, A. Nastro, *Microporous. Mater.* **1997**, *8*, 159.

72 M. Ogura, S. Y. Shinomiya, J. Tateno, Y. Nara, E. Kikuchi, H. Matsukata, *Chem. Lett.* **2000**, 882.

73 J. C. Groen, J. C. Jansen, J. A. Moulijn, J. Pérez-Ramírez, *J. Phys. Chem. B* **2004**, *108*, 13062.

74 J. C. Groen, S. Abello, L. A. Villaescusa, J. Pérez-Ramírez, *Micropor. Mesopor. Mater.* **2008**, *114*, 93.

75 F. C. Meunier, D. Verboekend, J. -P. Gilson, J. C. Groen, J. Pérez-Ramírez, *Micropor. Mesopor. Mater.* **2012**, *148*, 115

76 J. Scherzer, *J. Catal.* **1978**, *54*, 285.

77 J. Lynch, F. Raatz, P. Dufresne, *Zeolites* **1987**, *7*, 333.

78 J. Lynch, F. Raatz, Ch. Delalande, *Stud. Surf. Sci. Catal.* **1988**, *39*, 547.

79 C. J. H. Jacobsen, C. Madsen, J. Houzvicka, I. Schmidt, A. Carlsson, *J. Am. Chem. Soc.* **2000**, *122*, 7116.

80 I. Schmidt, A. Boisen, E. Gustavsson, K. Stahl, S. Pehrson, S. Dahl, A. Carlsson, C. J. H. Jacobsen, *Chem. Mater.* **2001**, *13*, 4416.

81 A. H. Janssen, I. Schmidt, C. J. H. Jacobsen, A. J. Koster, K. P. de Jong, *Micropor. Mesopor. Mater.* **2003**, *65*, 59.

82 A. Sakthivel, S. Huang, W. Chen, Z. Lan, K. Chen, T. Kim, R. Ryoo, A. S. T. Chiang, S. Liu, *Chem. Mater.* **2004**, *16*, 3168.

83 Z. Yang, Y. Xia, R. Mokaya, *Adv. Mater.* **2004**, *16*, 727.

84 M. Choi, K. Na, J. Kim, Y. Sakamoto, O. Terasaki, R. Ryoo, *Nature* **2009**, *461*, 246.

85 K. Na, C. Jo, J. Kim, K. Cho, J. Jung, Y. Seo, R. J. Messinger, B. F. Chmelka, R. Ryoo, *Science* **2011**, *333*, 328.

86 T. R. Pauly, Y. Liu, T. J. Pinnavaia, S. J. L. Billinge, T. P. Rieker, *J. Am. Chem. Soc.* **1999**, *121*, 8835.

87 P. -G. Pietta, *J. Nat. Prod.* **2000**, *63*, 1035.

88 T. P. T. Cushnie, A. J. Lamb, *Int. J. Antimicob. Ag.* **2005**, *26*, 343

89 E. Middleton; C. Kandaswami, T. C. Theoharides, *Pharmacol. Rev.* **2000**, *52*, 673

90 T. A. Nijhuis, M. Makkee, J. A. Moulijn, B. M. Weckhuysen, *Ind. Eng. Chem. Res.* **2006**, *45*, 3447.

91 Halcon International Inc., U. S. Patent 3 350 422 1966.

92 T. Seo, J. Tsuji, U.S. Patent 6 646 139 2003.

93 M.G. Clerici, G. Bellussi, U. Romano, *J. Catal.* **1991**, *129*, 159.

94 C. Perego, A. Carati, P. Ingallina, M. A. Mantegazza, Giuseppe Bellussi, *Appl. Catal. A: General*, **2001**, *221*, 63.

95 M. Taramasso, G. Perego, B. Notari, U.S. Patent 4 410 501 1983.

96 A. H. Tullo, P. L. Short, Chem. Eng. News 2006, 88, 22.

97 M. Haruta, B. S. Uphade, S. Tsubota, A. Miyamoto, *Res. Chem. Intermed.* **1998**, *24*, 329.

98 T. Hayashi, K. Tanaka, M. Haruta, *J. Catal.* **1998**, *178*, 566.

99 B. S. Uphade, Y. Yamada, T. Akita, T. Nakamura, M. Haruta, *Appl. Catal. A: General* **2001**, *215*, 137.

100 B. S. Uphade, T. Akita, T. Nakamura, M. Haruta, *J. Catal.* **2002**, *209*, 331.

101 E. Sacaliuc, A. M. Beale, B. M. Weckhuysen, T. A. Nijhuis, *J. Catal.* **2007**, *248*, 235.

102 H. Yang, D. Tang, X. Lu, Y. Yuan, *J. Phys. Chem. C* **2009**, *113*, 8186.

103 C. Qi, T. Akita, M. Okumura, M. Haruta, *Appl. Catal. A: General* **2001**, *218*, 81.

104 A. K. Sinha, S. Seelan, M. Okumura, T. Akita, S. Tsubota, M. Haruta, *J. Phys. Chem. B* **2005**, *109*, 3956.

105 L. Xu, Y. Ren, H. Wu, Y. Liu, Z. Wang, Y. Zhang, J. Xu, H. Peng, P. Wu, *J. Mater. Chem.*, **2011**, *21*, 10852.

106 C. -H. Liu, Y. Guan., E. J. M. Hensen, J. -F. Lee, C. -M. Yang, *J. Catal.* **2011**, *282*, 94.

107 J. Huang, E. Lima, T. Akita, A. Guzman, C. Qi, T. Takei, M. Haruta, *J. Catal.* **2011**,

278, 8.

108 B. Taylor, J. Lauterbach, W. N. Delgass, *Appl. Catal. A: General* **2005**, *291*, 188.

109 W. -S. Lee, L. -C. Lai, M. C. Akatay, E. A. Stach, F. H. Ribeiro, W. N. Delgass, *J. Catal.* **2012**, *296*, 31.

110 J.J. Bravo-Suarez, K. K. Bando, J. I. Lu, M. Haruta, T. Fujitani, S.T. Oyama, *J. Phys. Chem. C* **2008**, *112*, 1115.

111 B. Chowdhury, J. J. Bravo-Suarez, N. Mimura, J. Q. Lu, K. K. Bando, S. Tsubota, M. Haruta, *J. Phys. Chem. B* **2006**, *110*, 22995.

112 L. Cumaranatunge, W. N. Delgass, *J. Catal.* **2005**, *232*, 38.

113 J. -Q. Lu, N. Li, X. -R. Pan, C. Zhang, M. -F. Luo, *Catal. Commun.* **2012**, *28*, 179.

114 J. Huang, T. Takei, T. Akita, H. Ohashi, M. Haruta, *Appl Catal B: Environ.* **2010**, *95*, 430.

115 J. Lu, X. Zhang, J. J. Bravo-Suárez, T. Fujitani, S. T. Oyama, *Catal. Today* **2009**, *147*, 186.

116 A. K. Sinha, S. Seelan, S. Tsubota, M. Haruta, *Angew. Chem. Int. Ed.* **2004**, *43* 1546.

117 W. -S Lee, M. C. Akatay, E. A. Stach, F. H. Ribeiro, W. N. Delgass, *J. Catal.* **2013**, *308*, 98.

118 J. Huang, T. Takei, H. Ohashi, M. Haruta, *Appl. Catal. A: General* **2012**, *435-436*, 115.

119 B. Chowdhury, J. J. Bravo-Suarez, M. Date, S. Tsubota, M. Haruta, *Angew. Chem. Int. Ed.* **2006**, *45*, 412.

120 B. Chowdhury, K. K. Bando1, J .J. Bravo-Suarez, S. Tsubota, M. Haruta, *J. Mol.*

Catal. A: Chem. **2012**, *359*, 21.

121 X. Feng, X. Duan, G. Qian, X. Zhou, D. Chen, W Yuan, *Appl. Catal. B: Environ.* **2014**, *150-151*, 396.

122 W. -S Lee, M. C. Akatay, E. A. Stach, F. H. Ribeiro, W. N. Delgass, *J. Catal.* **2014**, *313*, 104.

123 S. J. Jong, S. Cheng, *Appl. Catal. A: General*, **1995**, *126*, 51.

124 D. P. Serrano, R. Sanz, P. Pizarro, I. Moreno, *Appl. Catal. A: General,* **2012**, *435 – 436*, 32.

125 S. Brunauer, P. H. Emmett, E. Teller, *J. Am. Chem. Soc.* **1938**, *60*, 309.

126 E. P. Barrett, L. G. Joyner, P. P. Halenda, *J. Am. Chem. Soc*. **1951**, *73*, 373.

127 P. Kubelka, F. Munk, *Z. Tech. Phys*. **1931**, *12*, 593.

128 M. A. Camblor, J. Perez-Pariente, *Zeolite* **1991**, *11*, 202.

129 E. M. Flanigen, H. Khatami, H. Szymanski, *Adv. Chem. Ser.*, **1971**, *101*, 201.

130 E. M. Flanigen, in J.A. Rabo (Editor), Zeolite Chemistry and Catalysis, Am. Chem. Soc., Washington, 1976, p. 80.

131 J. C. Jansen , F. J. van der Gaag, H. van Bekkum, *Zeolites* **1984**, *4*, 369.
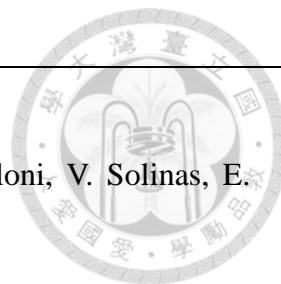
132 G. Coudurier, C. Naccache and J.C. Vedrine, *J. Chem. Soc., Chem. Commun.* **1982** 1413.

133 E. Oldfield, J. Haase, K. D. Schmitt, S. E. Schrammb, *Zeolites* **1994**, *14*, 101.

134 X. Wang, S. Cheng, J. C. C. Chan, *J. Phys. Chem. C* **2007**, *111*, 2156.

135 D. Margolese, J. A. Melero, S. C. Christiansen, B. F. Chmelka, G. D. Stucky, *Chem. Mater.* **2000**, *12*, 2448.

136 J. Datka, S. Marschmeyer, T. Neubauer, J. Meusinger, H. Papp, F. -W. Schu1tze, I.

Szpyt, *J. Phys. Chem.* **1996**, *100*, 14451.

137 A. Ungureanu, B. Dragoi, V. Hulea, T. Cacciaguerra, D. Meloni, V. Solinas, E. Dumitriu, *Micropor. Mesopor. Mater.* **2012**, *163*, 51.

138 Q. Yang, J. Yang, Z. Feng, Y. Li, *J. Mater. Chem.* **2005**, *15*, 4268.

139 J. Lu, X. Zhang, J. J. Bravo-Suarez, T. Fujitani, S. T. Oyama, *Catal. Today* **2009**, *147*, 186.

140 J. W. Lee, S. Kong, W. S. Kim, J. Kim, *Mater. Chem. Phys.* **2007**, *106*, 39.

141 A. Zecchina, G. Spoto, S. Bordiga, A. Ferrero, G. Petrini, G. Leofanti, M. Padovan, *Stud. Surf. Sci. Catal.* **1991**, *69*, 251.

142 S. -Y. Chen, C. -Y. Tang, J. -F. Lee, L. -Y. Jang, T. Tatsumi, S. Cheng, *J. Mater. Chem.* **2011**, *21*, 2255.

143 F. -T. Kuo, S. -Y. Chen, T. -H. Lin, J. -F. Lee, S. Cheng, *RSC Adv.* **2013***, 3*, 12604.

144 T. Imanaka, Y. Okamoto, S. Teranish, *Bull. Chem. Soc. Jpn.* **1972**, *45*, 3251.

145 F. Dubnikova, A. Lifshitz, *J. Mater. Chem. A* **2000**, *104*, 4489.

146 M. Daniel, D. Astruc, *Chem. Rev.* **2004**, *104*, 293.

147 J. E. Penner-Hahn, *Coordin. Chem. Rev.* **1999**, *190-192*, 1101.

148 J. G. Parsons, M. V. Aldrich, J. L. Gardea-Torresdey, *Appl. Spectrosc. Rev.* **2002**, *37*, 187.

149 A. L. Ankudinov, B. Ravel, J. J. Rehr, S. D. Conradson, *Phys. Rev. B* **1998**, *58*, 7565.

150 R. B. Greegor, F. W. Lytle, *J. Catal.* **1980**, *63*, 476.

151 R. E. Benfeld, *J. Chem. Soc., Faraday Trans.* **1992**, *88*, 1107.

152 A. Jentys, *Phys. Chem. Chem. Phys.* **1999**, *1*, 4059.

153 A. I. Frenkel, S. Nemzer, I. Pister, L. Soussan, T. Harris, Y. Sun, and M. H. Rafailovich, *J. Chem. Phys.* **2005**, *123*,184701.

154 A. I. Frenkel, C. W. Hills, R. G. Nuzzo *J. Phys. Chem. B* **2001**, *105*, 12689,

155 D. R. C. Huybrechts, P. L. Buskens, P. A. Jacobs, *J. Mol. Catal.* **1992**, *71*, 129.

156 G. Mul, A. Zwijnenburg, B. van der Linden, M. Makkee, J.A. Moulijn, *J. Catal.* **2001**, *201*, 128.

157 B. Taylor, J. Lauterbach, W. N. Delgass, *Catal. Today* **2007**, *123*, 50.

158 M. Du, G. Zhan, X. Yang, H. Wang, W. Lin, Y. Zhou, J. Zhu, L. Lin, J. Huang, D. Sun, L. Jia, Q. Li, *J. Catal.* **2011**, *283*, 192.

159 W. -S. Lee, M. C. Akatay, E. A. Stach, F. H. Ribeiro, W. N. Delgass, *J. Catal.* **2012**, *287*, 178.